R diss 2742. S

Stellingen behorend bij het proefschrift

DEFECTS IN NUCLEAR FUSION REACTOR MATERIALS

STUDIED BY

THERMAL GAS DESORPTION SPECTROMETRY

1.

De door Schwirtlich en Schultz gerapporteerde migratieënergie van monovacatures in molybdeen van 1,35 eV, de door Maier *et al.* gerapporteerde migratieënergie van monovacatures in molybdeen van 1,5 eV, en de door Hansen *et al.* en Linderoth *et al.* gerapporteerde maximale dissociatieënergie van waterstof uit monovacatures in molybdeen van 1,7 eV, alle gemeten met behulp van technieken die geen goed onderscheid kunnen maken tussen monovacatures en kleine vacatureclusters, zijn tienden van een elektronvolt te hoog.

I.A. Schwirtlich en H. Schultz, Phil. Mag. A. **42** (1980) 601.
K. Maier, M. Peo, B. Saile, H.E. Schaefer and A. Seeger, Phil. Mag. A. **40** (1980) 701.
H.E. Hansen, R. Talja, H. Rajainmäki, H.K. Nielsen, B. Nielsen and R.M. Nieminen, Appl. Phys. A **36** (1985) 81.
S. Linderoth, H. Rajainmäki, B. Nielsen, H.E. Hansen, R.M. Nieminen en K. Petersen, Mater. Sci. Forum **15-18** (1987) 751.
Dit proefschrift, hoofdstuk 4.2 en 4.3.

2.

De door Kornelsen gerapporteerde verzadiging in argonretentie die is waargenomen tijdens het bestralen van wolfraam met argon in doses tot 5×10^{16} cm^{-2} wordt ten onrechte voor verzadiging aangezien omdat Kornelsen niet heeft onderzocht welke effecten optreden bij doses hoger dan 5×10^{16} cm^{-2}.

E.V. Kornelsen, Canad. J. Phys. **42** (1964) 364.
Dit proefschrift, hoofdstuk 3.3.

3.

In het onderzoek naar defecten in kernfusiereactormaterialen neemt de bruikbaarheid van thermische gasdesorptiespectrometrie af naarmate de complexiteit van de defecten toeneemt en er meer structurele defecten en verontreinigingen in de materialen aanwezig zijn, terwijl de bruikbaarheid toeneemt naarmate er meer complementaire informatie verkregen kan worden met behulp van andere technieken.

Dit proefschrift, hoofdstuk 3.3, 4.4, 5.3 en 6.3.

4.

De faseovergangen die optreden ten gevolge van devitrificatie en smelten tijdens het verhitten van de in de hoge-energiefysica als gepolariseerde targets gebruikte 1-butanol-glazen kunnen worden onderdrukt door toevoeging van minimaal 1,5 massaprocent water aan het 1-butanol. Voor 1-pentanol-glazen is het daarentegen niet mogelijk genoemde faseovergangen te onderdrukken door het toevoegen van water.

T.O. Niinikoski, in: Proc. of the Second Workshop on Polarised Target Materials (Rutherford and Appleton Laboratories, Report RL-80-080, 1980) p. 56.

5.

Een van de oudste voorbeelden van een goed opgezet wetenschappelijk experiment is het in de bijbel beschreven experiment dat door de profeet Elia werd uitgevoerd om aan te tonen dat de god Baäl niet bestaat en de god van Abraham, Isaäk en Israël wel.

De bijbel, 1 Koningen 18:20-46.

6.

Een ieder die meewerkt aan de proliferatie van een religie of ideologie en daarbij geen aandacht schenkt aan andere religies of ideologieën, maakt zich schuldig aan hetzelfde vergrijp als een onderzoeker die slechts die onderzoeksresultaten publiceert die overeenstemmen met zijn hypothese en de resultaten die daarmee strijdig zijn niet.

7.

Een groot deel van de officieel in Nederland geregistreerde geneesmiddelen levert slechts een bijdrage aan de bestrijding van symptomen en bewerkstelligt, in tegenstelling tot hetgeen de naam suggereert, geen genezing. Het hanteren van de pretentieuze naam geneesmiddel is daarom wetenschappelijk onverantwoord.

8.

In de gezondheidsindustrie kunnen aanzienlijke kosten worden bespaard door een medisch specialisme in het leven te roepen voor syndromen die bij de vigerende stand van de medische wetenschap niet éénduidig kunnen worden verklaard.

9.

Teneinde de verkeersveiligheid, de verkeersdoorstroming, het milieu, de bloeddruk van verkeersdeelnemers, en de levensduur van vervoermiddelen te dienen, behoort het uitgangspunt van het verkeersbeleid te zijn dat alle vervoermiddelen zich zoveel mogelijk met een voorspelbare eenparige snelheid voortbewegen. De noodzakelijkheid van voorzieningen en verkeersregels die snelheidsveranderingen met zich meebrengen, zoals kruispunten, verkeerslichten, bushaltes, verkeersdrempels, de verkeersregel dat niet het doorgaand verkeer maar verkeer komend van rechts voorrang heeft, en het ontbreken van een inhaalverbod voor vrachtverkeer op autosnelwegen, dienen in dit licht te worden herbezien.

10.

Voor bewoners van landen die geplaagd worden door armoede, uitzichtloosheid en een corrupte overheid is een harder justitieel klimaat noodzakelijk dan voor bewoners van landen met relatief weinig armoede, uitzichtloosheid en corruptie, omdat voor de eerste groep mensen de merites van crimineel gedrag relatief groter zijn, de repercussies relatief minder ernstig, en het schuldgevoel relatief kleiner.

11.

Zolang in een democratie een deel van de stemgerechtigden stemt op een partij die voor de belangen van de achterban opkomt, en een deel van de stemgerechtigden op een partij die de verschillende belangen in een samenleving tegen elkaar afweegt, worden de belangen van de tweede groep tekort gedaan.

12.

Bij bezuinigingen met de zogenaamde kaasschaafmethode wordt ook de kip met de gouden eieren een kopje kleiner gemaakt.

559742

TR diss 2142

TR diss
2142

DEFECTS IN NUCLEAR FUSION REACTOR MATERIALS

STUDIED BY

THERMAL GAS DESORPTION SPECTROMETRY

H. A. FILIUS

BIBLIOTHEEK TECHNISCHE UNIVERSITEIT
Prometheusplein 1
2628 ZC
DELFT

Interfacultair Reactor Instituut

Technische Universiteit Delft / Delft University of Technology

Cover: Particles migrating from one saturated trap to another, analogous to the trapping processes discussed in chapter 5. In each saturated trap, the amount of newly arriving particles balances the amount of released particles, and thus the net flux of particles into a saturated trap equals zero. New traps are only visited by particles when preceding traps are saturated. The physical beauty of the cascade is accentuated by the Greek poet and musician Arion in the foreground. The cascade of Arion can be found in Rijksmuseum Paleis Het Loo, Apeldoorn, The Netherlands. Photo: M. Heuff. Copyright: Rijksmuseum Paleis Het Loo.

CIP-GEGEVENS KONINKLIJKE BIBLIOTHEEK, DEN HAAG

Filius, Hans Adriaan

Defects in nuclear fusion reactor materials studied by thermal gas desorption spectrometry /
Hans Adriaan Filius. - Delft: Interfacultair Reactor Instituut, Delft University of Technology. - Ill.
Thesis Technische Universiteit Delft. - With ref. -With summary in Dutch.
ISBN 90-73861-10-1
NUGI 812
Subject headings: gas desorption / nuclear materials.

Copyright © 1992 by H.A. Filius

DEFECTS IN NUCLEAR FUSION REACTOR MATERIALS

STUDIED BY

THERMAL GAS DESORPTION SPECTROMETRY

PROEFSCHRIFT

TER VERKRIJGING VAN DE GRAAD VAN DOCTOR AAN
DE TECHNISCHE UNIVERSITEIT DELFT, OP GEZAG VAN
DE RECTOR MAGNIFICUS, PROF. DRS. P.A. SCHENCK,
IN HET OPENBAAR TE VERDEDIGEN TEN OVERSTAAN
VAN EEN COMMISSIE DOOR HET COLLEGE VAN DEKANEN
DAARTOE AANGEWEZEN, OP 1 DECEMBER 1992 TE 19.00 UUR.

door

HANS ADRIAAN FILIUS

geboren te Vlissingen
natuurkundig ingenieur

Dit proefschrift is goedgekeurd door de promotoren:

Prof. dr. ir. H. van Dam,
Prof. dr. A. van Veen.

The following copyright holders have kindly granted their permission to reproduce parts of previously published material:

North Holland Publishing Company, Amsterdam,
Gordon and Breach, Science Publishers, Inc., London.

The research described in this thesis has been performed at the Reactor Physics Department of the Interfaculty Reactor Institute of the Delft University of Technology, Mekelweg 15, 2629 JB Delft, The Netherlands.

Aan mijn ouders

CONTENTS

1. INTRODUCTION
   1.1 Nuclear fusion reactor materials 15
      1.1.1 Nuclear fusion reactors 15
      1.1.2 Requirements for fusion reactor materials 16
      1.1.3 Selection of fusion reactor materials 17
   1.2 Defects in fusion reactor materials 19
      1.2.1 Defect creation 19
      1.2.2 Defect migration and growth 21
      1.2.3 Defect dissociation 23
   1.3 Thermal gas desorption spectrometry 26
      1.3.1 General 26
      1.3.2 Thermal helium desorption spectrometry 26
   1.4 Outline 27

2. EXPERIMENTAL DETAILS
   2.1 Introduction 31
   2.2 Specimen preparation 32
   2.3 Controlled defect production and modification 32
   2.4 Defect dissociation 35
   2.5 Positron annihilation 37
   2.6 A spectrometer for ion irradiation induced desorption 38
   2.7 A spectrometer for hydrogen permeation experiments 39

3. THE INTERACTION BETWEEN SELF-INTERSTITIALS AND ARGON IN MOLYBDENUM
   3.1 Introduction 47
   3.2 The production of self-interstitial atoms 48
      3.2.1 Experimental results 48
      3.2.2 Discussion 51
   3.3 The influence of self-interstitials on the retention of argon in high fluence argon irradiated molybdenum 53
      3.3.1 Introduction 53
      3.3.2 Experimental results 55
      3.3.3 Discussion 56
   3.4 A comparison with silicon 58
      3.4.1 Introduction 58
      3.4.2 Experimental results 58
      3.4.3 Discussion 60
   3.5 Conclusions 62

4. THE INTERACTION OF VACANCIES WITH HYDROGEN AND NITROGEN IN MOLYBDENUM
4.1 Introduction 65
4.2 The annealing behaviour of monovacancies in molybdenum . . . 65
4.2.1 Introduction 65
4.2.2 Data analysis 66
4.2.3 Experimental results 68
4.2.4 Discussion 70
4.3 The interaction between monovacancies and hydrogen in molybdenum 71
4.3.1 Introduction 71
4.3.2 Experimental results 71
4.3.3 Discussion 72
4.4 The interaction between monovacancies and nitrogen in molybdenum 74
4.4.1 Introduction 74
4.4.2 Positron annihilation results 74
4.4.3 Helium filling of suspected NV defects 77
4.4.4 Reduction of suspected NV defects by self-interstitials . 79
4.4.5 Theoretical considerations 81
4.5 The interaction between vacancy clusters and nitrogen in molybdenum 83
4.5.1 Introduction 83
4.5.2 Positron annihilation results 83
4.5.3 The production of defect clusters that survive a 1005 K anneal 83
4.5.4 Nature of defect clusters that survive a 1005 K anneal . 87
4.6 Conclusions 89

5. THE INTERACTION BETWEEN HYDROGEN AND VOIDS IN TUNGSTEN
5.1 Introduction 93
5.2 Theoretical model for the hydrogen-void interaction 94
5.2.1 The metal-hydrogen system 94
5.2.2 Void saturation 96
5.3 Application of the model 99
5.3.1 Experimental details 99
5.3.2 Experimental results 100
5.3.3 Discussion 101
5.3.4 A comparison with deuterium in molybdenum 103
5.4 Conclusions 105

6. MISCELLANEOUS EXPERIMENTS
6.1 Introduction 109
6.2 Helium precipitates in molybdenum 109
6.2.1 Introduction 109
6.2.2 The conversion of helium platelets into bubbles 110
6.2.3 The interaction between helium precipitates and self-interstitials 111
6.2.4 The interaction between helium precipitates and heavy noble gas atoms 113
6.3 Helium in austenitic stainless steel 114
6.3.1 Introduction 114
6.3.2 Experimental results 115
6.3.3 Discussion 117
6.4 Ion irradiation induced desorption 119
6.4.1 Introduction 119
6.4.2 Survey of previous research 120
6.4.3 Preliminary test experiments on the new impact desorption spectrometer 121
6.4.4 Future developments 124

SUMMARY 129

SAMENVATTING 133

ACKNOWLEDGEMENTS 137

CURRICULUM VITAE 139

The contents of this thesis have partly been published in the following articles:

- *Self-interstitials generated by low energy heavy ion bombardment of metals.* A. van Veen, G.J. van der Kolk, H.A. Filius, K.T. Westerduin and L.M. Caspers, Nucl. Instr. and Meth. B **2** (1984) 779.
- *The retention of Ar in Low energy high fluence Ar-irradiated Mo and Si.* H.A. Filius and A. van Veen, Radiation Effects and Defects in Solids **108** (1989) 1.
- *On the trapping and thermal release of low energy noble gases implanted into silicon.* A. van Veen, P.C. de Jong, K.R. Bijkerk, H.A. Filius and J.H. Evans, in: Fundamentals of Beam-Solid Interactions and Transient Thermal Processing, eds. M.J. Aziz, L.E. Rehn and B. Stritzker, Proc. Mat. Res. Soc. **100** (MRS, Pittsburg, Pensylvania, 1988) p. 231.
- *Vacancy Annealing in He and H_2 irradiated Mo observed by thermal helium desorption spectrometry.* T.R. Armstrong, A. van Veen, J.R. Heringa, H.A. Filius. In press.
- *The interaction between nitrogen and defects in Mo studied by the positron annihilation technique.* B. Nielsen, A. van Veen, L.M. Caspers, H.A. Filius, H.E. Hansen and K. Petersen, in: Positron Annihilation, eds. P.G. Coleman, S.C. Sharma, L.M. Diana (North Holland, Amsterdam, 1982), p. 438.
- *The interaction between nitrogen and vacancies in molybdenum observed with thermal helium desorption spectrometry.* H.A. Filius and A. van Veen. J. Nucl. Mater. **144** (1987) 1.
- Hydrogen exchange with voids in tungsten observed with TDS and PA. A. van Veen, H.A. Filius, J. de Vries, K.R. Bijkerk, G.J. Rozing and D. Segers. J. Nucl. Mater. **155-157** (1988) 1113.
- *Trapping and detrapping of deuterium and hydrogen in neutron irradiated molybdenum.* D.T. Britton, K.R. Bijkerk, A. van Veen, J.R. Heringa, H.A. Filius, J. de Vries, J.H. Evans and W. Segeth, in: Fusion Technology 1988, eds. A.M. van Ingen, A. Nijsen-Vis and H.T. Klippel (North Holland, Amsterdam, 1989) 924.

Chapter 1
Introduction

1.1 Nuclear fusion reactor materials

1.1.1 Nuclear fusion reactors

Controlled thermonuclear reactors, briefly called nuclear fusion reactors, may provide a long term solution to the world energy problem. These reactors, based on the fusion of light nuclei at temperatures exceeding 10^8 K by which energy is released in the form of kinetic energy of neutrons or charged particles, are envisaged to compensate for dwindling supplies of fossil fuels and the eventual depletion of fissionable uranium used in present-day nuclear reactors. The fusion reaction which requires the lowest ignition temperature is the $T(d,n)^4He$ reaction[1]. Since the energy released in this reaction is very high (17.58 MeV), deuterium and tritium are destined to be the most likely fuels for nuclear fusion reactors. Deuterium is easily extractable from the surface waters of the earth, and tritium, although not naturally abundant because of its decay with a half-life of 12.26 years, can be produced from lithium which is extractable from sea water as well as from land deposits. In a nuclear fusion reactor no chemical combustion products will be released to produce acid rain or greenhouse effects, a runaway reaction (meltdown) will be impossible, and radioactive waste can be minimized by carefully selecting the nuclear fusion reactor construction materials.

Before controlled thermonuclear reactors can become operative two major problems have to be solved. The first one is to meet the Lawson criterium, which dictates that the product of nuclei density and nuclei confinement time must equal at least 10^{20} $m^{-3}.s$ at a temperature of 10^8 K to make self sustained fusion technically feasible. The second is that in an ignited fusion reactor the radiation environment and the power loading of the reactor components are such that none of the presently available construction materials possess the properties that are required for these components[2].

International collaboration on these problems involving 20,000 scientists[3] has led to several large scale experimental fusion machines of which the most important are JET (Joint European Tokamak), TFTR (Tokamak Fusion Test Reactor, United States), JT-60 (Japan Atomic Energy Research Institute Tokamak 60), and T-15 (Soviet Union). All these machines have a similar structure[4] which is schematically shown in fig. 1.1. In November 1991 it was shown in the JET reactor that with the present generation machines a fusion reaction is technically feasible. A next generation reactor, called ITER (International Thermonuclear Experimental Reactor), will have to demonstrate

that long term self sustained fusion can be controlled and that its construction materials are resistent to long term operation. Considering its cost of 5 Gecu, ITER is envisaged to be a global collaboration between all the countries involved in fusion research so far, under the auspices of the IAEA (International Atomic Energy Agency)[5].

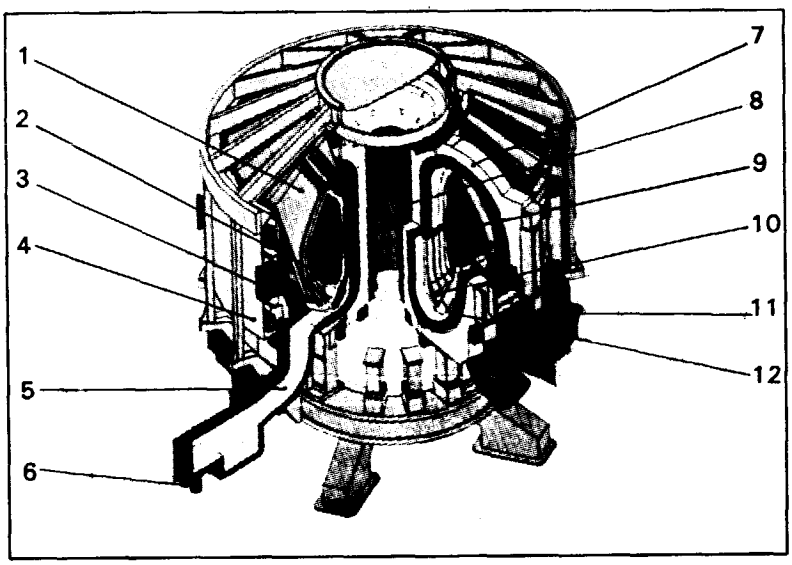

Fig. 1.1. Design of the NET reactor. The main components are: (1) blanket, (2) first wall, (3) shield, (4) crysostat, (5) plasma exhaust, (6) vacuum pump, (7) toroidal field coils, (8) inner poloidal coils, (9) plasma, (10) outer poloidal coils, (11) divertor plates, (12) active control coils. Source: P. Schiller and J. Nihoul[4].

1.1.2 Requirements for fusion reactor materials

The fusion reactor components that are mostly affected by irradiation with energetic particles that emerge from the plasma in which the fusion takes place are[2,4]: the plasma facing components (*i.e.* the first wall, the limiters that control the plasma shape, the divertor dump plates that serve to extract impurities from the plasma, and the launchers used for plasma heating), the blanket (which serves to breed tritium and to slow down the high energy neutrons in order to generate heat for power production), the superconducting magnets (which confine the plasma), and the radiation shield.

The cumulative neutron fluence in a T(d,n)^{4}He reactor may result in a cumulative energy deposition of 40 MW yr/m^2, which can lead to radiation damage levels of up to 200 dpa (displacements per atom)[4]. This neutron radiation, and to a lesser extent the D, T, and alpha radiation, cause thermal

conductivity changes, hardening, embrittlement (decrease in ductility), creep, void swelling, activation (which forms a decisive issue in determining the public acceptability of fusion energy) and heating. The heat flux may exceed 5 MW/m^2, and some of the components will reach temperatures of 1200 K[4]. The high thermal load leads to temperature gradients which induce large thermal stresses, and due to pulsed operation of the reactor it also leads to thermal fatigue (especially at joints of dissimilar materials).

One of the biggest problems forms erosion and redeposition of the plasma facing components[6]. Erosion occurs through physical sputtering, chemical erosion, melting, sublimation, or (to a lesser extent) blistering followed by exfoliation, and is detrimental for both the plasma and the components. It introduces impurities in the plasma that cause high radiative power losses and reduction of the fusion yield by dilution of the fusion reactants[7].

Another problem is posed by the permeation and retention of tritium in the reactor materials. For environmental and economic reasons should these be kept as low as possible.

The ideal material is therefore a low activation, high temperature resistant, UHV (ultra high vacuum) compatible material, which is easily machinable, with a radiation resistance up to 200 dpa, a high thermal conductivity, a high fatigue resistance, and a low tritium permeability and retention[4,8].

1.1.3 Selection of fusion reactor materials

Initially, the first walls of the experimental fusion reactors were made of metal (in JET[9] the nickel based alloy Nicrofer 7612LC was used, in JT-60[10] and TFTR[11] molybdenum or Inconel coated with 20 μm TiC). However, plasma disruptions that could leed to an energy deposition of 5 to 10 MJ/m^2 in 0.1 to 1.0 ms[6], or runaway electrons (>20 MeV) that could deposit 80 MJ/cm^2 [12], caused severe erosion and subsequent metal atom contamination of the plasma.

Substantial parts of the inner walls of JET, TFTR and JT-60 have therefore been clad with graphite[13], being a low density, low-Z (low atomic number) material. In these materials electrons deposit their energy in a much larger volume than in metals (the penetration depth in graphite is 15 cm for 20-40 MeV electrons), and low-Z element contamination in the plasma leads to less radiative power loss than high-Z element contamination. Besides, graphite has a high sublimation temperature, a low thermal expansion, and a good compressive strength. Unfortunately, graphite has a tendency to loose its integrity and thermal conductivity under high energy neutron irradiation, it has a high potential tritium inventory, it may react chemically with hydrogen, it is a brittle material that can experience sudden crack growth, and the attachment of graphite tiles is not without problems[14,15].

In future generation reactors like ITER, thermal excursions due to plasma disruptions and runaway electrons will be solved[3], and graphite will then no longer be the prime candidate. The neutron fluences in future generation reactors will be considerably higher than in present generation reactors, and the major problems then will be posed by[16] thermal load, radiation damage and radioactive waste. For these reactors, metal components will be preferred instead of graphite. Metals have a better resistance to neutron damage than graphite, are chemically inert to hydrogen, have superior fracture toughness, and well developed fabrication techniques.

Most metals are not eligible though. Metals in which hydrogen is dissolved exothermically, such as tantalum and titanium, exhibit a too high hydrogen affinity, while moderate atomic number metals such as stainless steel and copper possess insufficient high temperature properties, have high sputtering rates, and cause serious radiative power losses when contaminating the plasma[4]. Copper is considered for divertor plates however because of its high thermal conductivity and strength.

The favourite candidates for the plasma facing components are alloys based on tungsten[17] and molybdenum. These high-Z materials have a relatively high threshold energy for sputtering by light ions, have excellent thermal properties (*e.g.* the melting point of W is 3683 K, of Mo 2890 K) and relatively low tritium retention. However, to avoid sputtering and subsequent plasma contamination, their use is restricted to reactors with extremely low plasma edge temperatures (<50 eV). If it will turn out to be impossible to attain and maintain these low edge temperatures, an alternative may be beryllium[18]. Being a low-Z element, beryllium causes less radiative power loss when contaminating the plasma, an advantage which may be countered by the fact that beryllium exhibits higher erosion rates and is susceptible to swelling due to the Be(n,2n)2He reaction which produces large amounts of He. Other candidates are alloys based on vanadium. Vanadium is a low activation material, has a good resistance to void and cavity swelling, a low neutron absorption, a high thermal conductivity and a low thermal expansion[19,20]. Its disadvantage is its poor oxidation resistance.

As a structural material for the blanket and the radiation shield of ITER, austenitic stainless steel 316L has been considered because of its extensive data base and ease of fabrication[21]. Another candidate for the radiation shield is tungsten because of its high density.

1.2 Defects in fusion reactor materials

1.2.1 Defect creation

The property changes of fusion reactor materials under irradiation conditions are predominately caused by the nucleation and growth of point defects in the materials. The main point defects in fusion reactor materials are: self-interstitial atoms, vacancies, interstitial and substitutional impurities, and clusters of these. At the temperatures at which a fusion reactor is operated, point defects will be able to migrate and agglomerate, thus forming extended defects. In chapter 3 *e.g.* it is shown that when self-interstitial atoms form clusters, platelets of self-interstitials are produced which give rise to dislocation loops (or dislocation segments when both ends of the dislocation don't join). Similarly, so-called voids are produced in the material when large numbers of vacancies form clusters. Vacancies or clusters of vacancies may also contain gas atoms that exert a pressure on the surrounding matrix. When the vacancy clusters are stabilized by their internal gas pressure, they are called gas bubbles (or gas platelets when they are two-dimensional).

In the thermal gas desorption experiments discussed in this thesis, the defects have generally been created by ion bombardment. When, due to ion bombardment, an ion impinges on a crystalline material, the energy E_1 transferred by the impinging ion to a lattice atom is given by the classical collision equation

$$E_1 = \frac{4m_1m_2}{(m_1+m_2)^2}\cos^2\phi \; E_0, \qquad (1.1)$$

where m_1 is the mass of the impinging ion, m_2 the mass of the lattice atom, ϕ the scattering angle of the lattice atom, and E_0 the kinetic energy of the ion. If the transferred energy is more than the threshold energy that is required to create a Frenkel pair (*i.e.* a self-interstitial atom and a vacancy), defects will be created in the lattice. This threshold energy (or minimum displacement energy) E_d is about 40 eV for W and 34 eV for Mo[22].

A single impinging ion may trigger off a cascade of collision sequences[23], thus initiating a process by which substantial amounts of Frenkel pairs are created. Most of the created vacancies and self-interstitials will recombine spontaneously however, if their mutual distance is less then a certain recombination radius r_c (in Mo r_c equals 1.16 nm)[24]. The recombination process takes place within $\sim$1 ps (depending on the temperature), and therefore the exact volume over which a collision cascade extends is ill-defined. The fact that there is no thermal equilibrium during the collision

cascade process implies that areas under heavy bombardment are not amenable to ordinary thermodynamic laws.

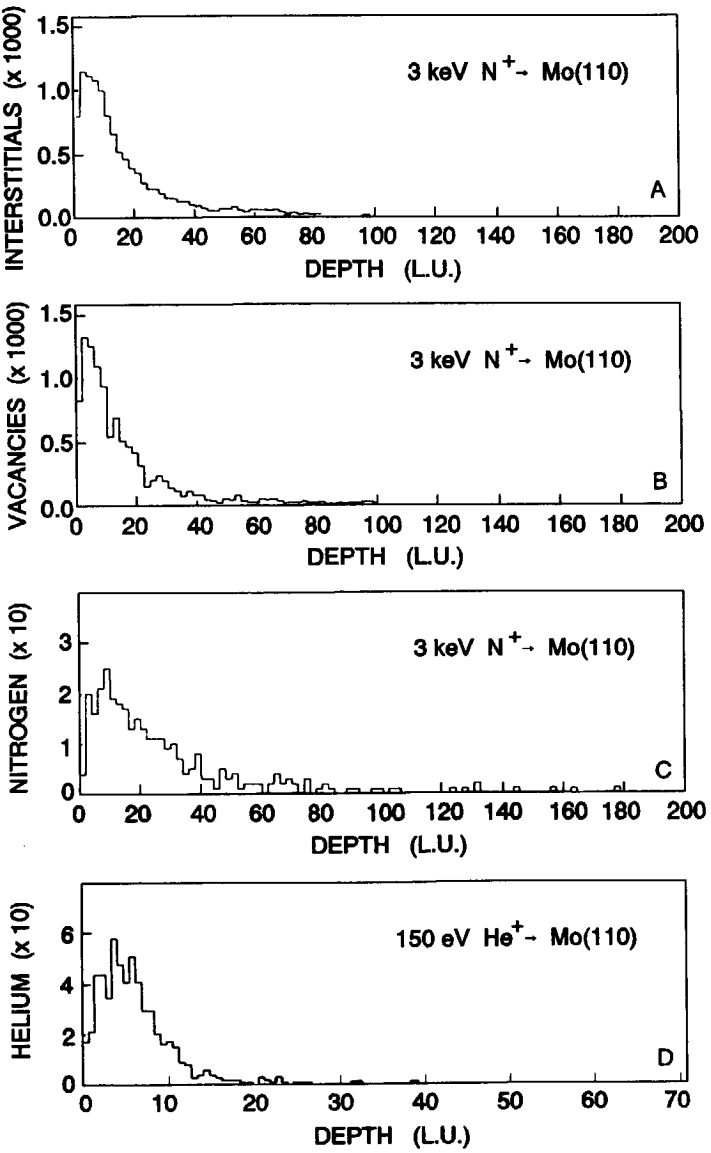

Fig. 1.2. Depth distribution of point defects created in a Mo(110) single crystal by 400 3 keV N^+ ions, as calculated with the computer code MARLOWE. The depth is given in lattice units of 0.314 nm. (A) self-interstitial distribution, (B) vacancy depth distribution, (C) nitrogen depth distribution, (D) helium depth distribution after irradiating a Mo(110) single crystal with 1000 150 eV He^+ ions.

In crystalline materials the successive energy transfer of one lattice atom to another may cause a linear chain of atom replacements. The symmetrical repelling forces of surrounding atoms will ensure that this so called "replacement collision sequence" remains linear. The net result is a vacancy located at the beginning of the chain and a self-interstitial at the end of the chain.

The range of the impinging ion in the lattice and the amount of damage created can be calculated on the basis of the energy transferred to lattice atoms[25]. Note that energy is transferred to both lattice nuclei (nuclear stopping) and lattice electrons (electronic stopping). To calculate ion ranges and produced damage in an amorphous material, Biersack and Haggmark[26] have developed the Monte Carlo computer code TRIM. For a crystalline material, Torrens and Robinson[27] have developed the computer code MARLOWE. As an example of the MARLOWE calculations, fig. 1.2 shows the depth distribution of various point defects after irradiating a Mo(110) single crystal with 3 keV nitrogen and 150 eV helium ions.

1.2.2 Defect migration and growth

If the temperature is high enough, defects in a material will be able to migrate. The concentration c_i of a defect type i at a certain depth x and time t will be dependent on the diffusion behaviour, the defect production rate I(x,t), association of defects (by which defect i may be formed or disappear), and dissociation of defects (by which defect i may also be formed or disappear). Thus, for the one-dimensional transport of defects in a material, the diffusion equation is given by[28]:

$$\frac{\partial c_i(x,t)}{\partial t} = \frac{\partial}{\partial x}\left(D\frac{\partial c_i(x,t)}{\partial x}\right) + I(x,t)$$

$$+ \sum_{k,l} K_{k+l\rightarrow i} c_k c_l - \sum_m K_{m+i\rightarrow n} c_i c_m \quad \text{(association)}$$

$$+ \sum_p K_{p\rightarrow i+q} c_p - \sum_r K_{i\rightarrow r+s} c_i \quad \text{(dissociation)} \qquad (1.2)$$

where D is the diffusivity, and $K_{a+b\rightarrow c+d}$ the reaction constant for the process a+b → c+d. The concentration c_i is expressed in atomic fraction. The diffusivity D is given by

$$D = \frac{1}{6}\lambda^2 \nu_o \exp\frac{S^M}{k} \exp-\frac{E^M}{kT}, \qquad (1.3)$$

where λ and v_o denote respectively the average jump distance and the average jump frequency, S^M is the migration entropy, k is Boltzmann's constant, T the absolute temperature, and E^M the defect migration energy (for most metals, the hydrogen migration energies vary from 0.2 to 0.5 eV[29]; the helium migration energy is about 0.3 eV in bcc metals and 0.5-0.7 eV in fcc metals[30]). The reaction constants K can be expressed by

$$K = z v_o e^{\frac{S}{k}} e^{-\frac{E}{kT}}, \tag{1.4}$$

with z a geometrical factor related to the size of the defects[31], and E the activation energy required for the association or dissociation process.

If no other defects are present, the association and dissociation terms disappear, and the diffusion equation may be solved analytically. *E.g.* for a stationary gas concentration c_o at the crystal surface, the solution is[32]:

$$\frac{c_d(x,t)}{c_o} = 1 - erf\frac{x}{2\sqrt{Dt}}. \tag{1.5}$$

In the case that particles are implanted into a crystal and they are able to diffuse, a stationary situation will be established after some time. Van Veen and Caspers have shown that in the case that the influence of other defects is negligible, the concentration of implanted particles beyond the mean implantation depth L then becomes[33]:

$$c_d = \frac{\theta J L}{D N_o}, \tag{1.6}$$

where J is the flux of particles arriving at the surface, θ the probability that the particles penetrate into the sample (a considerable fraction is backscattered by surface atoms), and N_o the atomic density of the crystal; c_d is expressed in atomic fraction. Equation 1.6 can easily be understood by realizing that in the stationary situation the flux of incoming particles θJ should balance the flux of particles diffusing to the surface. The latter is given by Fick's law and equals $DN_o c_d/L$ (see fig. 1.3; the concentration gradient beyond the implantation depth L is negligible compared to that below L).

It has been shown by Van Veen *et al.*[34] that vacancy type defects may form unsaturable traps for helium atoms. The helium atoms trapped in these defects may exert such a pressure that lattice atoms are pushed out to become self-interstitials, thereby providing space for more helium atoms. This process may occur repeatedly, and Evans *et al.*[35,36,37] have demonstrated

that thus helium platelets may grow by pushing out complete platelets of self-interstitials, a mechanism which had previously been suggested by Greenwood *et al.*[38]. The unsaturability of traps for helium implies that helium permeates over considerably shallower distances in fusion reactor materials than *e.g.* hydrogen.

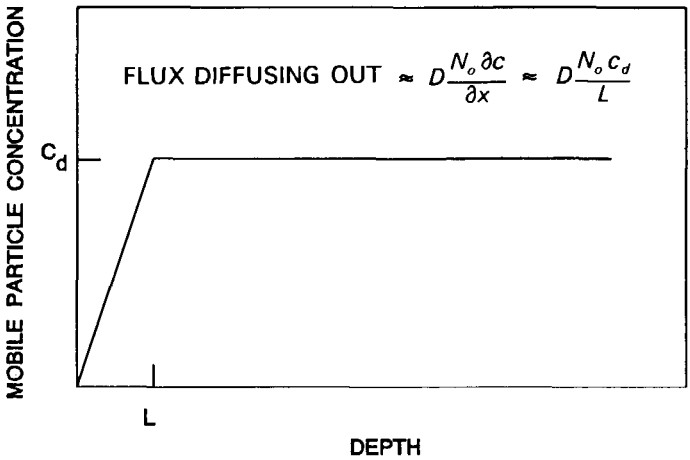

Fig. 1.3. Concentration profile of implanted particles during implantation. See text for denotation.

1.2.3 Defect dissociation

The dissociation of a compound defect generally requires energy. In this section it is shown how this dissociation energy E^D can be deduced from the formation energy E^F.

The formation energy E_i^f of a defect i is the difference in potential energy of a crystallite with and without the defect. If two defects are bound to each other, their binding energy E_i^B is the difference in formation energy between the separate defects and the bound defect. *E.g.* for a HeV (a helium atom bound to a vacancy):

$$E^B_{HeV} = E^F_{He} + E^F_V - E^F_{HeV}. \tag{1.7}$$

The dissociation energy E^D equals the binding energy plus the migration energy of the least bound constituant:

$$E^D = E^B + E^M. \tag{1.8}$$

As an example, fig. 1.4 shows the various energies for the systems nitrogen-molybdenum and helium-molybdenum. Formation, binding and dissociation energies can be calculated by using interatomic potentials (as is done in the computer code RELAX developed by Caspers *et al.*[39]), by applying the "atom embedding theory" in which a defect is assumed to be embedded in the electron gas formed by the surrounding atoms[40,41,42], or by using the Miedema model[43].

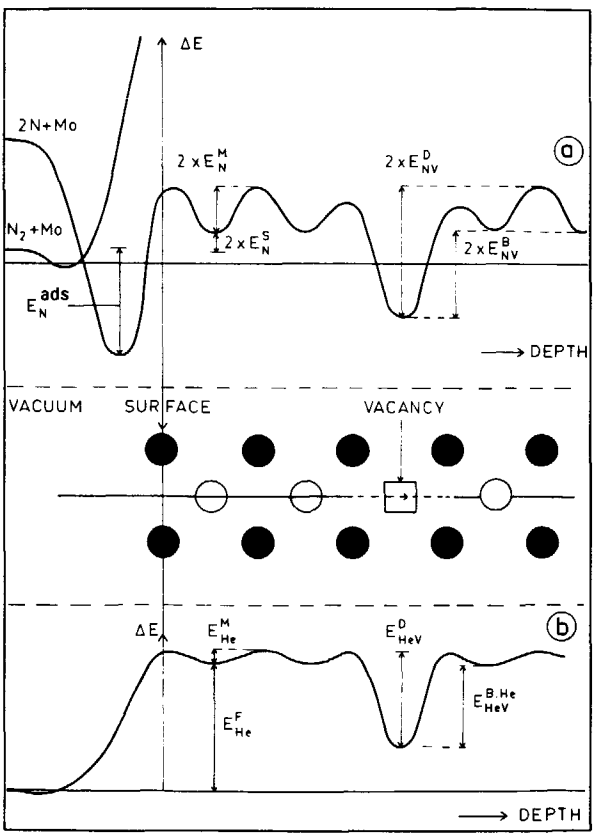

Fig. 1.4. Qualitative energy diagram for (a) the system nitrogen-molybdenum and (b) the system helium-molybdenum. The nitrogen diagram is depicted for two nitrogen atoms, which in vacuum form a molecule. Upon approaching the molybdenum surface, the molecule dissociates and the atoms become adsorbed with adsorption energy E_N^{ads}. The net energy required to bring a nitrogen atom in an interstitial position in the molybdenum matrix (i.e. the formation energy or the heat of solution) is denoted as E_N^S. The energy required to dissociate a nitrogen atom from a vacancy E_{NV}^D equals the binding energy of a nitrogen atom to a vacancy E_{NV}^B plus the migration energy E_N^M. The helium diagram is given for one helium atom. Here, molecule formation does not occur and surface adsorption is very weak. Source: A. Van Veen and L.M. Caspers[45].

As an illustration, it is shown here how the Miedema model can be used to approximate the binding energy of vacancy clusters. Assume that a vacancy cluster V_k consisting of k vacancies is spherical with radius r_k, and that its volume equals k times the volume occupied by one vacancy Ω, then

$$\frac{4}{3}\pi r_k^3 = k\Omega. \tag{1.9}$$

Furthermore, assume that the formation energy $E_{V_k}^f$ increases linearly with the surface of the sphere according to

$$E_{V_k}^f = \gamma 4\pi r_k^2 \tag{1.10}$$

where γ is a proportionality constant. Then, the binding energy $E_{V_k}^{B,V}$ of one vacancy is given by

$$E_{V_k}^{B,V} = E_V^f + E_{V_{k-1}}^f - E_{V_k}^f = E_V^f + \gamma'((k-1)^{\frac{2}{3}} - k^{\frac{2}{3}}) \tag{1.11}$$

where $\gamma' = \gamma(4\pi)^{\frac{1}{3}}(3\Omega)^{\frac{2}{3}}$. Equation 1.11 shows that for high values of k the binding energy $E_{V_k}^{B,V}$ approaches E_V^f. For low values of k the vacancy cluster is not spherical and in that case equation 1.11 is not valid.

Another illustration is the use of formation energies to predict so-called reduction reactions. Defects may be reduced by other defects, when such a reduction reaction is exothermal. Consider *e.g.* the reaction

$$NV + I \rightarrow N \tag{1.12}$$

where NV denotes a compound defect consisting of a nitrogen atom and a vacancy (*i.e.* a substitutional nitrogen atom), I is an interstitial atom, and N an interstitial nitrogen atom. This so-called "kick-out" reaction only occurs if

$$E_{NV}^f + E_I^f > E_N^f. \tag{1.13}$$

It can be shown that this condition is satisfied for Mo, since

$$E_{NV}^f + E_I^f = E_N^f + E_V^f - E_{NV}^{B,N} + E_I^f \tag{1.14}$$

where $E_V^f + E_I^f$ is the Frenkel pair energy in Mo, *i.e.* 9.6 eV[44], and $E_{NV}^{B,N} = E_{NV}^{D,N} - E_N^M = 2.55$ eV[45]-1.2 eV[46] = 1.35 eV. For HeV defects (*i.e.* substitutional helium atoms) in Mo the same can be deduced, because

$E_{HeV}^{D,He} = 3.8$ eV[47] and $E_{He}^{M} = 0.17$ eV[48]. On the other hand, it is impossible to annihilate He_8V defects by self-interstitials[47].

1.3 Thermal gas desorption spectrometry

1.3.1 General

To investigate the processes that govern the creation and spatial distribution of defects in fusion reactor materials, a wide range of techniques is utilized such as resistivity measurements, scanning and transmission electron microscopy, scanning tunneling microscopy (STM), Rutherford backscattering, Mössbauer spectrometry, Auger electron spectroscopy (AES), perturbed angular correlation (PAC), and the positron annihilation technique (PAT).

Among these techniques, a special position is taken by thermal gas desorption spectrometry (TDS), by which the history of gaseous species in fusion reactor materials can be monitored. Gases are not only present because the plasma facing materials are subjected to intense deuterium, tritium or helium ion bombardment, they are also introduced in large quantities due to (n,p) and (n,α) reactions. Gaseous impurities may occur up to 1000 ppm[49], which will substantially contribute to the formation and stabilization of the defects.

In the early seventies, it was realized by Kornelsen that thermal gas desorption spectrometry, apart from supplying information about gaseous impurities, can also provide a unique possibility to investigate point defects that are present at extremely low concentrations[50]. For this purpose, Kornelsen developed the thermal helium desorption spectrometry technique (THDS) with which the creation and controlled growth of subsurface defects can be monitored up to depths of 100 nm by using helium as a probe. The technique was further developed by Van Veen[51,52]. Due to the THDS technique, thermal gas desorption spectrometry became a powerful tool in providing information about fusion reactor materials that is complementary to that obtained by other techniques[47,53,54].

1.3.2. Thermal helium desorption spectrometry

The THDS technique is based on the fact that helium is very mobile in metals at or above room temperature, and only present in states bound to defects. By following the desorption of helium during a temperature ramp, the binding energies of helium trapped by defects can be determined, and thus different types of defects can be identified. The most straightforward THDS experiment would take the following form:

(1) irradiation of a sample by energetic ions (1 keV-5 keV) to create defects (defects can also be created by *e.g.* laser exposure or plastic deformation[66]);
(2) decoration of the formed defects by low energy helium ion irradiation (in Mo 150 eV is used, well below the damage threshold of 200 eV);
(3) monitoring of the helium release temperature during thermal ramp annealing.

One of the benefits of the THDS technique is its versatility. For example, between steps 1 and 2 the original defects can be modified or removed by annealing treatments. Any changes in defect structure will then be reflected in the desorption spectra of the helium introduced subsequently in step 2.

It might be expected that the helium dose used in step 2 should be sufficient to decorate traps by single helium atoms on the average. However, from previous experiments it is known that when further helium is added, the helium itself may be able to modify certain types of defects. Further helium filling can therefore be helpful in identifying these types of defects.

1.4 Outline

The main aim of the presently described study is to explore and demonstrate the versatility of thermal gas desorption spectrometry as a tool to investigate the interaction between gaseous impurities and point defects in nuclear fusion reactor materials. Taking into account the material selection considerations of section 1.1.3, emphasis in this study is laid on molybdenum and tungsten, although other materials have been studied as well for comparison reasons. The gases chosen are those that are present in fusion reactors in the form of fuel, reaction products or residual UHV gases. The defects investigated range from interstitial atoms and single vacancies to voids and gas pressurized bubbles.

In chapter 2 the experimental details are described, which include specimen preparation, controlled defect production, defect modification, defect analysis and data handling; this chapter also presents two novel gas desorption spectrometers, which have been developed for experiments on ion irradiation induced desorption and hydrogen isotope permeation. Chapter 3 is dedicated to self-interstitial atoms, their production, their coalescence, and their interaction with gaseous impurities. Chapter 4 is devoted to vacancies and the interaction of vacancies and vacancy clusters with hydrogen and nitrogen. Chapter 5 is allotted to the interaction between voids and hydrogen isotopes; voids form very potent traps for hydrogen isotopes and exert a profound influence on the hydrogen isotope permeation and hydrogen isotope inventory in fusion reactor materials. Chapter 6 finally describes miscellaneous experiments on the precipitation of helium in molybdenum, on the trapping of

helium in stainless steel, and on ion irradiation induced desorption of volatile species from stainless steel surfaces.

References chapter 1

1. E. Teller, Fusion, Vol. 1: Magnetic Confinement (Academic Press, New York, 1981) p. 5.
2. S. Amelinckx, J. Nucl. Mater. **155-157** (1988) 3.
3. D.H. Crandall, Nucl. instr. Methods B **42** (1989) 409.
4. P. Schiller and J. Nihoul, J. Nucl. Mater. **155-157** (1988) 41.
5. K. Tomabechi, J. Nucl. Mater. **179-181** (1991) 1173.
6. J.B. Whitley, K.L. Wilson and D.A. Buchenauer, J. Nucl. Mater. **155-157** (1988) 82.
7. R.C. Isler, Nucl. Fusion **24** (1984) 1599.
8. R. Behrisch and J. Ehrenberg, J. Nucl. Mater. **155-157** (1988) 95.
9. K.J. Dietz, J. Nucl. Mater. **155-157** (1988) 8.
10. H. Takatsu, T. Ando, M. Yamamoto, T. Arai, K. Kodama, M.Ohkubo, M. Shimizu and the JT-60 Team, J. Nucl. Mater. **155-157** (1988) 27.
11. H.F. Dylla, M.A. Ulrickson, D.K. Owens, D.B. Heifetz, B.E. Mills, A.E. Pontau, W.R. Wampler, B.L. Doyle, S.R. Lee, R.D. Watson and C.D. Croessmann. J. Nucl. Mater. **155-157** (1988) 15.
12. J.B. Whitley, J.A. Koski and R. Aymar, in: Proc. 14th Symp. on Fusion Technology (Avignon, 1986).
13. M. Seki, M. Guseva, G. Vieider and J. Whitley, J. Nucl. Mater. **179-181** (1991) 1189.
14. A. Miyahara and T. Tanabe, J. Nucl. Mater. **155-157** (1988) 49.
15. N. Itoh and K. Morita, J. Nucl. Mater. **155-157** (1988) 58.
16. P. Schiller, K. Ehrlich, J. Nihoul, J. Nucl. Mater. **179-181** (1991) 13.
17. Y. Hiraoka, M. Fujitsuka, T. Fujii, J. Nucl. Mater. **179-181** (1991) 275.
18. J. Roth, W. Eckstein, E. Gauthier and J. Laszlo, J. Nucl. Mater. **179-181** (1991) 34.
19. D.L. Smith, J. Nucl. Mater. **122&123** (1984) 51.
20. B.A. Loomis, A.B. Hull and D.L. Smith, J. Nucl. Mater. **179-181** (1991) 148.
21. J.L. Boutard, J. Nucl. Mater. **179-181** (1991) 1179.
22. P. Jung, Rad. Eff. **35** (1978) 155.
23. See *e.g.* C.A. English, Radiation Effects and Defects in Solids **113** (1990) 15.
24. M. Hou, A. van Veen, L.M. Caspers and M.R. Ypma, Nucl. Instr. and Meth. **209/210** (1983) 19.
25. G. Carter and J.S. Colligon, Ion bombardment of Solids (Heinemann, London, 1968).
26. J.P. Biersack and L.G. Haggmark, Nucl. Instr. and Meth. **174** (1980) 257.
27. M.T. Robinson and I. Torrens, Phys. Rev. B **9** (1974) 5008.

28. See *e.g.* A. van Veen, in: Erosion and Growth of Solids stimulated by Atom and Ion Beams, eds. G. Kiriakidis, G. Carter and J.L. Whitton (Nijhoff Publishers, Dordrecht, 1986) p. 200.
29. J. Volkl and G. Alefeld, in: Diffusion in Solids; Recent Developments, eds. A.S. Nowick and J.J. Burton (Academic Press, Oxford, 1975) ch.3.
30. M.I. Baskes and C.F. Melius, Phys. Rev. B **20** (1979) 3197.
31. R.H.J. Fastenau, A. van Veen, P. Penning, L.M. Caspers, Phys. Stat. Sol. (a) **47** (1978) 577.
32. H.S. Carslaw and J.C. Jaeger, Conduction of Heat in Solids, (Oxford, 1948).
33. A. van Veen and L. M. Caspers, in: Proc. Consultants Symp. on Inert Gases (AERE report 9733, Harwell, 1980) p. 494.
34. A. van Veen, L.M. Caspers, E.V. Kornelsen, R.H.J. Fastenau, A.A. van Gorkum and A. Warnaar, Phys. Stat. Sol. (a) **40** (1977) 235.
35. J.H. Evans, A. van Veen and L.M. Caspers, Rad. Eff. **78** (1983) 105.
36. J.H. Evans, A. van Veen, and L.M. Caspers, Scripta Met. **15** (1981) 323.
37. J.H. Evans, A. van Veen and L.M. Caspers, J. Nucl. Mater. **103&104** (1981) 1181.
38. G.W. Greenwood, A.J.E. Foreman, and D.E. Rimmer, J. Nucl. Mater. **1** (1959) 305.
39. L.M. Caspers and A. van Veen, phys. stat. sol. (a) **68** (1981) 339.
40. J.K. Noerskov, Phys. Rev. B **26** (1982) 2875.
41. M.S. Daw and M.I. Baskes, Phys. Rev. B **29** (1984) 6443.
42. P. Nordlander, J.K. Noerskov and F. Besenbacher, J. Phys. F **16** (1986) 1161.
43. A.R. Miedema, F.R. de Boer and R. Boom, Calphad **1** (1977) 341.
44. Calculated by using the Finnis-Sinclair potential. M.W. Finnis and J.E. Sinclair, Philos. Mag. A **50** (1984) 45.
45. A. van Veen and L.M. Caspers, Solid State Comm. **30** (1979) 761.
46. J. H. Evans and B.L. Eyre, Acta Met. **17** (1969) 1109.
47. A. van Veen, J.H. Evans, W.Th.M. Buters and L.M. Caspers, Rad. Eff. **78** (1983) 53-66.
48. A. van Veen, Materials Science Forum **15-18** (1987) 348.
49. Proc. of the Third Topical Meeting on Fusion Reactor Materials, eds. J.B. Whitley, K.L. Wilson, F.W. Clinard Jr. (North-Holland, Amsterdam, 1984).
50. E.V. Kornelsen, Rad. Eff. **13** (1972) 227.
51. See e.g. A. van Veen, Materials Science Forum **15-18** (1987) 3.
52. L.M. Caspers and A. van Veen, Phys. Stat. Sol. (a) **68** (1981) 339.
53. A. van Veen, J.H. Evans, W.Th.M. Buters and L.M. Caspers, Rad. Eff. **78** (1983) 53.
54. G.J. van der Kolk, A. van Veen, J.Th.M. de Hosson, L.M. Caspers, Nucl. Instr. and Meth. B **6** (1985) 517.
55. W.Th.M. Buters and A. van den Beukel, J. Nucl. Mater. **137** (1985) 57.

Chapter 2
Experimental details

2.1 Introduction

In this chapter, a description is given of the apparatus which has been utilized to conduct the experiments discussed in the next chapters. In addition, two desorption spectrometers are presented which have newly been developed for (1) research on ion irradiation induced desorption from surfaces and (2) hydrogen isotope permeation experiments.

Firstly, it is described in section 2.2 how samples of fusion reactor materials have been prepared for investigation. Then, in section 2.3, it is explained how defects have been introduced in the samples, and how the defects were modified in order to obtain the most appropriate defect structure for investigation. It is also demonstrated how the gas desorption technique introduced in section 1.3 has been put into practice. In section 2.4 it is explained and examplified how the dissociation of defects is reflected in gas desorption spectra. Section 2.5 is allotted to the positron annihilation technique, which has been used in several investigations to supplement the information obtained by thermal gas desorption spectrometry.

If atoms or molecules are adsorbed on surfaces, they can not only desorb thermally, but also due to energy transfer from impinging particles. If the impinging particles are ions, the latter process is called ion irradiation induced desorption or ion impact desorption. The process is related to sputtering (the erosion of solid surfaces by ion bombardment), and in fusion reactors the substantial amounts of gaseous species that are thus released by the high fluxes of energetic particles might contaminate the plasma. Since data on ion irradiation induced desorption are scarce, a special desorption spectrometer has been developed for this purpose, which is presented in section 2.6.

Section 2.7, finally, describes the construction of a new spectrometer for hydrogen isotope permeation experiments. Hydrogen isotope permeation in fusion reactor materials is of paramount importance for the hydrogen isotope inventory in the plasma[1]. It successively encompasses: adsorption of a hydrogen molecule at the surface of a construction material, dissociation of the molecule into atoms, solution of the atoms, diffusion of the atoms, trapping and detrapping of the atoms, recombination of the atoms into molecules at a surface site, and desorption of the molecule. In the past, permeation models have been published by Pick en Sonnenberg[2], Waelbroeck *et al.*[3], Doyle[4], and Arbab and Hudson[5]. In most of these models a distinction is made between permeation limited by diffusion and permeation limited by surface recombination. Models including trapping and detrapping at

defects have been described by *e.g.* Brice and Doyle[6], Tanabe *et al.*[7], and Myers and Wampler[8]. In all the models however there is a lack of data on permeation processes in the presence of traps, and there is also a lack of data on surface recombination rates. To supply the required data, the new spectrometer described in section 2.7 has been designed.

2.2 Specimen preparation

Taking into account the selection considerations of section 1.1.3, most experiments described in the following have been carried out on molybdenum and tungsten. The samples on which the gas desorption experiments have been performed were, unless otherwise stated, single crystalline high purity (99.999%) metal discs of 8 mm diameter and 3 mm thickness. Only single crystalline material was used to avoid any influence of grain boundaries on the measurements.

Before being mounted in a UHV (ultra high vacuum) chamber, the samples were mechanically polished with diamond powder (grain size 0.25 μm) and electrochemically polished in a 25%H_2SO_4-75% methanol solution.

After being mounted in the UHV chamber, the Mo and W samples were cleaned by repeated heating to 2200 K and exposure for 1 h to 10^{-4} Pa H_2 gas at 1600 K. Before every measurement, the samples were heated up to 2/3 of the melting temperature to remove all remaining defects.

Several samples have been prepared for investigation by TEM (transmission electron microscopy). These samples were discs of 3 mm diameter and 20-40 μm thickness. After irradiation, the samples were back-thinned to produce transparent regions for electrons at the implanted area[9].

In chapter 6 experiments are described on polycrystalline stainless steel L316 with grain sizes varying from 80-100 μm. This stainless steel was obtained from the European fusion team in Ispra, Italy (charge 12247), and serves as a reference steel for the international fusion materials research. The composition is as follows: Cr (17.62%), Ni(12.34), Mo(2.31), Mn(1.84), Si(.45), Cu(.20), Co(.17), N(.06), P(.03), C(.02), Ta(.01), S(.001), B(8-15 ppm). The carbon content is low to guarantee easy manufacturing. The stainless steel samples were mechanically polished until the surface roughness was within 50 nm. The samples were not electrolytically polished, since electrolytical polishing of multicomponent materials results in preferential etching and hence may increase the surface roughness.

2.3 Controlled defect production and modification

To introduce defects and gas atoms in the samples and to modify and monitor the defects, use was made of the gas desorption spectrometers TDS

I, TDS II, TDS III, TDS IV and HDD which were available at the Radiation Damage group in Delft[10,11,12]. The principle of the first four spectrometers is the same and is shown schematically in fig. 2.1.

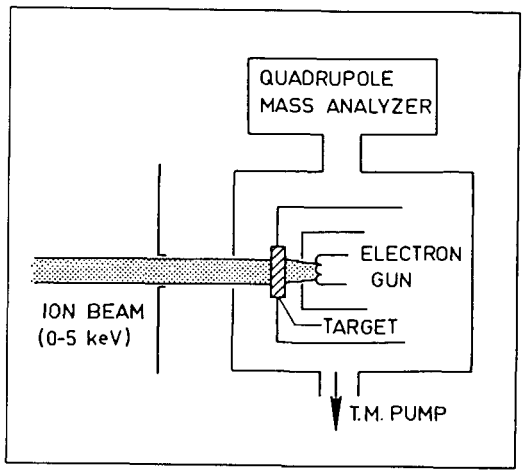

Fig. 2.1. Basic configuration of a thermal gas desorption spectrometer. Source: A. Van Veen and L.M. Caspers[10].

The samples, mounted in a UHV chamber, were irradiated with gas ions from a low pressure (10^{-6} Pa) ion gun, which allowed ion acceleration to energies ranging from 25 eV to 5 keV. The purity of the used gas was 99.995-99.999 vol.%. To exclude neutrals, the ion beam could be deflected by means of two parallel electrodes. To obtain a homogeneous distribution of the ions over the sample surface, the ion beam could be swept vertically and horizontally with the help of two other sets of electrodes. To define the irradiated area of the sample, a diaphragm was positioned in front of the sample surface. In the experiments of section 3.2 and chapter 4 the irradiated area was 0.05 cm^2, in the experiments of section 3.3 and chapter 6 the irradiated area was 0.28 cm^2. The obtained irradiation flux densities could mount to $5x10^{12}$ ions cm^{-2} s^{-1}.

To select particles on mass and charge, use was made of an $\vec{E}x\vec{B}$ filter. The resolution obtained with this so-called Wienfilter is shown in fig. 2.2, where it can be seen that He^+, N^+ and N_2^+ ions can sufficiently be separated from impurity gas ions. Fig. 2.2 also shows the hysteresis of the filter which is due to remanent magnetism in the core of the electromagnet.

To modify or anneal the defect structure, the samples could be heated by 2.5 keV electron bombardment on the rear side. The temperature was measured by a WRe3%-WRe25% thermocouple, and a computer controlled feedback system[13] assured a linear temperature increase with time. Unless

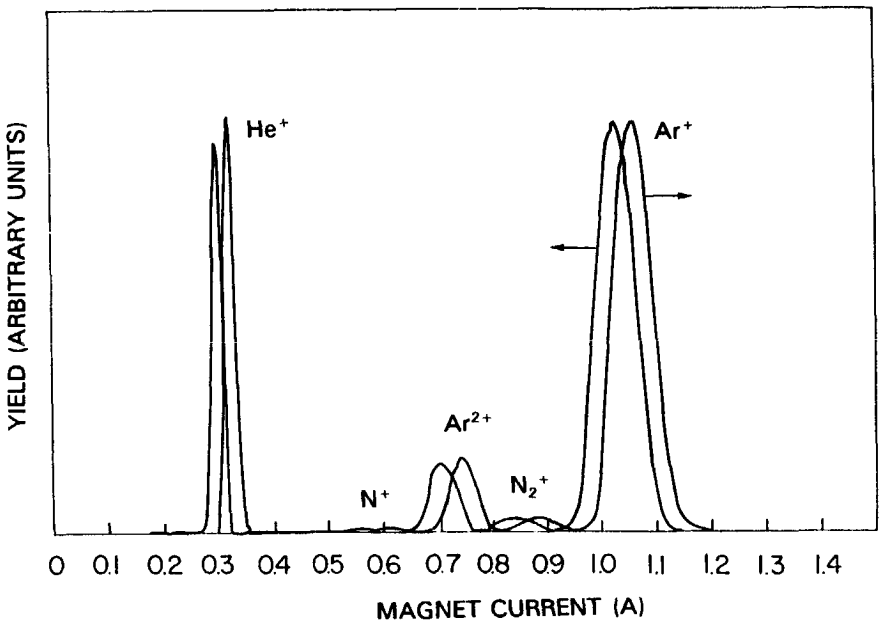

Fig. 2.2. Seperation between helium, argon and nitrogen ions obtained with the Wien filter. The spectrum has been recorded by initially increasing (arrow to the right) and then decreasing (arrow to the left) the current of the Wien filter magnet. Hysteresis is clearly perceptible. The electric field was 6×10^3 V/m.

otherwise stated, all gas release temperatures quoted herafter correspond to a heating rate of 40 K/s. Only in the experiments on silicon described in section 4.4 the heating rate was 10 K/s because of the low heat conductivity of silicon.

The release of trapped gas from the samples during heating was monitored by a quadrupole mass spectrometer (Balzers QMG 111 in the experiments of chapter 3 and 4, and Balzers QMG 311 in the experiments of chapter 6). During the desorption the gas was pumped away, and the relation between the helium desdorption rate L(t) and the measured partial helium pressure P(t) during desorption is given by[3]

$$L(t) = V\left(\frac{dP}{dt} + \frac{P}{\tau}\right) \qquad (2.1)$$

where $\tau = V/S$ with V the desorption volume (about 1.5 l, varying on the apparatus) and S the gas pumping speed. τ was determined by measuring the exponential decrease of a gas pulse.

Calibration of the mass spectrometer was done after each measurement by introducing a well-defined amount of gas atoms in the system and measuring the response of the mass spectrometer. This well-defined amount was determined by inserting gas in a fixed volume (about 1 cm^3, depending on the apparatus used) and measuring its pressure with a membrane manometer. The sensitivity for argon *e.g.* was $\sim 5 \times 10^{-6}$ detected argon ion per desorbed argon atom at an average residence time τ in the UHV chamber of 1.5 s, and for helium $\sim 1 \times 10^{-6}$ detected helium ion per desorbed ion at an average residence time τ of 0.5 s.

For irradiation doses above 10^{16} cm^{-2} use was made of a high dose desorption spectrometer named HDD, which allowed a higher irradiation flux density. In this apparatus a magnetically constricted plasma was created by impact ionisation of 6×10^{-3} Pa gas atoms. The samples were negatively biased with respect to the plasma. This resulted in a much higher irradiation flux density than in the previously mentioned desorption spectrometers, *i.e.* $\sim 3 \times 10^{15}$ cm^{-2} s^{-1}. The area of the sample which is exposed to irradiation is in this spectrometer not defined by a diaphragm, but by the surface of the sample. The high dose desorption spectrometer has been used in the experiments described in section 3.4 and chapter 5.

2.4 Defect dissociation

In thermal gas desorption experiments, the defects usually dissociate due to thermal annealing. The dissociation will start at a temperature that corresponds to the dissociation energy of the most weakly bound constituant.

To illustrate this, fig. 2.3 shows a thermal gas desorption spectrum obtained after irradiating a Mo(110) sample with 1 keV helium ions. The broad peak between the temperatures of 300 K and 650 K is due to the release of helium trapped near the sample surface[14]. The peaks labelled E, F, G and H have been shown previously[14] to represent the amount of helium released from respectively $He_{6\text{-}9}V$ (a complex of n helium atoms in a vacancy, with $5 \leq n \leq 9$), $He_{3\text{-}4}V$, He_2V and HeV defects. It is important to note that the release of helium from defects containing more than one helium atom occurs in several steps[14]. A vacancy containing two helium atoms for instance will release one helium atom at a temperature of ~ 970 K (which will contribute to the peak labelled G), thus leaving a HeV defect behind. When the temperature is further increased, the He atom from the remaining HeV defect will contribute to the peak labelled H. Consequently, the number of vacancies can be derived from the helium population of the H peak. The experiment also shows that a Mo sample containing only HeV's and no multiply filled vacancies can simply be obtained by irradiating a sample with helium ions and then annealing it to 1040 K.

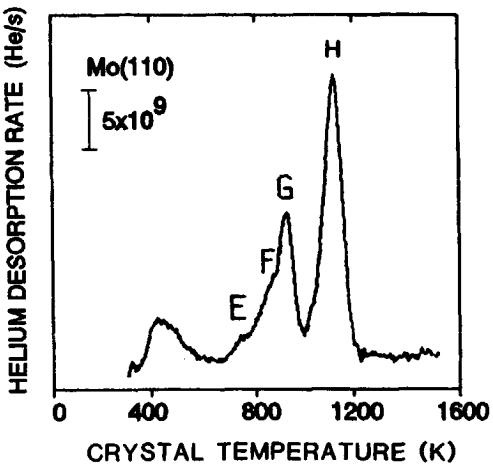

Fig. 2.3. A helium desorption spectrum obtained after irradiating a Mo(110) single crystal with 1 keV He^+ ions in a dose of $1.0x10^{13}$ cm^{-2}. No modification or decoration of the formed defects has taken place. The spectrum shows the helium desorption behaviour during the final anneal step (40 K/s).

Trapped gas atoms can not only reach the sample surface after dissociation of the defect, but also due to diffusion of the defect (possibly assisted by thermally generated vacancies). The temperature at which these processes take place depends on the annealing method. Three methods are commonly applied:

1) Isothermal annealing, where the temperature is kept constant.
2) Isochronal annealing, where the temperature is increased in steps, and after every step the temperature is kept at a constant value for a fixed period of time. Measurements are usually performed at room temperature before every increase.
3) Ramp annealing, where the temperature is increased linearly in time.

Method 2 has been applied in the positron annihilation and TEM measurements described here, method 3 in the gas desorption experiments. When first order desorption processes are investigated, it is possible to calculate corresponding temperatures for the three annealing methods[15]. A first order desorption process is described by:

$$\frac{dN_D}{dt} = -N_D \nu \exp\frac{-E^D}{kT(t)} \qquad (2.2)$$

where N_D is the number of defects in the sample. For ramp annealing, dT/dt is a constant ß, and the temperature at which most dissociation processes

take place is given by:

$$\exp\frac{-E^D}{kT_m}=\beta E^D/(vkT_m^2). \qquad (2.3)$$

This can be derived from $d^2N_D/dT^2=0$. The fraction of defects not having dissociated at T_m equals ~0.4. In the case of isochronal annealing, the temperature T_c at which the same degree of recovery is achieved is derived from:

$$\frac{N_D(t)}{N_D(0)}=\exp(-t\,v\,e^{-E^D/kT_c})\approx 0.4, \qquad (2.4)$$

where $N_D(0)$ denotes the number of defects at t = 0 s. Thus, for a given value of T_m equation 2.3 can be used to calculate E^D and this value substituted in equation 2.4 yields T_c.

2.5 Positron Annihilation

To supplement the information obtained by gas desorption spectrometry, use has been made of the positron lifetime technique. This technique, which is based on the fact that the lifetime of a positron in a material depends on the defect structure in the material, has extensively been described elsewhere[16]. Briefly, the experimental set-up is described as follows[17].

A positron source (in the present experiments ^{22}NaCl-on-mylar) is sandwiched between two samples that have undergone identical treatment. The sandwich is surrounded by two gamma detectors (consisting of a scintillator coupled to a photomultiplier), one to detect the 1275 keV photon which is emitted simultaneously with a positron from the ^{22}Na source, and one to detect a 511 keV photon which is emitted when the positron is annihilated in one of the samples. The time difference between the detection of the 1275 keV and the 511 keV photon is the positron lifetime, and is measured by a time to amplitude convertor coupled to a multichannel analyser. To single out the required energies of 1275 and 511 keV, single channel analysers are employed.

The resolution of the spectrometers used in the experiments of chapters 4 and 5 is respectively 250 and 200 ps. The obtained data was, unless otherwise stated, analysed by assuming a two state trapping model[18]. In this model two positron lifetimes are distinguished, *i.e.* one corresponding to free delocalized positrons in bulk material and one corresponding to localized positrons trapped in defects.

2.6 A spectrometer for ion irradiation induced desorption

To gain more insight into the process of ion irradiation induced desorption, a new spectrometer has been constructed, which is shown in fig. 2.4. The main components are:

- a rotatable tiltable sample which can be heated by electron bombardment on the rear side;
- a 1/4" tube from which gas atoms or molecules emerge to cover the sample surface with an adsorbed layer;
- a mass analysed ion source as described in section 2.3 to bombard the sample with ions;
- a computer controlled translatable quadrupole mass spectrometer (Balzers

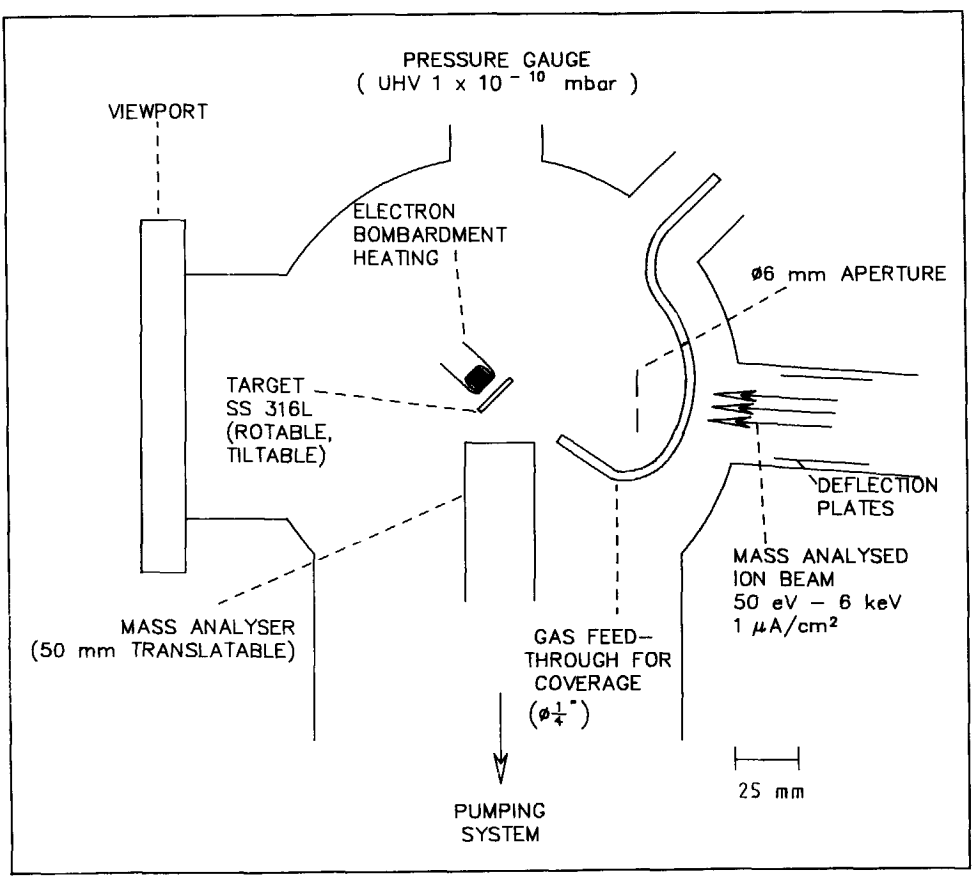

Fig. 2.4. Schematic top view of the desorption spectrometer for ion irradiation induced desorption.

QMG 311) to monitor the species coming off the sample during ion bombardment;
- a 6 mm diaphragm mounted 60 mm from the target surface to define the irradiated area.

Special CAMAC software has been developed to control the mass spectrometer in such a way that it can monitor the evolution in time of four pre-selected masses simultaneously.

The mass spectrometer can be used in two modes: (1) the usual mode with its filament switched on to monitor neutral particles, and (2) a mode with its filament switched off to monitor secondary ions coming off the sample surface. In the former mode, the neutral particles are ionized in the ion source of the mass spectrometer before being mass analysed. In the latter mode the monitored particles are already ions, and all the grids and lenses in the ionisation part of the mass spectrometer are at earth potential. The sample is at earth potential in both modes.

The sample heating is computer controlled, so that not only ion impact desorption can be monitored, but also thermal desorption. The UHV background pressure is 1×10^{-8} Pa. The performance of the spectrometer is reviewed in section 6.4.

2.7 A desorption spectrometer for hydrogen permeation experiments

The new desorption spectrometer for permeation experiments comprises a rotatable cylindrical miniature UHV chamber incorporated in a larger UHV chamber. The two independently pumped vacuum chambers are separated from each other by a membrane. This circular membrane (diameter 12 mm, thickness 30 μm) is electron welded on a small cylinder which terminates one of the extremities of the miniature UHV chamber. The membrane serves as the sample through which the hydrogen isotope flux permeates and is made out of a potential fusion reactor material. Stainless steel, molybdenum, nickel, and nickel alloys are the first candidates for the membrane, which also enable comparison with previously published results[19,20,21,22].

The cylindrical miniature UHV chamber is 140 mm long and envelopes a very compact integrated ion accelerator, designed by A. van Veen and fabricated by J.G.J. van Oort. This Lilliputian ion accelerator, portrayed in figs. 2.5 and 2.6, allows keV irradiation of the membrane with hydrogen isotopes. The back of the miniature UHV chamber accommodates a 32 mm flange which can be detached to replace the filament of the ion source. At the exterior of the miniature UHV chamber, a filament is coiled around the membrane for electron impact heating.

Due to 1.5 m long spirally suspended vacuum bellows, the miniature UHV chamber can be swivelled around in the large UHV chamber in such a way

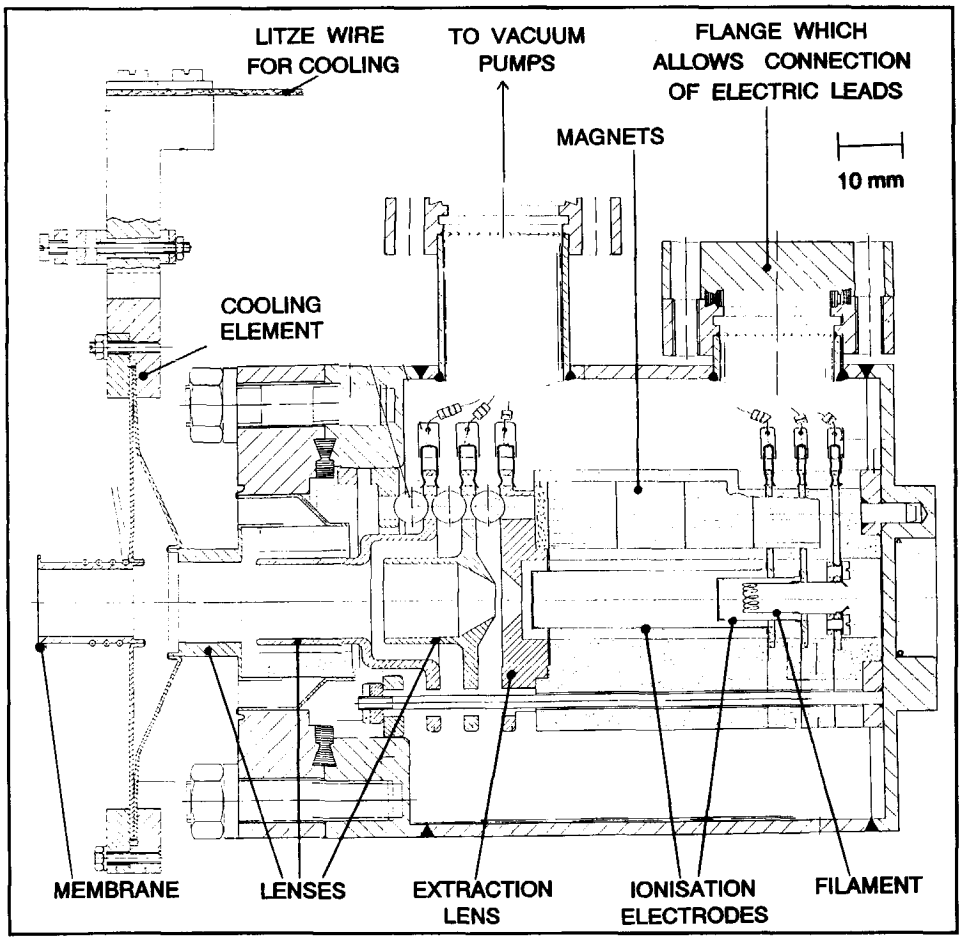

Fig. 2.5. Design of the miniature ion accelerator.

that the membrane optionally faces (see figure 2.7):

- a differentially pumped 5 keV ion accelerator similar to the one described in section 2.3 (this accelerator can be used to create defects in the membrane or to modify the membrane surface),
- a 30 keV Danfysik 911A[23] ion accelerator (which serves the same purpose as the 5 keV accelerator),
- a quadrupole mass analyser (Balzers QMG 311, for gas desorption experiments),
- a neodymium laser (for defect production and flash annealing),
- a Riber OPC105 cylindrical mirror analyser (to perform Auger electron spectroscopy; stabilised high voltage supplies were manufactured by J. de Roode and appropriate CAMAC software was newly developed),

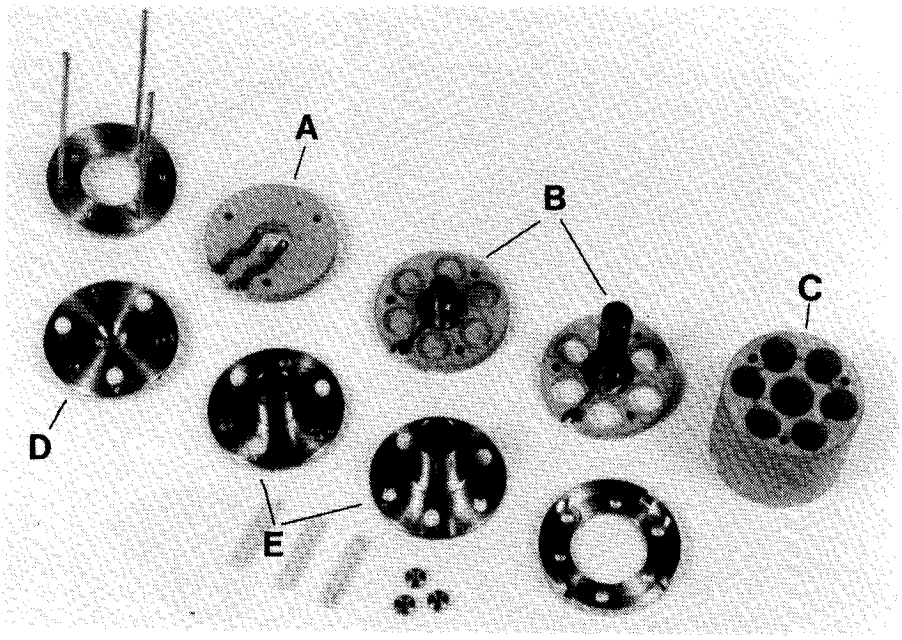

Fig. 2.6. Components of the miniature ion accelerator. (A) filament holder, (B) ionisation electrodes (C) holder for permanent magnets (which enhance the ionisation yield), (D) extraction lens, (E) acceleration lenses.

- a Kelvin probe[24] (this is an extremely sensitive vibrating electrode in front of the sample surface with which adsorbed layers can be monitored; this is done by measuring changes in work function caused by the adsorbed layer).

It should be emphasized that the facilities for surface characterisation are indispensible for well-defined permeation experiments. Surface impurities *e.g.* may exert an inhibitory influence on dissociation and recombination processes[25], as has been pointed out by *e.g.* Pick[26], Wampler[27] and Richards *et al.*[28] (note though that surface barriers can only influence the rate at which equilibrium is reached but not the final stationary state). The heat of adsorption is known to be dependent on the surface concentration and topography of the adsorbed particles (due to repulsive forces) and also on inhomogeneities in the surface (steps *e.g.*).

A problem with hydrogen desorption experiments is the inevitable presence of a relatively high hydrogen background in the vacuum system. This problem can partly be circumvented by performing experiments with deuterium instead of hydrogen. For a clear separation between surface signal and background signal however, a piezoelectrically driven chopper and a collimator have been mounted in front of the quadrupole mass analyser. The measured signal thus

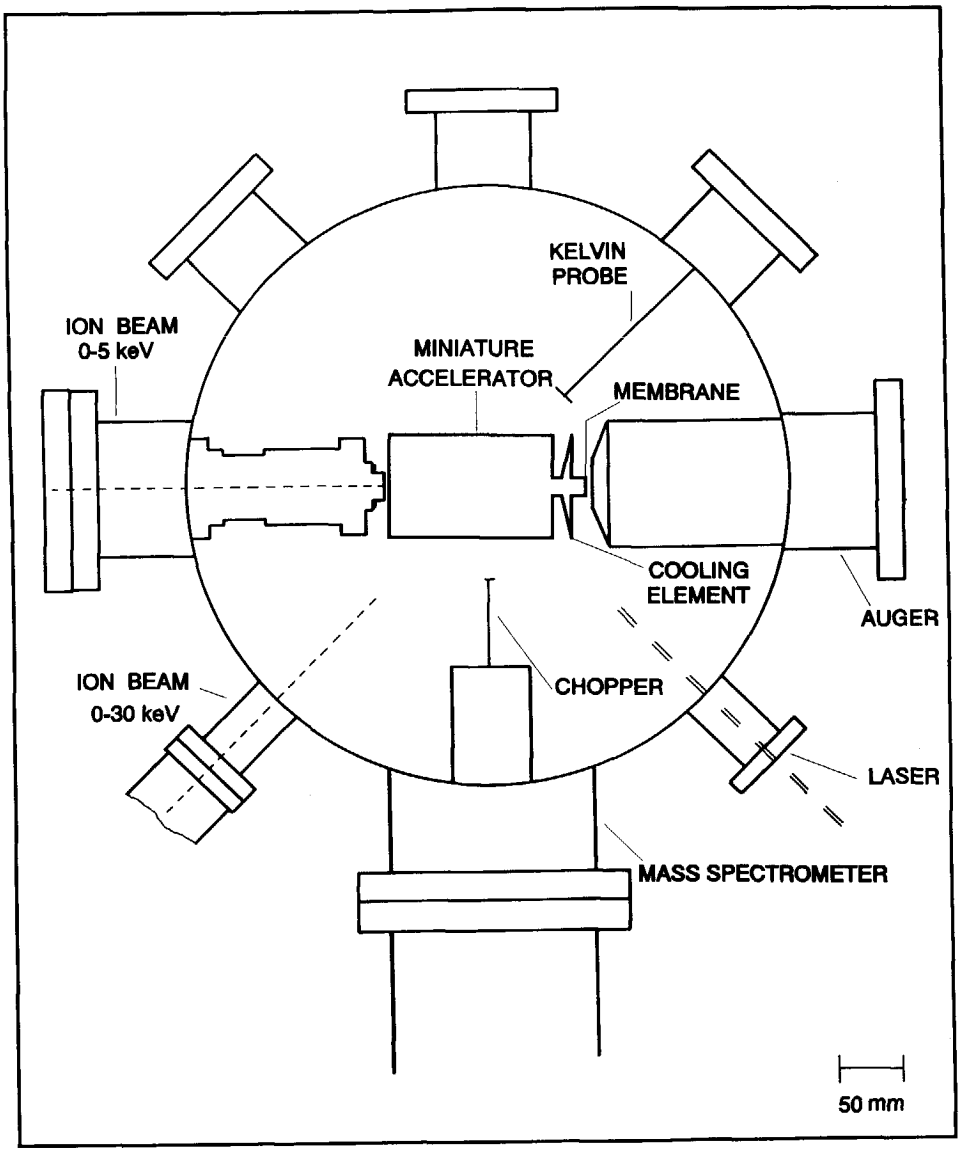

Fig. 2.7. Schematic top view of the UHV chamber for hydrogen permeation experiments. The miniature ion accelerator with the permeation membrane is positioned in the centre and can be swivelled along the indicated paraphernalia.

equals $m(t)s(t) + n(t)$ convoluted with $h(t)$, where $m(t)$ denotes the chopper modulation, $s(t)$ the surface signal, $n(t)$ the background signal, and $h(t)$ the response of the mass analyser. The chopping frequency should be chosen low enough to avoid renewed mixing of surface and background signals due to the

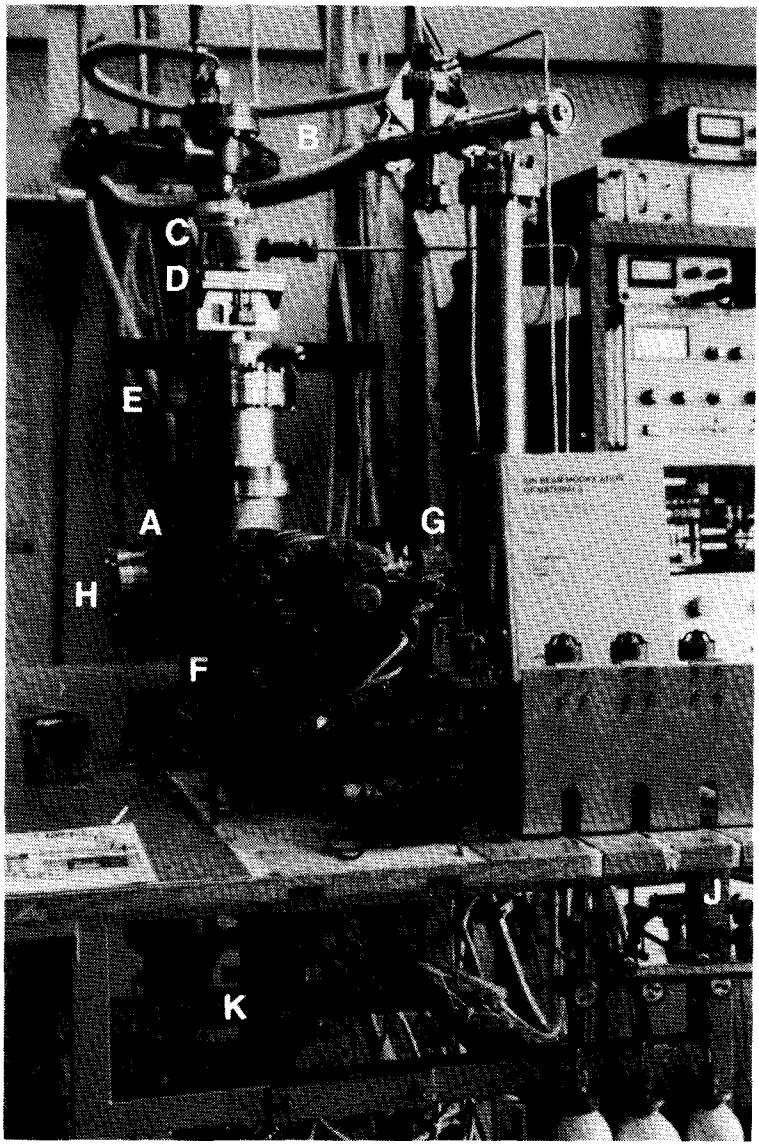

Fig. 2.8. Testing apparatus for miniature ion source. (A) UHV vessel in which the miniature UHV system is incorporated, (B) vacuum bellows for gas inlet and pumping of the miniature UHV system, allowing rotation over 270 degrees, (C) differentially pumped gas feedthrough enabling rotary motion of the miniature UHV system, (D) tilting device, (E) liquid nitrogen receptacle for cooling of the membrane holder via a 35 mm thick copper ribbon, (F) quadrupole mass spectrometer, (G) ion source, (H) viewport, (J) gas inlet system, (K) pumping systems. The components (C), (D) and (E) are shown in detail in fig. 2.9.

finite residence time of the hydrogen in the quadrupole mass analyser. A computer simulation has been developed which allows determination of the ratio between surface signal and background signal for various collimators and various geometries. Hither to, the desorption spectrometer has been developed to such an extent that all components have been fabricated, assembled, and tested, apart from the Kelvin probe. In a specially prepared separate UHV chamber, shown in fig. 2.8, the testing of the miniature ion source is under way.

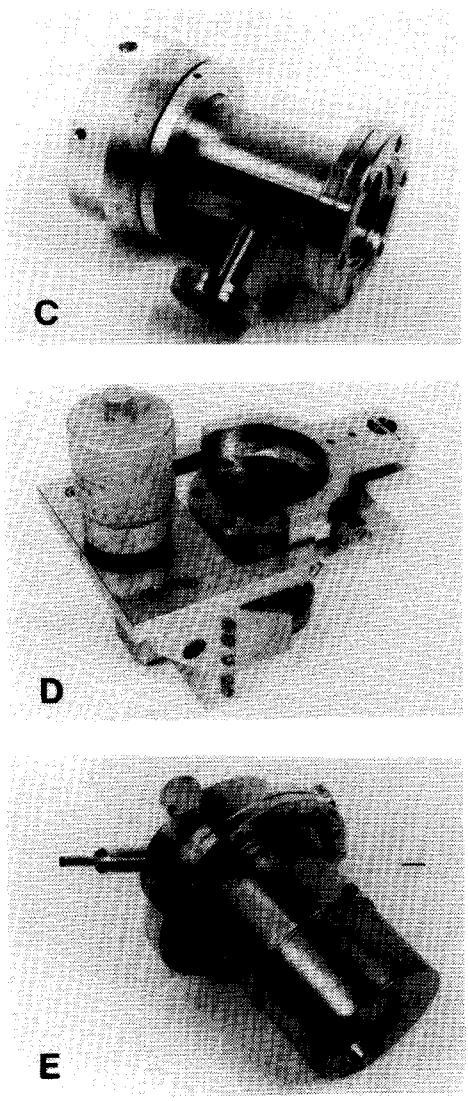

Fig. 2.9. The components C, D and E of figure 2.8 shown in detail.

References chapter 2

1. M. Kitajima, Corrosion Engineering **36** (1987) 241.
2. M.A. Pick and K. Sonnenberg, J. Nucl. Mater. **131** (1985) 208.
3. F. Waelbroeck, P. Wienhold and J. Winter, J. Nucl. Mater. **111&112** (1982) 185.
4. B.L. Doyle, J. Nucl. Mater. **111&112** (1982) 628.
5. M. Arbab and J.B. Hudson, Appl. Surf. Sci. **29** (1987) 1.
6. D.K. Brice and B.L. Doyle, J. Nucl. Mater. **103&104** (1981) 503.
7. T. Tanabe, N. Saito, Y. Etoh and S. Imoto, J. Nucl. Mater. **103&104** (1981) 483.
8. S.M. Myers and W.R. Wampler, J. Nucl. Mater. **111&112** (1982) 579.
9. J.H. Evans, A. van Veen and L.M. Caspers, Rad. Eff. **78** (1983) 105.
10. A. van Veen and L.M. Caspers, in: Proc. Consultants Symp. on Inert Gases in Metals (AERE Report 9733, Harwell, 1980) p. 494.
11. A. van Veen and L.M. Caspers, Solid State Comm. **30** (1979) 761.
12. L.M. Caspers and A. van Veen, Phys. Stat. Sol. A **68** (1981) 339.
13. G.J. van der Kolk, Ph.D. Dissertation, Delft University of Technology, 1984.
14. A. van Veen, J.H. Evans, W.Th.M. Buters and L.M. Caspers, Rad. Eff. **78** (1983) 53.
15. A. van Veen, A. Warnaar and L.M. Caspers, Vacuum **30** (1980) 109.
16. See e.g. Positrons in Solids, Topics in Current Phys. **12**, ed. P. Hautojärvi (Springer, Heidelberg, 1979).
17. J. de Vries, Ph.D. Dissertation, Delft University of Technology, 1987.
18. A. Seeger, Appl. Phys. **4** (1974) 183.
19. K.L. Wilson, J. Nucl. Mater. **103&104** (1981) 453.
20. T. Tanabe, N. Saito, Y. Etoh and S. Imoto, J. Nucl. Mater. **103&104** (1981) 483.
21. A.S. Schmidt, F. Verfuss and E. Wicke, J. Nucl. Mater. **131** (1985) 247.
22. B.M.U. Scherzer, P. Boergesen, W. Möller, Nucl. Instr. and Meth. B (1986) 375.
23. G. Sidenius, Proc. Int. Conf. on Electromagnetic Isotope Separators, Marburg, Germany, 1970, p. 423.
24. I.D. Baikie, K.O. van der Werf, H. Oerbekke, J. Broeze and A. van Silfhout, Rev. Sci. Instrum. **60** (5) (1989) 930.
25. M. Braun, B. Emmoth, F. Waelbroeck and P. Wienhold, J. Nucl. Mater. **93&94** (1980) 861.
26. M.A. Pick, J. Nucl. Mater. **145-147** (1987) 297.
27. W.R. Wampler, J. Nucl. Mater. **145-147** (1987) 313.
28. P.M. Richards, S.M. Myers, W.R. Wampler and D.M. Follstaedt, J. Appl. Phys. **65**(1) (1989) 180.

Chapter 3
The interaction between self-interstitials and argon in molybdenum

3.1 Introduction

The interaction of mobile self-interstitial atoms with other defects in fusion reactor materials is of crucial importance for the nucleation and evolution of damage. In studies aimed at understanding this interaction, the required self-interstitials are usually produced by MeV electron irradiation[1,2]. This method has the disadvantage that copious amounts of unwanted vacancies are produced concurrently. Moreover, the temperature should be such that the vacancies remain immobile, which restricts thermal annealing experiments severely.

For these reasons, Van Veen *et al.*[3,4,5] have introduced a novel technique, which enables the creation of self-interstitials without interfering vacancies. TEM-experiments carried out by Ogilvie *et al.*[6], Bowden and Brandon[7], and Venables and Baluffi[8,9] had already indicated that it is possible to create self-interstitials without interfering vacancies by low energy heavy ion bombardment. Later, these findings were corroborated by Bullough *et al.*[10], who bombarded copper and molybdenum crystals with low energy self-ions and used TEM to monitor the resultant self-interstitial structures. By employing the THDS technique, Van Veen *et al.*[3,4,5] have been able to study the effects of low energy heavy ion bombardment on a much smaller scale than visible by TEM. They elucidated that, during low energy heavy ion bombardment,

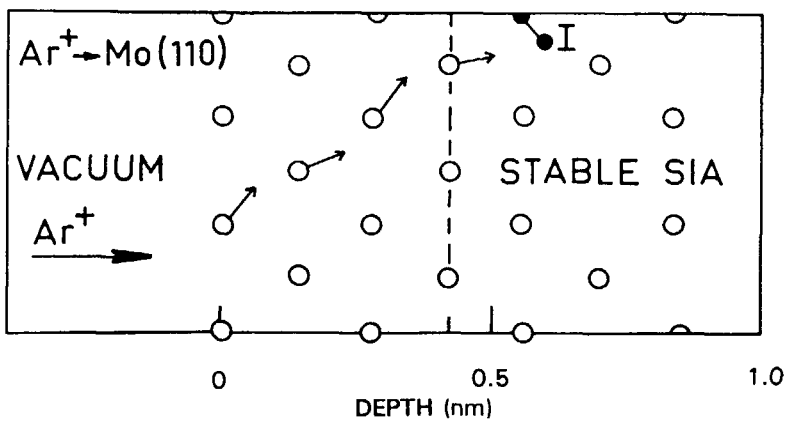

Fig. 3.1. The production of a self-interstitial atom under the surface of a bcc (110) crystal via a replacement collision sequence in the <111> direction.

vacancies are created in the very surface of the material, and that due to replacement collision sequences self-interstitials are generated at larger depths[11,12]. This process, which is depicted in fig. 3.1, ensures that spontaneous recombination between self-interstitials and concurrently produced vacancies does not occur. The low bombardment energy guarantees that the heavy ions do not penetrate deep into the sample: they are either reflected or they remain in surface layers.

In section 3.2 the novel technique is examined more closely, and special attention is paid to the role of replacement collision sequences and the threshold energy for the generation of self-interstitials. In section 3.3 the novel technique is applied. It is demonstrated that the accumulation of self-interstitials produced by particle irradiation can give rise to the formation of dislocation loops in fusion reactor materials, and that this may lead to a considerable increase in the retention of gas atoms. The interaction between self-interstitials and argon atoms in high fluence irradiated molybdenum is discussed, and in order to gain more insight into processes governing gas atom retention, a comparison is made with silicon in section 3.4.

3.2 The production of self-interstitial atoms

3.2.1 Experimental results

In order to gain more insight into the novel self-interstitial production process, the following measurement cycle has been conceived:

1) Creation of HeV defects (vacancies filled with helium) in a Mo(110) crystal; this was realized by 3 keV helium ion bombardment perpendicular to the surface, followed by partial annealing to 1040 K (see section 2.4).
2) Bombardment of the samples with low energy argon ions to generate self-interstitial atoms.
3) Monitoring of the helium release during thermal annealing.
4) Determination of the number of HeV's in order to see whether part of them were annihilated by the reaction HeV + I → He (in section 1.2.3 it has already been argued that this reaction is exothermal).

The whole procedure has been repeated for each measurement, since all defects are annihilated or removed by the annealing in the last stage.

Fig. 3.2 shows the helium desorption spectra taken from the Mo sample for various argon ion energies. It can be noticed that with increasing argon ion energy the H peak population reduces and that simultaneously F and G peaks emerge. In fig. 3.3 it is shown how variation of the 50 eV argon dose affects the populations of the helium release peaks H and G in an identical experiment on Ni(110). The population of the H peak, which equals the number of HeV defects, is seen to decrease exponentially with heavy ion dose in accordance

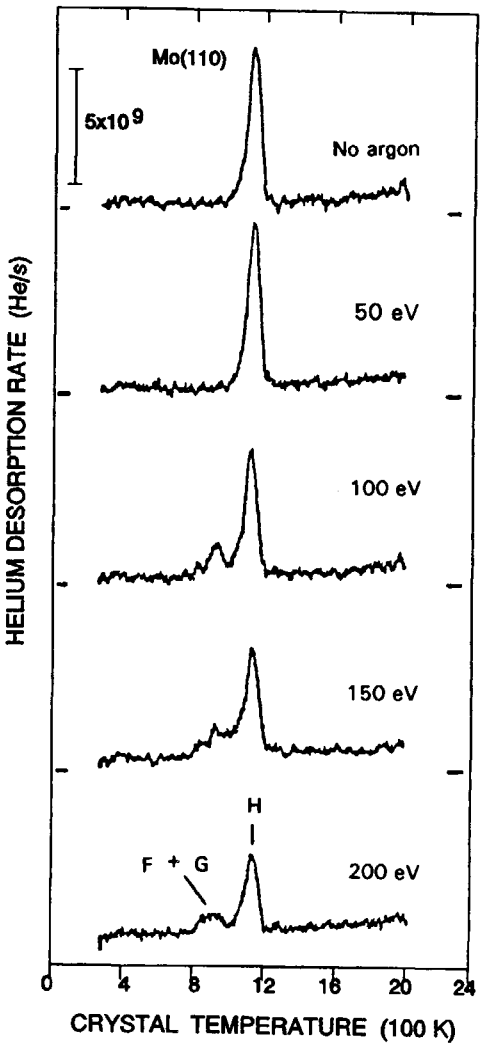

Fig. 3.2. Helium desorption spectra obtained after successively irradiating a Mo(110) single crystal with 1.5×10^{12} cm^{-2} 3 keV He ions, annealing up to 1040 K, and bombarding it with 5×10^{14} cm^{-2} argon ions. The argon ion energy varied as indicated.

with the recombination reaction HeV + I → He. The population of the G peak, which represents the He_2V concentration, initially equals zero but increases with increasing heavy ion dose and reaches a maximum at a dose of ~6×10^{14} Ar cm^{-2}. Apparently, the helium which is released in the reaction HeV + I → He is partly retrapped by other HeV's, thus contributing to the formation of vacancies that are multiply filled with helium.

Beyond a certain filling degree the defects cannot be annihilated by self-interstitials any longer[13]. Therefore, a deviation from the exponential behaviour is envisaged at high argon doses. This deviation will also occur because at high argon doses the subsurface damage will be such that the production of self-interstitials becomes less efficient.

At the bombardment doses where the annihilation of the HeV defects proceeds exponentially, it is possible to define a self-interstitial capture coefficient μ:

$$\mu = - (1/N_{HeV})\, dN_{HeV}/dP \qquad (3.1)$$

where N_{HeV} denotes the number of HeV defects per cm^2 and P the dose of heavy ions per cm^2. Fig. 3.4 shows the value of μ for the molybdenum experiment as a function of the argon ion energy. It can be seen that μ is of the order of 10^{-15} cm^2 per ion. It can also be observed that a rather well defined threshold energy of (80 ± 5) eV exists for the creation of self-interstitial atoms by heavy ions.

To prove that in the above experiments the HeV defects are indeed completely removed after the argon bombardment, experiments have been carried out in which the crystal was refilled with 100 eV helium after the argon bombardment. The results of these experiments, which are not shown here, confirmed that not only the helium had been released from the HeV defects, but that the accompanying vacancies had been annihilated as well.

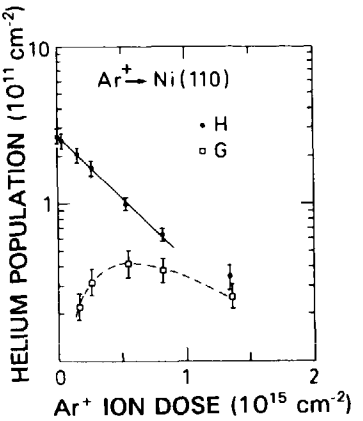

Fig. 3.3. Helium population of the peaks G and H versus argon dose in an experiment on Ni(110) analogous to that of fig. 3.2. The argon energy was 50 eV.

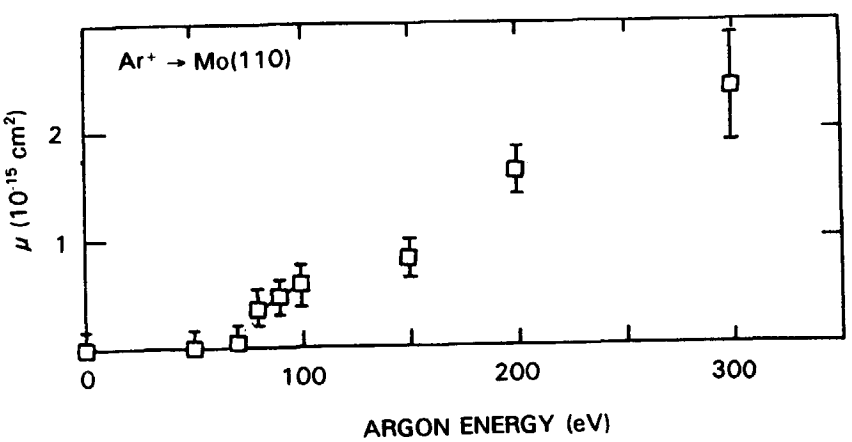

Fig. 3.4. The self-interstitial capture coefficient μ versus argon ion energy, derived from the reduction in the H peak population in fig. 3.2.

3.2.2 Discussion

From the experimental results it is clear that, due to the low energy heavy ion bombardment, self-interstitial atoms are generated which are able to annihilate the HeV defects. Sputtering processes are not expected to play an important role in the elimination of the HeV defects, because 10^{15} cm^{-2} heavy ions with energies of a few hundred eV do not remove more than one atomic layer (the depth distribution of the vacancies is shown in fig. 3.5).

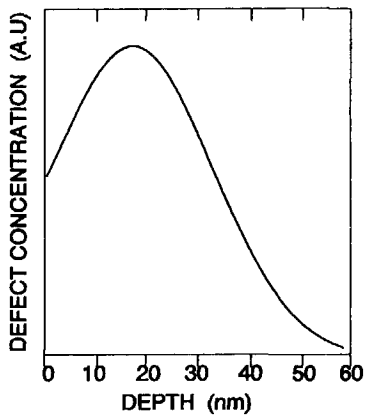

Fig. 3.5. Depth distribution of vacancies in molybdenum after 3 keV helium ion bombardment, calculated with MARLOWE and approximated by a Gaussian. The mean depth is 22 nm.

The effectiveness of the self-interstitial generation process depends on the depth under the surface at which the self-interstitials are produced by the replacement collision sequences. If they are produced too close to the surface or if they come too close to the surface while migrating, they will spontaneously recombine with the surface in a process analogous to Frenkel pair recombination. The border inside a Mo crystal beyond which no spontaneous recombination with the surface occurs is not uniformly planar, because the surface recombination probability depends on the orientation of the split interstitial at the end of a collision sequence relative to the surface: *e.g.* split interstitials that are directed parallel to the surface are more stable than others.

To gain more insight into the self-interstitial generation process, MARLOWE calculations have been performed which included replacement collision sequences. To account for the surface recombination, use was made of an effective recombination depth ϵ which has been introduced by Van Veen *et al.*[5]. They assume that beyond this depth the surface recombination probability equals 0 and beneath this depth it equals 1. Thus, the average depth L at which stable self-interstitials are generated is given by

$$L = \epsilon + \frac{\int_{\epsilon}^{\infty} (z-\epsilon)\frac{dN}{dz}dz}{\int_{\epsilon}^{\infty} \frac{dN}{dz}dz} , \qquad (3.2)$$

where z is the distance to the surface, and dN/dz the depth distribution of the self-interstitials immediately after their production. The number of stable self-interstitials generated per argon ion α follows from

$$\alpha = \frac{1}{P} \int_{\epsilon}^{\infty} \frac{dN}{dz} dz \cdot \tag{3.3}$$

The stationary concentration of self-interstitials beyond the distance L during the argon bombardment can be approximated by equation 1.6, with L replaced by L-ϵ. The self-interstitial capture coefficient μ can be described by[3]

$$\mu = c_t \, a_o \, \alpha \, (L-\epsilon), \tag{3.4}$$

where c_t is a geometrical constant (for bcc metals $c_t \approx 20$) and a_o the lattice unit.

The MARLOWE calculations yielded dN/dz for different argon ion energies, and with equations 3.2-3.4 μ could be calculated for different values of ϵ. The

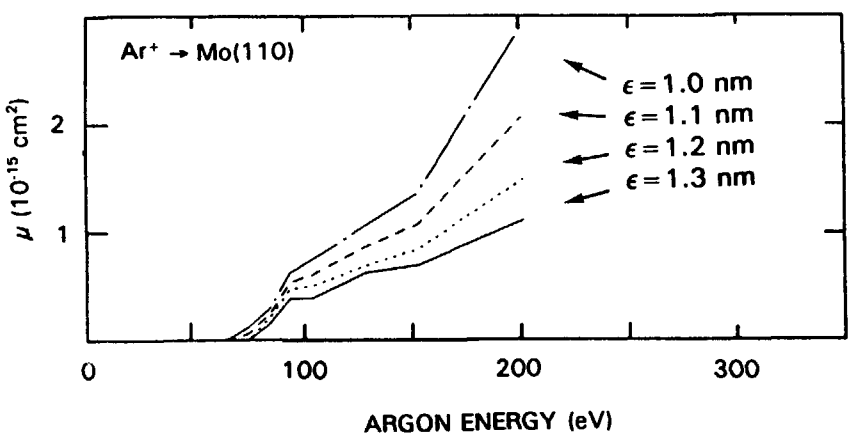

Fig. 3.6. Calculated self-interstitial capture coefficient μ versus argon ion energy for various effective recombination depths ϵ. The curves are drawn to guide the eye.

result is shown in fig. 3.6. A comparison between figs. 3.6 and 3.4 shows that the best fit is obtained with $\epsilon \approx 1.2$ nm. It should be noted that according to the MARLOWE calculations most of the collision sequences ended only one or two lattice units deeper than ϵ, and therefore the value of ϵ is quite critical.

The replacement collision sequences that require the lowest impact energies are those in the closed packed directions, *i.e.* <111> and <100> for bcc metals and <110> and <100> for fcc metals. Calculations based on

molecular dynamics by Bullough[14] have shown that the threshold energy for replacement collision sequences in Mo in the <111> direction equals 45 eV. This implies that, if one wants to induce a sequence in the <111> direction by perpendicularly bombarding a Mo(110) crystal with argon ions, an argon ion energy is required of at least 82 eV (see equation 1.1). This value is in very good agreement with the experimentally obtained threshold energy of (80 ± 5) eV. Van Veen *et al.* have measured threshold values for Xe on W(100) of (50 ± 10) eV and for Ar on Ni(110) of (25 ± 3) eV, and found these values to be in good agreement with MARLOWE calculations that included collision sequences. The role of replacement collision sequences in the novel self-interstitial production technique has thus more strongly been established.

In both the figs. 3.4 and 3.6 μ increases very rapidly just above the threshold energy, but soon increases at a much slower rate. This might be accounted for by the fact that, as long as the transferred energy is lower than twice the threshold energy, still only one replacement collision sequence can be initiated per argon ion. At high argon energies the above model with a recombination depth ϵ is not longer valid: vacancies will be created in deeper layers and these will annihilate the self-interstitials. Besides, the amount of damage then produced will defocus and shorten the replacement collision sequences. The MARLOWE calculations showed that the increase in μ at higher energies is nearly entirely due to an increase in α and not in the depth L at which the self-interstitials are generated.

3.3 The influence of self-interstitials on the retention of argon in high fluence argon irradiated molybdenum

3.3.1 Introduction

More than two and a half decades ago the retention and thermal desorption of low energy (≤5 keV) inert gases in tungsten was investigated by Kornelsen[15]. At irradiation doses above 10^{15} cm^{-2} Kornelsen observed a tendency for saturation in the number of trapped atoms which was ascribed to gas-sputtering, *i.e.* the release of trapped gas atoms by incident gas ions. The gas-sputtering was found to proceed by momentum transfer through lattice atoms and not necessarily by matrix-sputtering or direct collisions. The maximum dose Kornelsen applied was 5×10^{16} cm^{-2}, and to the best of our knowledge inert gas retention in metals at higher fluence regimes and such low energies has not been reported since.

This is not true for silicon, where several authors have explored high fluence argon retention, for example Comas and Wolicki[16], Kempf[17], and Wittmaack *et al.*[18]. The former irradiated Si with more than 10^{19} cm^{-2} 1 keV Ar and measured a saturation value of retained Ar of 4×10^{16} cm^{-2}. Wittmaack *et al.*

have investigated high fluence retention of Ar in Si in the energy range between 10 and 500 keV and observed oscillations in argon content during the irradiation which were ascribed to the formation and rupture of blisters.

In general, the theory and the mechanisms involved in high fluence irradiation processes have started to emerge only recently[19]. This is firstly because high fluence processes are assuming importance, not only in plasma facing components in fusion reactors but also in *e.g.* materials created or modified by sputtering processes or surfaces treated under plasma conditions, while secondly an extensive knowledge gained about low fluence processes has now made a more detailed understanding feasible.

In the next sections it is shown that in high fluence irradiation processes self-interstitial atoms may have a considerable influence on the retention of gas atoms.

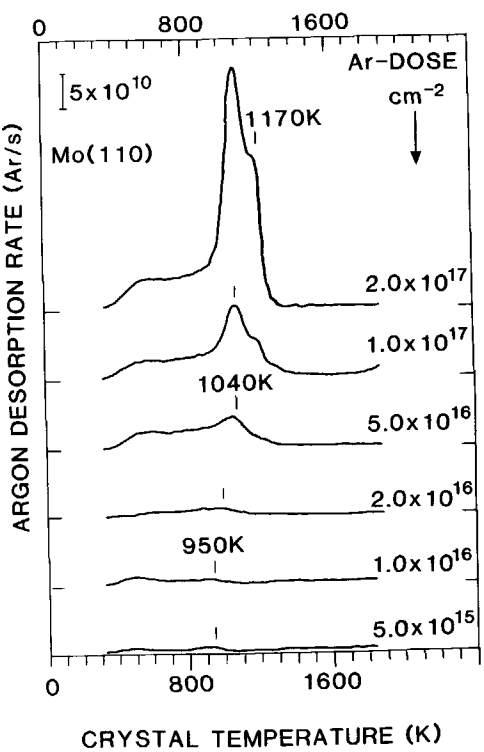

Fig. 3.7. Argon desorption spectra from a Mo(110) single crystal which has been irradiated with 100 eV argon ions. The argon irradiation doses are as indicated.

3.3.2 Experimental results

A Mo(110) sample was irradiated at room temperature with 100 eV Ar in doses ranging from 1.0×10^{14} to 2.0×10^{17} cm^{-2}. The irradiation flux equalled 2×10^{12} $cm^{-2}s^{-1}$. The thermal release of trapped Ar is shown in fig. 3.7 for doses above 5.0×10^{15} cm^{-2} (at lower doses the Ar was always released at ~950 K), and the total amount of trapped Ar (obtained by integration over the whole temperature range) is plotted in fig. 3.8.

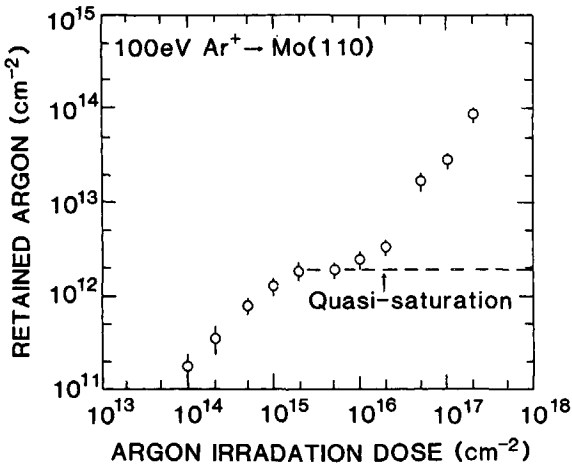

Fig. 3.8. Total amount of retained argon as a function of argon irradiation dose. The dashed line shows quasi-saturation due to gas-sputtering.

It can be seen in fig. 3.7 that with increasing irradiation dose the Ar release peak shifts towards higher temperatures, implying that at higher irradiation doses stronger traps for Ar are formed. Fig. 3.8 shows that after an initial increase of retained Ar with Ar irradiation dose, and a successive tendency for saturation, a renewed increase takes place at argon doses above 10^{16} cm^{-2}. The same effect has been observed for 150 eV Ar. Although the amount of retained Ar was 2 to 3 times higher in this case, the development of the desorption peak structure was identical to that of 100 eV.

TEM observations on the Ar irradiated Mo disclosed (i) dislocation loops with diameters of 10-20 nm and Burgers vectors of $1/2a<110>$ and $1/2a<111>$, where a denotes the lattice unit, and (ii) dislocation segments intersecting the surface perpendicularly, which were only present for Ar doses above $10^{17}cm^{-2}$. The annealing behaviour of the extended defects is shown in fig. 3.9, where it can be observed that upon stepwise annealing to 1150 K the dislocation segments intersecting the surface disappear completely. The 1150 K in the

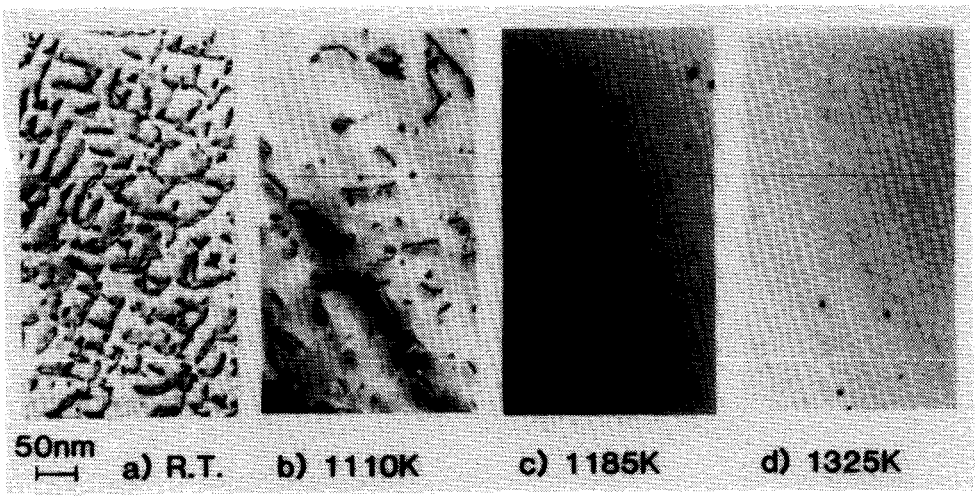

Fig. 3.9. Electron micrographs of Mo(110) irradiated with $2x10^{17}$ cm^{-2} 150 eV Ar. (a) No annealing; self-interstitial loops and dislocation segments intersecting the surface are visible. (b)-(d) Annealing for 5 minutes at the temperatures indicated; the dislocation segments intersecting the surface have disappeared at 1185 K, the self-interstitial loops in deeper layers have remained.

stepwise annealing (with an effective heating rate of ~0.05 K/s) corresponds to ~1300 K in the thermal desorption experiments (with a heating rate of 40 K/s, see section 2.4). Fig. 3.7 reveals that this temperature coincides with the temperature at which all trapped Ar has been released.

The TEM observations also showed that during the annealing rotation of the larger loops occurred, so that their Burgers vectors became ½a<111>. The most stable loops were those with Burgers vectors parallel to the surface.

3.3.3 Discussion

In section 3.2 it has been reported how the low energy argon bombardment produces replacement collision sequences resulting in (i) vacancies and implanted atoms in surface layers, and (ii) self-interstitials at larger depths which are free to migrate. Fig. 3.9 now demonstrates that these self-interstitials can form clusters, thus giving rise to dislocation loops. This is in agreement with results obtained by Ogilvie *et al.*[6], Bowden and Brandon[7], and Venables and Baluffi[8,9].

Further it is noteworthy that the dislocation segments intersecting the surface are only present at fluence regimes where fig. 3.8 exhibits a renewed increase in retained argon. This indicates that the dislocation segments grow and are stabilized by virtue of the mutual interaction between the shallowly

implanted argon and the self-interstitials. Note that according to MARLOWE calculations the penetration depth of 100 eV Ar on Mo(110) is less than half a lattice unit, but obviously the Ar may end up in deeper layers due to irradiation-induced transport mechanisms or channeling.

To check whether the nucleation and growth of self-interstitial/argon complexes is plausible, atomistic calculations have been performed based on the Finnis-Sinclair potential for atom-embedding[20]. These calculations showed that when a substitutional argon atom is positioned in the third atomic layer from the surface, it will trap a self-interstitial atom with a binding energy of 0.45 eV. The binding energy of a second self-interstitial mounts to 1.45 eV, and this easily proves that the nucleation of self-interstitial/argon complexes is likely to occur.

These complexes have a large sink strength for newly arriving argon atoms, thus giving rise to a significant increase in argon trapping. When more self-interstitials and argon atoms are added, dislocation segments decorated with and stabilized by argon are presumably formed. This ties in with the observation that for increasing argon doses the argon is bound more tightly. On annealing, the complexes dissociate, thus explaining why the argon desorption and the disappearance of the segments occur simultaneously.

A dramatic increase in 100 eV Ar trapping after sputtering with 10^{16} cm^{-2} argon has also been observed by Edwards[21] for a Ni surface; this result could well be due to irradiation induced substructures as described above.

Another effect which occurs at higher doses is that the distribution of vacancies and self-interstitials is not spatially random. If a self-interstitial is deposited close to a pre-existing vacancy the two will combine and create an undamaged region, whereas the self-interstitial is likely to survive if it comes to rest close to a pre-existing interstitial. This "Lück-Sizmann effect" yields separated regions with either interstitial clusters or vacancy clusters[22,23].

By comparing fig. 3.8 to the results of Kornelsen it appears that the saturation due to gas-sputtering observed by Kornelsen is quasi-saturation. The saturation effect of gas-sputtering is also perceived in the present work, but at doses above those employed by Kornelsen, the influence of argon accumulation at self-interstitial/argon complexes starts to dominate. Note that the trapping of self-interstitials at these complexes implies that there are fewer available for the gas-sputtering mechanism.

An attempt has been made to simulate the gas-sputtering process by using a computer model based on a depth-dependent cross-section for gas-sputtering. This cross-section $\sigma(x)$ is given by:

$$\sigma(x) = \sigma(0) \exp(-x/L_a), \qquad (3.5)$$

where x is the distance to the surface and L_a an effective absorption length

for released argon. The argon concentration c(x,t) per cubic centimeter is calculated from

$$\frac{\partial c}{\partial t} = J\,I(x) - J\,c\,\sigma(x) + v\frac{\partial c}{\partial x}, \qquad (3.6)$$

where J denotes the argon flux, I(x) the implantation profile and v the speed of surface recession. The last three terms describe respectively the implantation, the gas-sputtering, and the surface motion due to matrix-sputtering. The speed of surface recession due to matrix-sputtering is given by

$$v = JY/N_o \qquad (3.7)$$

with Y the matrix-sputtering yield (for 100 eV Ar on Mo Y equals 0.13) and N_o the atomic density of molybdenum. Fitting this model to the data of fig. 3.8 yielded that $\sigma(0) = 10^{-14}$ cm^{-2} and $L_* = 0.45$ nm. The effects of argon incorporation and irradiation induced substructures have not been included in the model.

3.4 A comparison with silicon

3.4.1 Introduction

In order to gain more insight into the retention of low energy high fluence gas atoms, the above mentioned experiments have also been carried out on silicon. Silicon is not a fusion reactor material, but due to its applications in the semiconductor industry, silicon is a widely investigated material which enables comparison with other research.

In the experiments on silicon described below, 1 keV argon bombardment has been applied instead of the 100 eV argon bombardment which was used in the molybdenum case. Due to the lower atomic mass of silicon and the higher energy, the argon atoms did not only end up in the very first atomic layer at the surface, but also in deeper layers (the range of 1 keV argon on silicon given by TRIM is 2.4 nm and by MARLOWE 2.8 nm). This higher range allowed to study the influence of argon bubbles.

3.4.2 Experimental results

A single crystalline Si(111) sample of 8 mm diameter was irradiated at room temperature with 1 keV Ar in doses ranging from 2×10^{13} to 2×10^{19} cm^{-2}. The irradiation flux equalled 3×10^{15} cm^{-2}s^{-1}. Fig. 3.10 shows the thermal release

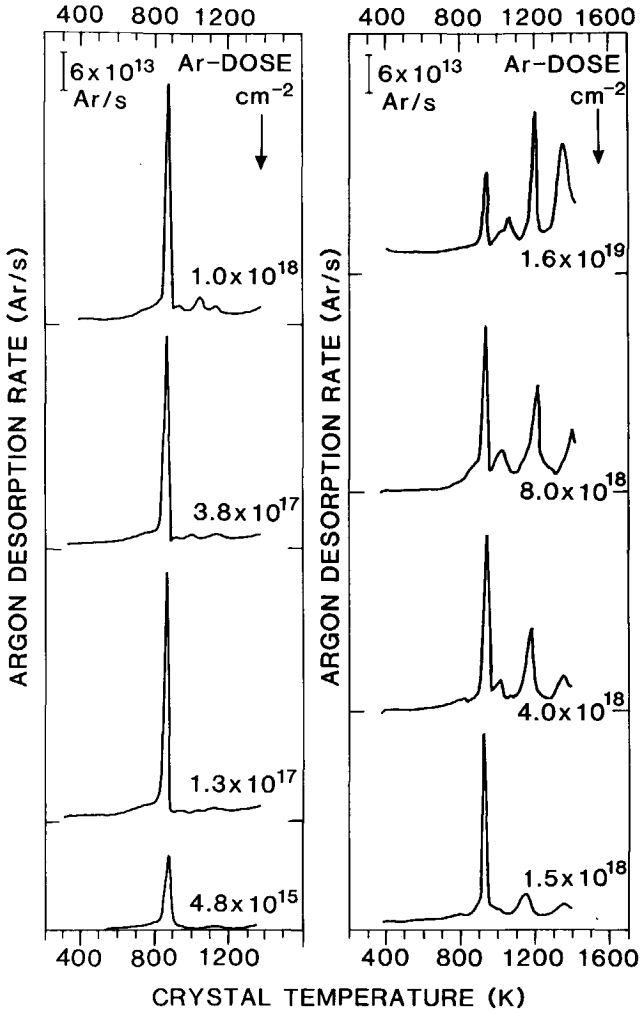

Fig. 3.10. Argon desorption spectra from a Si(110) single crystal which has been irradiated with 1 keV Ar^+. The argon irradiation doses are as indicated.

of the trapped argon and fig. 3.11 the total amount of trapped argon. It is seen in fig. 3.10 that with increasing argon dose a peak structure evolves at higher desorption temperatures, implying that, as in the results for molybdenum, the argon similarly gets bound more strongly. Also the argon retention shows an analogous behaviour: an initial linear increase in argon content with argon irradiation dose, then a tendency towards saturation, and at doses above 5×10^{17} cm^{-2} a renewed increase in argon content. The dashed curve in fig. 3.11 represents a fit obtained with the computer model for gas-sputtering with $\sigma(0) = 3\times10^{-14}$ cm^{-2} and $L_a = 0.45$ nm.

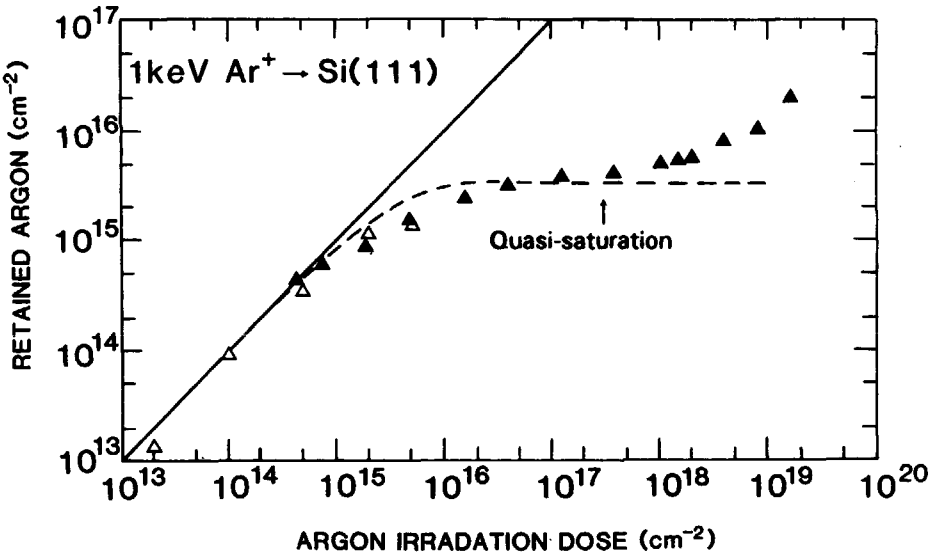

Fig. 3.11. Total amount of retained argon as a function of argon irradiation dose. The dashed line shows the contribution of gas-sputtering calculated with the model of section 3.3.3.

3.4.3 Discussion

Unlike metals, silicon may be rendered amorphous when subjected to room temperature irradiation. After the argon irradiation, the argon is expected to be present both atomically dispersed and in the form of bubbles. On annealing, the silicon recrystallizes and the shallowly implanted argon is swept out by the recrystallization front[24,25]. The extremely sharp desorption peak which becomes manifest due to this process at ~875 K is visible in fig. 3.10.

At irradiation doses above 10^{18} cm^{-2} the recrystallization peak at ~875 K starts to shrink while desorption peaks at higher temperatures start to grow, indicating that another release mechanism takes over. Although a detailed assignment of the desorption peaks at higher temperatures is not yet within reach, it is clear that they represent defects that survive recrystallization. TEM observations by Bangert *et al.*[26] have shown the presence of argon bubbles that are stable far above the recrystallization temperature after 10^{17} cm^{-2} 2-5 keV argon bombardment on Si(100). This indicates that the argon desorption at higher temperatures is at least partly associated with argon bubbles. Since large argon bubbles trap argon atoms more efficiently and more strongly than small ones, we believe that the renewed increase in argon retention at doses beyond 5×10^{17} cm^{-2} is caused by the nucleation and growth of these argon bubbles. Although bubbles in bulk material may also occur in molybdenum,

these are not expected to be formed as readily as in silicon: due to the much higher atomic mass of molybdenum (95.94 *vs* 28.09), the argon does not penetrate as deep in molybdenum as in silicon. In the present experiment, the argon ranges calculated by MARLOWE were only 0.2 nm for 100 eV argon on Mo(110) and 2.8 nm for 1 keV argon on the Si(111).

To account for the fact that the bubbles in silicon are very stable to annealing, Bangert *et al.* presumed that oxygen is able to stabilize the bubbles, an idea that has been confirmed for helium bubbles by Evans *et al.*[27]. Bean *et al.*[28], however, have observed extended dislocation networks after 1 keV Ar bombardment, which were also stable upto at least 1073 K. Consequently, it is envisaged that, similarly to the molybdenum case, there is a mutual stabilizing interaction between dislocation networks and argon bubbles. The production of self-interstitials that give rise to dislocation networks does not proceed as efficiently in the silicon as in the molybdenum experiments however, since in the silicon the process is hindered by amorphization and by vacancies which are created in deeper layers than the very surface layer.

For more than 10^{19} cm^{-2} 1 keV Ar on silicon, Comas and Wolicki[16] have measured a saturation value of retained argon of $4x10^{16}$ cm^{-2}, which is consistent with the results of fig. 3.11. Apparently, this is not a saturation due to gas-sputtering as described by Kornelsen: the experimental results have shown that with increasing argon dose the argon is bound more strongly, and this implies that the cross section for gas-sputtering introduced in section 3.3.3 decreases. The leading process causing the saturation in the dose regime of 10^{19} cm^{-2} must be matrix-sputtering. Kornelsen has shown that at low doses gas release via matrix-sputtering is much less important than gas release via momentum transfer to the gas atoms. However, this is not the case in the dose regimes of Comas and Wolicki where the argon concentration is of the same order of magnitude as the silicon concentration. Here, the argon will be present in closely packed bubbles very near the surface and matrix-sputtering will easily cause the rupture of these bubbles, thus establishing a new equilibrium between implanted and released argon. An additional effect at high doses is that bubbles become overpressurized when argon atoms are added. This leads to interbubble fracture and cracks that may serve as a drain to the surface for the argon.

In molybdenum, matrix-sputtering does not take place as readily as in silicon, because the much higher atomic mass of molybdenum makes the energy transfer from impinging argon ions to matrix atoms less efficient.

3.5 Conclusions

It has been corroborated that low energy heavy ion bombardment provides a useful technique for the controlled production of stable self-interstitial atoms. The role of replacement collision sequences in the self-interstitial production process has more strongly been established and threshold energies have been accounted for.

By using the novel technique, it has been studied what influence self-interstitial atoms may have on the retention of gas atoms in fusion reactor materials. It has been shown that the retention of argon in low energy high fluence argon irradiated molybdenum and silicon cannot be described by a linear superposition of low fluence trapping processes. This fact is not just due to the effect of gas-sputtering, but also to the intimate interaction between deposited argon and irradiation induced self-interstitials. It has become evident that the saturation in argon retention due to gas-sputtering which has been reported by Kornelsen is quasi-saturation. At fluences higher than those explored by Kornelsen, the argon retention is governed by relatively stable defect complexes consisting of self-interstitials and argon atoms. In these fluence regimes, dislocation segments and argon bubbles may be formed which stabilize each other. The influence of the irradiation temperature on the nucleation and growth of these complexes has not been discussed, but it is known that the argon retention depends significantly on the temperature[26]. This knowledge provides ample room for further research.

References chapter 3

1. See *e.g.* H. van Swygenhoven, G. Knuyt and L.M. Stals, J. Nucl. Mater. **127** (1985) 97.
2. A.Y. Stathopoulos, S.M. Murphy, M.H. Wood, R. Bullough and C.A. English, J. Nucl. Mater. **110** (1982) 301.
3. A. van Veen and L.M. Caspers, in: Proc. Consultants Symp. on Inert Gases in Metals (AERE report 9733, Harwell, 1980) p. 494.
4. A. van Veen, W.Th.M. Buters, G.J. van der Kolk, L.M. Caspers and T.R. Armstrong, Nucl. Instr. and Meth. **194** (1982) 485.
5. A. van Veen, W. Th. M. Buters, T.R. Armstrong, B. Nielsen, K.T. Westerduin, L.M. Caspers and J. Th. M. de Hosson, Nucl. Instr. and Meth. **209/210** (1983) 1055.
6. G.J. Ogilvie, J.V. Saunders and A.A. Thompson, J. Phys. Chem. Solids **24** (1963) 247.
7. P. Bowden and D.G. Brandon, Phil. Mag. **8** (1963) 935.
8. J.A. Venables and R.W. Baluffi, Phil. Mag. **11** (1965) 1022.

9. J.A. Venables, Proc. Atomic collision phenomena in solids, eds. D.W. Palmer, M.W. Thompson and P.D. Townsend (North-Holland, Amsterdam, 1970), p. 133.
10. T. Bullough, C.A. English and B.L. Eyre, Materials Science Forum **15-18** (1987) 1069.
11. J.R. Beeler, Jr., Radiation effects computer experiments (North-Holland, New York, 1983).
12. R.N. Stuart, M.W. Guinan and R.J. Borg, Rad. Eff. **30** (1976) 129.
13. A. van Veen, J.H. Evans, W.Th.M. Buters and L.M. Caspers, Rad. Eff. **78** (1983) 53.
14. J. Bullough, oral communication.
15. E.V. Kornelsen, Canad. J. Phys. **42** (1964) 364.
16. J. Comas and E.A. Wolicki, J. Electrochem. Soc., Solid State Science **117** (1970) 1197.
17. J. Kempf, Appl. Phys. **16** (1978) 43.
18. K. Wittmaack, P. Blanck and W. Wach, Rad. Eff. **39** (1978) 81.
19. G. Carter, I.V. Katardjiev and M.J. Nobes, in: Materials Modification by High Fluence Ion Beams, eds. R. Kelly and M. Fernanda da Silva, NATO ASI series E **155** (Kluwer, Dordrecht, 1989) 3.
20. M.W. Finnis and J.E. Sinclair, Phil. Mag. A **50** (1984) 45.
21. D. Edwards Jr., J. Appl. Phys. **46** (1975) 1437.
22. G. Lück and R. Sizmann, Phys. Stat. Sol. **6** (1964) 263.
23. A. Seeger, Radiation Effects and Defects in Solids **111-112** (1-2) (1989) 355.
24. A. van Veen, P.C. de Jong, K.R. Bijkerk, H.A. Filius and J.H. Evans, in: Fundamentals of Beam-Solid Interactions and Transient Thermal Processing, eds. M.J. Aziz, L.E. Rehn and B. Stritzker, Proc. Mat. Res. Soc. **100** (MRS, Pittsburg, Pennsylvania, 1988) p. 231.
25. A. Taoufik, A. Chouiyakh and B. Lang, Rad. Eff. **104** (1987) 117.
26. U. Bangert, P.J. Goodhew, C. Jeynes and I.H. Wilson, J. Phys. D **19** (1986) 589.
27. J.H. Evans, A. van Veen and C.C. Griffioen, Nucl. Instr. and Meth. B **28** (1987) 360.
28. J.C. Bean, G.E. Becker, P.M. Petroff and T.E. Seidel, J. Appl. Phys. **48** (1977) 907.

Chapter 4
The interaction of vacancies with hydrogen and nitrogen in molybdenum

4.1 Introduction

Thermal helium desorption spectrometry provides a sensitive technique for measuring the concentration of vacancy type defects at low defect concentrations. In section 4.2 it is shown how the technique has been used to measure vacancy annealing curves in Mo(110). It is demonstrated how the vacancy migration energy can be derived from the annealing curves by using a simple diffusion model. In section 4.3 it is examined whether the presence of hydrogen has any measurable effect on the vacancy annealing curves, and an attempt is made to estimate the dissociation energy of hydrogen bound to a vacancy. Section 4.4 is allotted to the interaction between vacancies and nitrogen in molybdenum. In this section, novel defect assignment methods are applied to corroborate previously obtained results concerning the dissociation of a nitrogen atom bound to a vacancy. In section 4.5, finally, the capabilities of THDS are explored by studying the influence of nitrogen on the annealing behaviour of small vacancy clusters.

4.2 The annealing behaviour of monovacancies in molybdenum

4.2.1 Introduction

The properties of vacancies in Mo have been studied by several authors employing a variety of experimental techniques both to create the initial vacancy population and to measure the resulting concentrations. For example, Schwirtlich and Schultz[1] have used electrical resistivity annealing measurements to determine the monovacancy formation energy (3.20 eV), the monovacancy formation entropy (1.5 k) and the monovacancy migration energy (1.35 eV) in single crystalline molybdenum. The vacancies were produced by quenching the sample in superfluid helium from high temperatures. For tungsten, Schwirtlich and Schultz found a monovacancy formation energy of 3.67 eV and a monovacancy migration energy of 1.78 eV. Maier *et al.*[2] have also derived these parameters for a range of bcc metals by carrying out positron annihilation measurements. For molybdenum they found a monovacancy formation energy of (3.0 ± 0.2) eV and a monovacancy migration energy of (1.5 ± 0.2) eV.

In this section it is shown how thermal helium desorption spectrometry is utilized to measure the vacancy migration energy in single crystalline Mo

irradiated with low energy (≤3 keV) helium ions. Since the THDS technique is extremely sensitive to vacancies, low defect concentrations can be used and therefore phenomena such as retrapping[3] and vacancy clustering can be neglected in determining the vacancy migration energy E_V^M. Moreover, E_V^M can be derived from the experimental data without assuming a vacancy sink strength, since all of the damage is created close to the sample surface and the surface acts as an infinite sink once the vacancies become mobile.

There are however disadvantages to the THDS technique. Firstly, it is necessary to know the distribution of the vacancies produced during the initial damaging irradiation. Secondly, because the technique is destructive (*i.e.* the vacancy population is destroyed during the measurement), it is necessary to create a new vacancy population for each annealing step. These vacancy populations are not always identical, and therefore a certain amount of scatter occurs in the data points.

Both the advantages and the disadvantages are illustrated in the following subsections which describe annealing experiments on vacancies created by helium ion irradiation. Subsection 4.2.2 describes a simple diffusion model which has been used to extract the vacancy migration energy E_V^M from the experimental results, subsection 4.2.3 presents the experimental results, and in subsection 4.2.4 it is considered how sensitive the obtained value for E_V^M is to variations in the fitting parameters.

4.2.2 Data analysis

The annealing curves obtained from the experiments have been analysed by solving the one-dimensional diffusion equation

$$\frac{\partial c_V(x,t)}{\partial t} = D_V \frac{\partial^2 c_V(x,t)}{\partial x^2} \tag{4.1}$$

where $c_V(x,t)$ is the depth distribution of the vacancies and D_V is the vacancy diffusion coefficient. The initial depth distribution $c_V(x,0)$ of the vacancies created by ion irradiation has been obtained from MARLOWE calculations[4]. At both surfaces the vacancy concentration equals zero, and the boundary conditions are therefore: $c_V(0,t) = 0$ and $c_V(\infty,t) = 0$. D_V can be expressed in terms of E_V^M through the equation

$$D_V = D_o^M \exp -\frac{E_V^M}{kT}, \tag{4.2}$$

where D_o^M is the pre-exponential factor for vacancy migration.

In order to obtain a value for E_V^M from the measured data, equation (4.1) has been solved for different E_V^M values by using Gear's method[5].

Although mainly E_V^M has been adjusted to match the experimental data, it is important to note that in fact D_V is measured, which involves another parameter, *viz* D_o^M (see equation 4.2). Without performing a large number of separate experiments which might allow the exact temperature dependence of D_V to be determined, it is necessary to know D_o^M. In the present work, D_o^M has been obtained from the following relationships

$$D_o^M = \frac{1}{6}\lambda^2 v_o \exp\frac{S_V^M}{k} \tag{4.3}$$

$$D^{SD} = \frac{1}{6}\lambda^2 v_o \exp\frac{S_V^f + S_V^M}{k} \tag{4.4}$$

where λ and v_o denote respectively the average jump distance and the average jump frequency, S_V^M and S_V^f are the entropy of vacancy migration and vacancy formation, and D^{SD} is the pre-exponential factor for self-diffusion. Combining equations 4.3 and 4.4 gives D_o^M in terms of D^{SD} and S_V^f, which can be found in the literature. Using a value of $0.13\text{x}10^{-4}$ m^2s^{-1} for D^{SD} [6] and a value of 1.5 k for S_V^f [1,7] gives $D_o^M = 3\text{x}10^{-6}$ m^2s^{-1}.

Apart from fitting E_V^M, the effect of vacancy clustering on the annealing curves has been examined. In order to do so, the following set of coupled equations has been solved:

$$\frac{\partial c_V}{\partial t} = D_V \frac{\partial^2 c_V}{\partial x^2} - 2K_1 c_V^2 + 2K_2 c_{V_2} \tag{4.5}$$

$$\frac{\partial c_{V_2}}{\partial t} = D_{V_2} \frac{\partial^2 c_{V_2}}{\partial x^2} + K_1 c_V^2 - K_2 c_{V_2} \tag{4.6}$$

where the subscript V refers to monovacancies and the subscript V_2 to divacancies[8]. K_1 is the rate at which monovacancies combine to form divacancies and K_2 is the rate at which the divacancies dissociate. Both K_1 and K_2 have been calculated by using equation 1.4, with $z = 1$[9], $v_o = 10^{14}$ s^{-1}, $S = k$[7], and $E = E_V^M$ for K_1 and $E = E_V^M + E_{V_2}^{B,V} = E_V^M + 0.44$[9] eV for K_2 (see also equation 1.8).

4.2.3 Experimental results

The present experiments have been performed on a Mo sample which was initially irradiated with a fluence of 9×10^{11} cm^{-2} 1 keV helium ions to create vacancies, then annealed to a certain temperature, and finally irradiated with 4×10^{13} cm^{-2} 150 eV helium to probe the remaining vacancies. Figure 4.1 shows the vacancy concentration as a function of the anneal temperature.

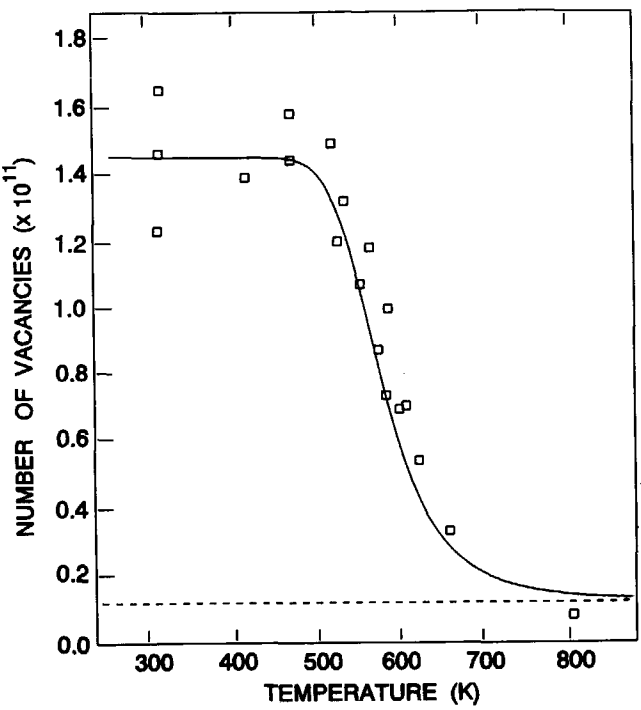

Fig. 4.1. Number of vacancies left after annealing versus anneal temperature. The initial vacancy distribution has been produced by 9×10^{11} cm^{-2} 1 keV He irradiation. The squares represent the experimental data measured by the helium desorption technique. The line has been calculated with $E_V^M = 1.23$ eV.

The solid curve has been calculated using the diffusion model based on equation 4.1. It can be seen in fig. 4.1 that the initial damaging 1 keV He irradiation produced 1.43×10^{11} cm^{-2} vacancies (corresponding to ~0.16 vacancy per incident helium ion), and that the vacancy concentration remains relatively constant for annealing temperatures below 480 K. Above this temperature the vacancy concentration drops rapidly with increasing temperature until at ~700 K almost all of the vacancies have left the sample.

The maximum in the annealing rate occurs at a temperature of 560 K and the annealing step has a full width at half maximum of 55 K. A very small number of vacancies remains at ~800 K because some of the vacancies trap a helium atom during the initial 1 keV irradiation. The trapped helium atom stabilizes the vacancy until it is released at ~1170 K (see section 2.4).

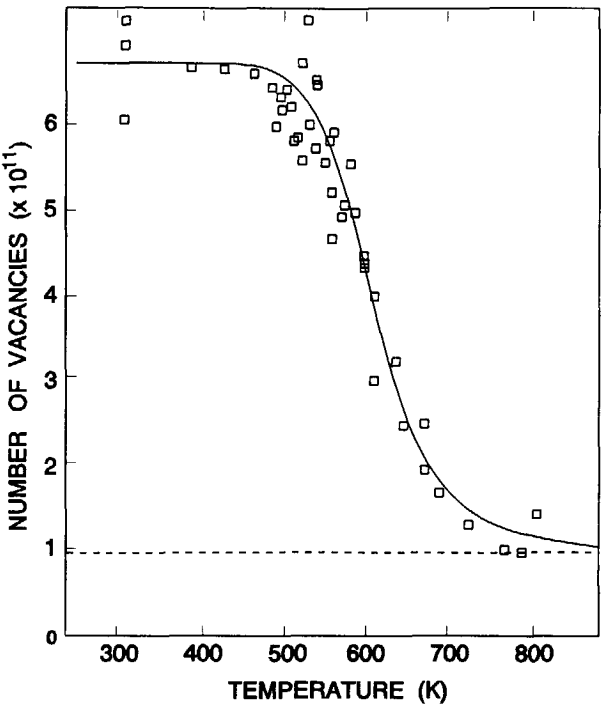

Fig. 4.2. Number of vacancies left after annealing versus anneal temperature. The initial vacancy distribution has been produced by 9×10^{11} cm^{-2} 3 keV He irradiation. The squares represent the experimental data measured by the helium desorption technique. The line has been calculated with $E_V^M = 1.23$ eV.

Fig. 4.2 shows similar data as fig. 4.1 but for an initial irradiation with 3 keV instead of 1 keV helium ions. Again, the solid curve has been calculated using the diffusion model. The general features of the data are similar to the data from the 1 keV irradiation although the unannealed vacancy concentration differs (~0.76 vacancy per helium ion instead of ~0.16). It can be deduced from fig. 4.2 that in the 3 keV experiment approximately 15% of the vacancies remain at temperatures above 700 K (*cf.* 7% in the 1 keV experiment). These are vacancies immobilized by helium atoms.

4.2.4 Discussion

It can be observed in figs. 4.1 and 4.2 that there is good agreement between the experimental data and the calculated curve. In the calculations, E_V^M has been adjusted to match the experimental curve, and the most suitable value of E_V^M, determined by least square fitting, is found to be (1.23 ± 0.04) eV.

It has already been remarked that the E_V^M value obtained depends on the value of D_o^M used in the calculations. To check whether the value of D_o^M obtained from the literature yields the best fitting result, the calculations have been repeated for several other values of D_o^M, ranging from 10^{-8} m^2s^{-1} to 10^{-4} m^2s^{-1}. It turned out that the best least square fit was indeed obtained with the literature value for D_o^M of $3x10^{-6}$ m^2s^{-1} and the value for E_V^M of 1.23 eV. The only other variable in the data analysis is the depth distribution of the vacancies produced by the helium irradiation. To examine the sensitivity of E_V^M to changes in the vacancy depth distribution, annealing curves have been calculated for depth distributions with ranges differing by 33% and stragglings by 20% from those given by the MARLOWE program. It was found that this produces a variation in E_V^M of approximately 4%. Thus, the calculated value of E_V^M is not very sensitive to variations in the assumed vacancy depth distribution.

In all of the present experiments, the vacancy concentrations were low and the damage was created close to the sample surface. This means that the probability of a free interstitial atom annihilating a vacancy other than its own is virtually negligible (Hou *et al.*[10] have calculated the effective recombination radius for correlated vacancy-interstitial recombination to be 1.16 nm).

To estimate the effect of vacancy clustering on the annealing curves, calculations have been performed which were based on the equations 4.5 and 4.6. D_{V_2} was chosen to be 0 to obtain maximum effect. The results showed that in the present experiments an effect of vacancy clustering was negligible: the maximum number of divacancies was found to be a factor 10^4 lower than the number of monovacancies. This can be attributed to the small number of vacancies present in the sample.

The obtained value of (1.23 ± 0.04) eV for the monovacancy migration energy is lower than the 1.35 eV that Schwirtlich and Schultz[1] derived from resistivity measurements, and the value of 1.5 eV that Maier *et al.*[2] obtained from positron annihilation experiments. In both the resistivity and the positron experiments however retrapping and vacancy clustering has occurred, and the values of 1.35 and 1.5 eV are therefore believed to be less correct than the (1.23 ± 0.04) eV found here. Hence, it is concluded that the best value for the monovacancy migration energy in molybdenum is (1.23 ± 0.04) eV.

4.3 The interaction between monovacancies and hydrogen in Mo

4.3.1 Introduction

To investigate whether the presence of hydrogen has a measurable effect on the vacancy annealing curves, and to examine whether the THDS technique can be used to determine the hydrogen-vacancy dissociation energy in molybdenum $E_{HV}^{D,H}$, experiments have been carried out on a Mo(110) sample irradiated with hydrogen. In section 4.3.2 the experimental results are described and in section 4.3.3 the results are discussed. It should be noted that direct thermal hydrogen desorption experiments are quite difficult to perform since hydrogen is always present as a background gas in the vacuum system. Moreover, hydrogen is chemisorbed on a Mo(110) surface in two states with binding energies of 1.2 and 1.5 eV[11], which obscures all processes below the surface having lower activation energies. In the experiments reported here, helium was therefore used as a probe.

4.3.2 Experimental results

Fig. 4.3 shows a vacancy annealing curve similar to those in figs. 4.1 and 4.2 but now for an initial irradiation of 2.8×10^{13} cm^{-2} 3 keV H_2 ions instead of He ions (this dose is approximately equivalent to 5.6×10^{13} cm^{-2} 1.5 keV protons). As before, the initial irradiation was followed by annealing and a 4×10^{13} cm^{-2} 150 eV helium irradiation. The general features of the experimental data in fig. 4.3 are similar to those in figs. 4.1 and 4.2. The only difference is that in the hydrogen experiment all vacancies have gone at a temperature of 700 K.

To study the effect of adding hydrogen to empty vacancies, the experiment of fig. 4.2 was repeated but with an additional hydrogen irradiation step. The vacancies, created by 9×10^{11} cm^{-2} 3 keV He irradiation, were filled with hydrogen by exposing the sample to a fluence of 2×10^{11} cm^{-2} 0.7 keV H_2 ions. An energy of 0.7 keV is sufficiently low to assure that no additional damage is created in the sample. After the 0.7 keV H_2 irradiation, the sample was annealed and filled with low energy helium, exactly the same as in the experiment of fig. 4.2. The presence of additional hydrogen in the vacancies did not have a measurable effect upon the annealing curve however: no significant difference was found with fig. 4.2.

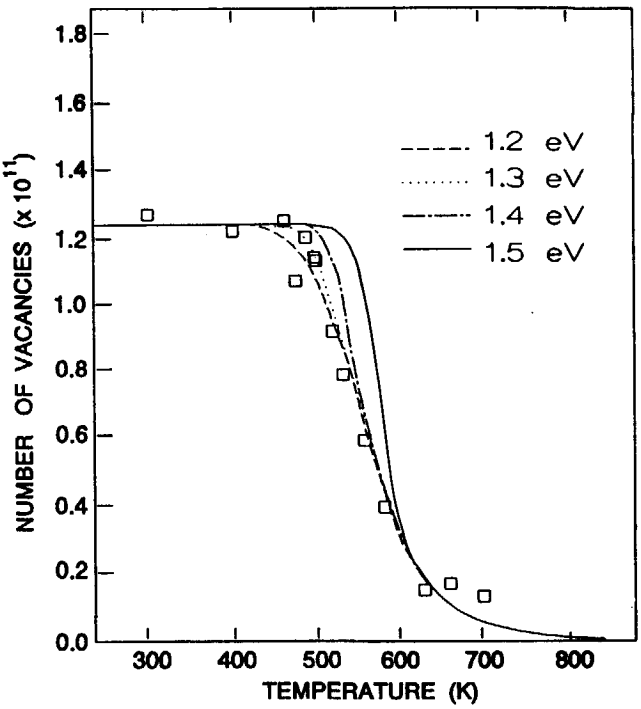

Fig. 4.3. Number of vacancies left after annealing versus anneal temperature. The initial vacancy distribution has been produced by 2.8×10^{13} cm^{-2} 3 keV H_2 irradiation. The squares represent the experimental data measured by the helium desorption technique. The lines have been calculated with a reaction diffusion equation for the indicated values of $E_{HV}^{D,H}$ with $E_V^M = 1.23$ eV.

4.3.3 Discussion

The fact that the influence of hydrogen is not reflected in the annealing curves implies that the exact value of $E_{HV}^{D,H}$ cannot be extracted from the measured data. Nonetheless, it is possible to make an estimate of the smallest hydrogen-vacancy dissociation energy which should have been observed in the annealing curves. In order to do so, calculations have been performed for different dissociation energies. In these calculations it was assumed that the vacancies were initially filled with hydrogen and the hydrogen filled vacancies were taken immobile. The following set of equations was applied:

$$\frac{\partial c_V}{\partial t} = D_V \frac{\partial^2 c_V}{\partial x^2} + \nu c_{HV} \tag{4.7}$$

$$\frac{\partial c_{HV}}{\partial t} = -\nu c_{HV} \tag{4.8}$$

$$\nu = \nu_o \exp \frac{-E_{HV}^{D,H}}{kT} \qquad (4.9)$$

where the subscript HV refers to hydrogen filled vacancies.

The results of some of the calculations are shown in fig. 4.3. Examination of the curves shows for example that a dissociation energy of 1.5 eV should have produced a delay in the recovery of ~100 K. Bearing this in mind, it can be deduced from fig. 4.3 that the dissociation energy of a hydrogen atom bound to a vacancy must be less than 1.4 eV. This is in agreement with experimentally and theoretically obtained deuterium dissociation energies of respectively 1.38 eV and 1.31 eV reported by Myers and Besenbacher[12] (in which a deuterium migration energy of 0.35 eV was assumed[13]). It is also in agreement with the hydrogen dissociation energy of 1.19 eV reported by Doyle and Brice[14].

Linderoth *et al.*[15] and Hansen *et al.*[13] have carried out positron experiments on the hydrogen-vacancy interaction in molybdenum. They observed a delay in vacancy clustering due to hydrogen of about 25 K and reported a maximum value of 1.7 eV for the hydrogen-vacancy dissociation energy, which is higher than our value of 1.4 eV. The value of 1.7 eV however is ascribed to hydrogen release from small vacancy clusters rather than from single vacancies.

Eleveld *et al.*[16] have determined the deuterium-vacancy disscociation energy in tungsten. By fitting data obtained from deuterium desorption experiments, they found a value for $E_{DV}^{D,D}$ in tungsten of (1.43 ± 0.02) eV. When the relative melting points of molybdenum and tungsten are considered (2890 K and 3683 K respectively), it is expected that $E_{HV}^{D,H}$ in molybdenum is less than $E_{DV}^{D,D}$ in tungsten (this expectation is based on the experimental finding that activation energies tend to be related to the melting point). Thus, the above conclusion that $E_{HV}^{D,H}$ in molybdenum is less than 1.4 eV compares well with the value of (1.43 ± 0.02) eV found for tungsten.

4.4 The interaction between monovacancies and nitrogen in Mo

4.4.1 Introduction

The first THDS experiments on nitrogen irradiated molybdenum have been performed by Van Veen and Caspers[17], who showed that nitrogen atoms (N) trapped by vacancies (V) prevent the vacancies from migrating. The defects consisting of a vacancy filled with a nitrogen atom (NV) were found to disappear by dissociation rather than by diffusion at a temperature well beyond the vacancy migration temperature. The NV dissociation energy in molybdenum was determined to be (2.55 ± 0.05 eV).

In order to corroborate the results obtained by Van Veen and Caspers, this section describes further experiments on molybdenum in which use was made of both the positron annihilation technique and the THDS technique. In section 4.4.2 results of positron annihilation experiments are presented, which show a total suppression of vacancy migration in two electron irradiated molybdenum single crystals which contained 200 ppm nitrogen. In section 4.4.3 THDS experiments on the helium filling behaviour of the suspected NV defects are presented, and section 4.4.4 describes an investigation into the annihilation of the suspected NV defects by self-interstitials. In the latter, use was made of the self-interstitial production method described in section 3.2. Section 4.4.5 finally, describes some theoretical considerations concerning the dissociation order of HeNV defects in molybdenum.

4.4.2 Positron annihilation results

In order to study the influence of nitrogen on the production and recovery of vacancies, two molybdenum samples were prepared in the following way. Firstly, interstitial nitrogen was introduced in the samples in a concentration of ~ 200 ppm by keeping the samples in a pure nitrogen gas at 1973 K until thermal equilibrium was reached[18]. After this, the samples were quenched to room temperature at which nitrogen is immobile. To create Frenkel pairs in the samples they were irradiated with 2 MeV electrons at 333 K. A pure Mo sample was also irradiated for comparison.

After preparing the samples, they were isochronally annealed in vacuum ($< 10^{-6}$ Pa), and after each annealing they were subjected to positron lifetime measurements. The measurements were analysed in terms of two positron lifetime components. The short lifetime component τ_1, which reflects the trapping of positrons in bulk material, was in agreement with the predictions of the two state trapping model[19]. The long lifetime component τ_2 and its intensity I_2, which reflect the trapping of positrons at vacancies, are shown in fig. 4.4.

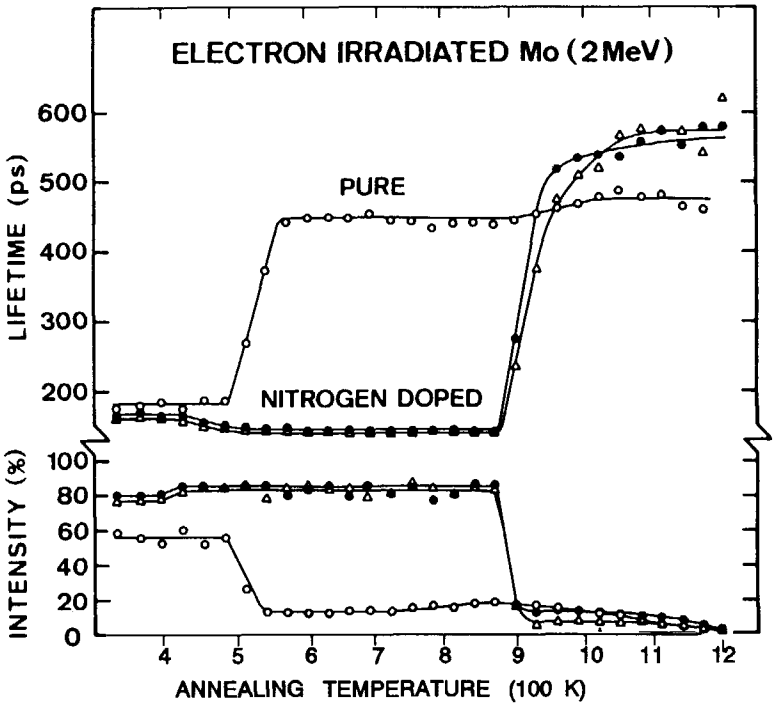

Fig. 4.4. The effect of nitrogen on the recovery of an electron irradiated Mo single crystal. The positron lifetime τ_2 and its intensity I_2 are shown as a function of annealing temperature for:

- △ Mo doped with 200 ppm nitrogen and electron irradiated at 330 K to a dose of 2.5×10^{18} cm^{-2};
- • Mo doped with 200 ppm nitrogen and electron irradiated at 330 K to a dose of 4.0×10^{18} cm^{-2};
- o Pure Mo electron irradiated to a dose of 2.0×10^{19} cm^{-2}.

To estimate the number of vacancies produced during the irradiation, the positron lifetime data were analysed by using the two state trapping model[19]. For the pure Mo sample the vacancy concentration was thus estimated to be 14 ppm after an electron dose of 2.0×10^{19} cm^{-2}. For the two nitrogen doped samples the vacancy concentrations were 26 ppm and 36 ppm after respectively 2.5×10^{18} and 4×10^{18} cm^{-2} electron irradiation. Apparently the presence of nitrogen causes an increase in vacancy production by approximately a factor 15. This can be explained by the fact that nitrogen forms traps for the mobile self-interstitials, thus reducing the number of interstitials that are able to recombine with vacancies (a process which has been described by Walker[20]).

In the pure Mo sample, the long lifetime component τ_2 at temperatures below 480 K is associated with the trapping of positrons at monovacancies.

This lifetime was measured to be 180 ps. It is seen in fig. 4.4 that in the temperature interval between 480 and 570 K (the so-called stage III region) the long lifetime increases strongly and the intensity I_2 decreases. This is caused by the fact that at these temperatures vacancies in molybdenum can migrate and agglomerate, thus forming fewer but larger defects. Using the two state trapping model, it can be calculated that during the migration the positron trapping rate at defects decreases to 26% of its former value. If it is assumed that the trapping rate per defect is proportional to R^3, where R is the effective radius of the defects[21], it means that 26% of the vacancies remain and form clusters.

In the nitrogen doped samples, the lifetime τ_2 directly after the electron irradiation is lower than in the pure sample, indicating that then already nitrogen atoms are bound to some vacancies (which causes a lower lifetime). At ~430 K a further decrease in the lifetime associated with vacancies is observed, which indicates that an increasing number of nitrogen atoms is bound to vacancies. We attribute this to the migration of interstitial nitrogen, which is in agreement with the literature value for the nitrogen migration energy in molybdenum of 1 eV[22]. According to the two state trapping model[19], a decrease in positron lifetime τ_2 should for constant trapping rate coincide with an increase in intensity I_2; in fig. 4.4 it can be observed that this is indeed the case.

Contrarily to what has been observed for the pure Mo sample, no clustering or loss of vacancies is observed in the temperature interval between 480 and 570 K for the nitrogen doped samples. Apparently, the free migration of vacancies is totally suppressed. This means that nearly all vacancies are at least bound by one nitrogen atom; hence, the average number of nitrogen atoms per vacancy is more than one. This agrees well with the fact that in the nitrogen doped samples the nitrogen concentration (200 ppm) is higher than the vacancy concentration (26 resp. 36 ppm). The fact that the lifetime only decreases to ~145 ps indicates that the nitrogen is not bound to the centre of the vacancy, something which has also been observed for the carbon-vacancy interaction in iron by Hautojärvi *et al.*[23].

The total suppression of vacancy mobility observed in the positron annihilation experiments agrees well with the THDS results obtained by Van Veen and Caspers: nitrogen trapped by vacancies immobilizes the vacancies. The results are also in agreement with those obtained by Anttila and Hirvonen[24] and Hautala *et al.*[25] who have studied the annealing behaviour of 60 keV ^{15}N implanted into polycrystalline Mo by the (p,γ)-resonance broadening technique. They observed an increased solubility of nitrogen and a decrease in overall diffusivity after MeV proton irradiation, which can well be explained by the trapping of nitrogen by proton irradiation induced vacancies.

4.4.3 Helium filling of suspected NV defects in molybdenum

In order to prove that the defects investigated by Van Veen and Caspers are indeed substitutional nitrogen atoms, more THDS experiments have been carried out in which use was made of novel defect assignment methods. The defect state in molybdenum after irradiation with nitrogen ions at ambient temperatures is expected to consist of immobile interstitial and substitutional nitrogen atoms, monovacancies, and perhaps a small number of larger vacancy-nitrogen clusters, dependent on the nitrogen implant energy. Molybdenum self-interstitials are highly mobile at 300 K and will thus get lost, mainly due to migration to the specimen surface. To investigate the as-irradiated structure and the changes in defect structure upon annealing by thermal gas desorption spectrometry, nitrogen cannot be used as a probe, since it is chemisorbed on a molybdenum surface in two states with binding energies of 2.8 eV and 3.3 eV[26]. All processes below the surface which require lower activation energies would thus remain unnoticed.

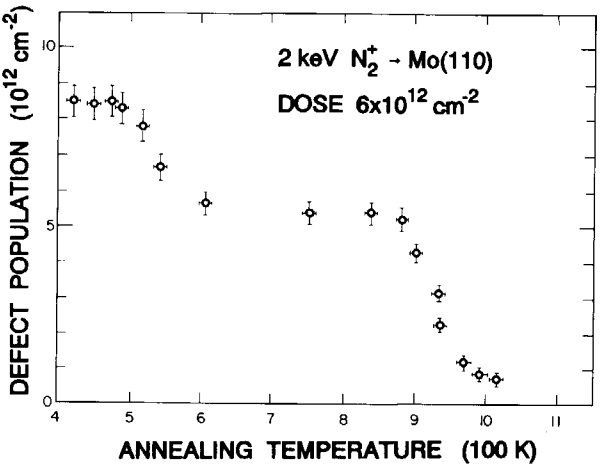

Fig. 4.5. The recovery of vacancy type defects in a nitrogen bombarded molybdenum single crystal, as obtained by Van Veen and Caspers[17].

In the THDS experiments carried out by Van Veen and Caspers helium was used as a probe, to give the results shown in fig. 4.5. The defect population is obtained from the number of helium atoms trapped at the defects that are left in the system after the appropriate anneal (see section 2.4). Clearly there are two main stages of defect disappearance: the first, between 500 K and 600 K corresponds to the so-called stage III recovery in molybdenum and is due to vacancy annealing; the second, between 900 K and 1000 K, which corresponds to an activation energy of (2.55 ± 0.05) eV, is the stage attributed to the reaction NV → N + V in which substitutional nitrogen goes

back into solution.

To preclude all doubts that the defects investigated by Van Veen and Caspers are indeed substitutional nitrogen atoms, a molybdenum specimed has been prepared which only contained the suspected NV defects. These were produced by a low dose ($1.8x10^{12}$ cm^{-2}) 3 keV implant plus an anneal to 900 K. The initial defect structure was then probed with 150 eV helium ions followed by helium desorption. Repeating the whole procedure, starting each time with the manufacture of the suspected NV defects, but with successively larger doses of 150 eV He ions, has produced the THDS spectra shown in fig. 4.6.

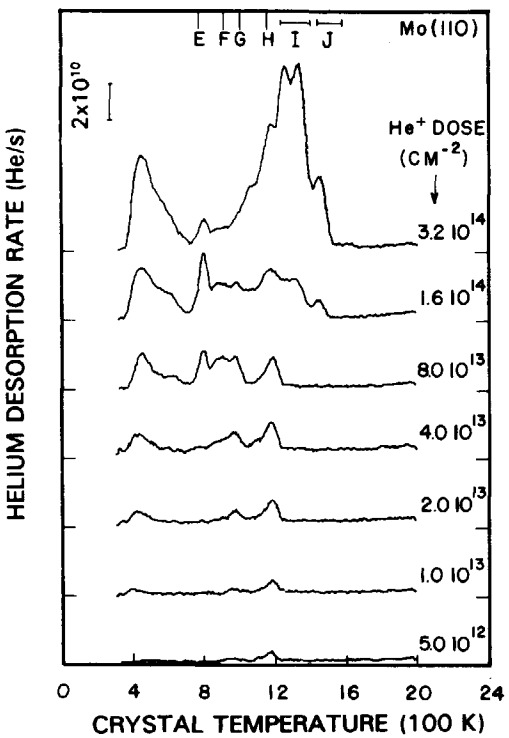

Fig. 4.6. Helium desorption spectra from a Mo(110) single crystal which has been irradiated with $1.8x10^{12}$ cm^{-2} 3 keV N, annealed up to 900 K, and irradiated with various doses of 150 eV He.

The evolution of the peaks, beginning with the H peak at low doses and then the growth of the peaks G, F and E at lower temperatures (*i.e.* weaker helium binding) followed by peaks at higher temperatures (higher helium binding), is exactly that found when the initial defects structure consists of monovacancies without nitrogen. It has already been remarked that the peaks E, F, G and H have been shown previously to represent the amount of helium

released from respectively $He_{6-9}V$ (a complex of n helium atoms in a vacancy, with $5 \leq n \leq 9$), $He_{3-4}V$, He_2V and HeV defects (see section 2.4). This strongly suggests that the initial defect must have a monovacancy character. Since a monovacancy itself cannot survive the anneal at 900 K the initial defect has to be a vacancy filled with one ore more nitrogen atoms. The latter can be excluded on the simple basis that the number of injected nitrogen atoms is not sufficient to fill all the vacancies with more than one nitrogen atom. Hence the defects must be NVs.

The peaks developing above the H peak at higher helium dose confirm the monovacancy character deduced already, since this behaviour is characteristic of the addition of helium to monovacancies in molybdenum. As a tenth helium atom arrives at a He_9V defect, the so-called trap mutation process is activated (see section 1.2.2) in which a self-interstitial is created to leave a divacancy with 10 helium atoms $(He_{10}V_2)$[27]. The helium is bound more strongly to a V_2 defect than to a monovacancy and this is reflected in the higher release temperature of the desorbed helium. Further trap mutation can take place to give larger He-V clusters and further release peaks.

4.4.4 Reduction of suspected NV defects by self-interstitials

In this section the influence of self-interstitials on the suspected NV defects is examined, by using the self-interstitial production technique described in section 3.2.

Whether the reaction NV + I → N, where N denotes an interstitial nitrogen atom, is expected to take place depends on the formation energy of the defects involved. The reaction will only occur if

$$E^F_{NV} + E^F_I \geq E^F_N, \tag{4.10}$$

where E^F_X is the formation energy of defect X. In section 1.2.3 it has already been shown that this is indeed the case.

As in section 4.4.3, the starting point of the procedure in each experimental run was the creation of NV defects in a Mo(110) specimen by N^+ irradiation and a 900 K anneal. Following this, the specimen was bombarded with a dose of 150 eV Ar^+ ions to create self-interstitials according to the method described in section 3.2. Variation of the Ar dose and subsequent probing by a constant helium dose should reflect any changes in the NV population due to the reaction NV + I → N. To minimize the effect of argon and vacancies in the surface layers, the specimen was annealed to 800 K after the argon bombardment but before probing with helium[28].

The results of the procedure are shown in fig. 4.7 as a function of argon dose. Concentrating on the H peak it is quite clear that the NV defect

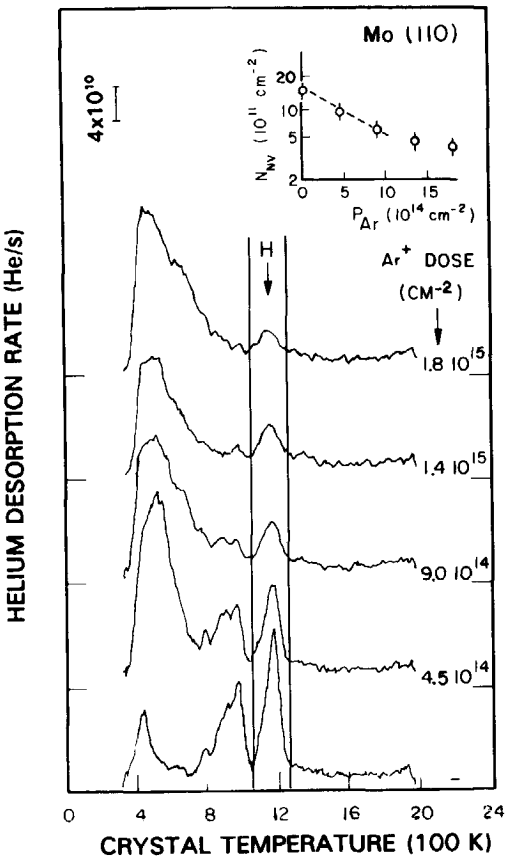

Fig. 4.7. Helium desorption spectra from a Mo(110) single crystal which has been irradiated with 1.8×10^{12} cm^{-2} 3 keV N, annealed up to 900 K, bombarded with 150 eV Ar, annealed up to 800 K, and irradiated with 5.0×10^{13} cm^{-2} He. The inset shows the number of NV defects N_{NV} as a function of argon dose P_{Ar}.

population is being reduced by the self-interstitials formed by the argon bombardment. Hence, the reaction NV + I → N is indeed taking place. Below an argon dose P_{Ar} of 1×10^{15} cm^{-2}, the NV population N_{NV} can be described by the equation

$$\frac{dN_{NV}}{dP_{Ar}} = -\mu N_{NV}, \tag{4.11}$$

where the capture coefficient μ depends on the self-interstitial yield per argon ion (≈ 0.025) and the capture probability of the self-interstitials by the defects (see also section 3.2). The capture coefficient μ as derived from the inset in

fig. 4.7 equals $(1.0 \pm 0.5) \times 10^{-15}$ cm^2.

At argon doses above 1×10^{15} cm^{-2} the reduction of the defects takes place less rapidly. This is attributed to the fact that during the reduction of NV defects interstitial nitrogen is formed which may act as an unsaturable trap for self-interstitials[29]. An additional reason might be the increased subsurface damage which causes a reduced yield of self-interstitials per argon ion.

The reduction behaviour reported here is similar to that of HeV and ArV defects, for which values of μ of respectively $\sim 7 \times 10^{-16}$ cm^2 and $\sim 1 \times 10^{-15}$ cm^2 have been measured[30]. The fact that the defects that are stable up to 900 K can be reduced by self-interstitials, and that the reduction behaviour is similar to that of monovacancies filled with helium and argon, confirms the NV assignment proposed previously.

4.4.5 Theoretical considerations

In section 4.4.3 it was noted that the thermal desorption of helium from the NV defects is identical to that of helium from monovacancies. This strongly suggests that the nitrogen dissociates from He_nNV complexes before the least bound helium atom is released. It is possible to check theoretically that this should happen by considering the definition of binding energy and applying the results to the present system. As far as HeNV complexes are concerned, we are primarily interested in $E^{D,He}_{HeNV}$ and $E^{D,N}_{HeNV}$. By using the definition of binding energy, see section 1.2.3, it can be derived that

$$E^{B,N}_{HeNV} - E^{B,He}_{HeNV} = E^{B,N}_{NV} - E^{B,He}_{HeV}. \tag{4.12}$$

Since by definition the dissociation energy $E^{D,X}_{XY}$ equals the sum of the binding energy $E^{B,X}_{XY}$ and the migration energy E^{M}_{X}, the addition of $E^{M}_{N} - E^{M}_{He}$ to both sides of equation 4.12 results in

$$E^{D,N}_{HeNV} - E^{D,He}_{HeNV} = E^{D,N}_{NV} - E^{D,He}_{HeV}. \tag{4.13}$$

By substituting the value of 2.55 eV for $E^{D,N}_{NV}$ (*i.e.* the value reported by Van Veen and Caspers) and 3.8 eV for $E^{D,He}_{HeV}$ (see table 4.1), equation 4.13 reads:

$$E^{D,N}_{HeNV} = E^{D,He}_{HeNV} - 1.25 \text{ eV}. \tag{4.14}$$

Thus it can be deduced that in the THDS experiments nitrogen leaves HeNV complexes before the helium is released.

A similar result follows for He_2NV and He_3NV defects, when using the experimental values $E^{D,He}_{He_2V} = 2.9$ eV, $E^{D,He}_{He_3V} = 2.6$ eV (see table 4.1), and when

Table 4.1. The temperatures at which defect reactions take place in THDS experiments on nitrogen in molybdenum, as proposed in this work. The temperatures at which relevant helium dissociation reactions occur are also given. For the denotation the reader is referred to the paragraphs and references in which the various processes are mentioned. The temperatures are given for an annealing rate of 40 K/s.

T (K)	Peak label	Reaction	Section or ref.
<300		Helium becomes mobile ($E_{He}^{M}=0.17$ eV)	8
		$He+He_nV \rightarrow He_{n+1}V$ for $n \leq 8$	27
		$He+He_nV \rightarrow He_{n+1}V_2I$ for $n>8$	27
		$NV+I \rightarrow N$	4.4.4
300-600		Release of He bound to (sub)surface positions	27
~500		Nitrogen becomes mobile ($E_N^M=1.2$ eV)	18
~550		Vacancies become mobile ($E_V^M=1.23\pm0.04$ eV)	4.2.4
<590		Hydrogen becomes mobile ($E_H^M<1.4$ eV)	4.3.3
650-960		$NV_2 \rightarrow NV+V$ ($1.6\text{ eV} \leq E_{NV_2}^{D,V} \leq 2.7$ eV)	4.5.4
700-1000		$NV_3 \rightarrow NV_2+V$ ($1.9\text{ eV} \leq E_{NV_3}^{D,V} \leq 3.0$ eV)	4.5.4
~790	E	$He_nV \rightarrow He_4V+(n-4)He$, $5 \leq n \leq 9$ ($E_{He_nV}^{D,He}=2.1\pm0.1$ eV)	27
~870	F_1	$He_4V \rightarrow He_3V+He$ ($E_{He_4V}^{D,He}=2.4\pm0.1$ eV)	27
~900		$NV \rightarrow N+V$ ($E_{NV}^{D,N}=2.55\pm0.05$ eV)	4.4.3,17
<910		$He_3NV \rightarrow He_3V+N$	4.4.5
~910	F_2	$He_3V \rightarrow He_2V+He$ ($E_{He_3V}^{D,He}=2.6\pm0.1$ eV)	27
<970		$He_2NV \rightarrow He_2V+N$	4.4.5
~970	G	$He_2V \rightarrow HeV+He$ ($E_{He_2V}^{D,He}=2.9\pm0.1$ eV)	27
~1100		Dissociation of N_mV_k clusters, $m \geq 2$ and $k=2,3$ or $m \geq 1$ and $k=4,5$, or $m \geq 0$ and $k \geq 6$	4.5.4
<1170		$HeNV \rightarrow HeV+N$	4.4.5
~1170	H	$HeV \rightarrow He+V$ ($E_{HeV}^{D,He}=3.8\pm0.2$ eV)	27
1200-1500	I,J	He dissociates from He_nV_k, after the release of nitrogen from $He_nN_mV_k$ complexes, $n \geq 1, m \geq 1, k \geq 2$	4.5.4

we assume that

$$E_{He_2NV}^{D,N} \leq E_{HeNV}^{D,N} \leq E_{NV}^{D,N}; \tag{4.15}$$

the latter is plausible because in an He_2NV defect there is less space for a nitrogen atom than in an HeNV or NV defect.

Thus, for $n \leq 3$ the assumption made in the previous work concerning the dissociation order for He_nNV defects is found to be consistent with the

experimentally found value for $E_{NV}^{D,N}$. For $n \geq 4$ this cannot be deduced, but considering the previously obtained experimental results a similar behaviour is envisaged.

4.5 The interaction between vacancy clusters and nitrogen in molybdenum

4.5.1 Introduction

In section 4.4 it has been shown that nitrogen may stabilize monovacancies in molybdenum. The purpose of this section is to show that also small vacancy clusters are stabilized by nitrogen. Section 4.5.2 presents some positron annihilation results on the interaction between nitrogen and vacancy clusters, and sections 4.5.3 and 4.5.4 are alotted to the production and the nature of small nitrogen-vacancy-clusters that are resistant to an anneal at 1005 K.

4.5.2 Positron annihilation results

It has been observed in fig. 4.4 that in the molybdenum sample where only vacancies were present, clustering of the vacancies occurred in the temperature interval from 480 to 570 K. In the nitrogen doped samples no increase in the positron lifetime τ_2 could be perceived at this temperature interval, which was caused by the fact that the presence of nitrogen totally suppressed the free migration and the clustering of vacancies. Around 920 K however, fig. 4.4 shows a very strong increase in the lifetime τ_2 for the nitrogen doped samples, indicating that at this stage clusters are formed. The lifetime in these clusters is significantly higher than the lifetime in voids in the pure sample. Since this cannot be ascribed to a size effect[31], it must be due to nitrogen in the clusters. This is in agreement with the observation of elongated lifetimes in voids caused by diffusion of nitrogen into the voids[32].

4.5.3 The production of defect clusters that survive a 1005 K anneal

In this section we focus on thermal helium desorption experiments on clusters of defects in molybdenum, created by 3 keV N^+ irradiation and subsequent thermal annealing. The N^+ doses applied are higher than those in section 4.4 in order to create enough defects to form (small) clusters. In all the experiments discussed below, the defect structure has been probed with 5.0×10^{13} cm^{-2} 150 eV He^+.

Fig. 4.8 shows the desorption of helium from defects created by different doses of 3 keV N^+ irradiation followed each time by an anneal up to 1005 K to exceed the temperature at which NV defects dissociate. It is likely that NV

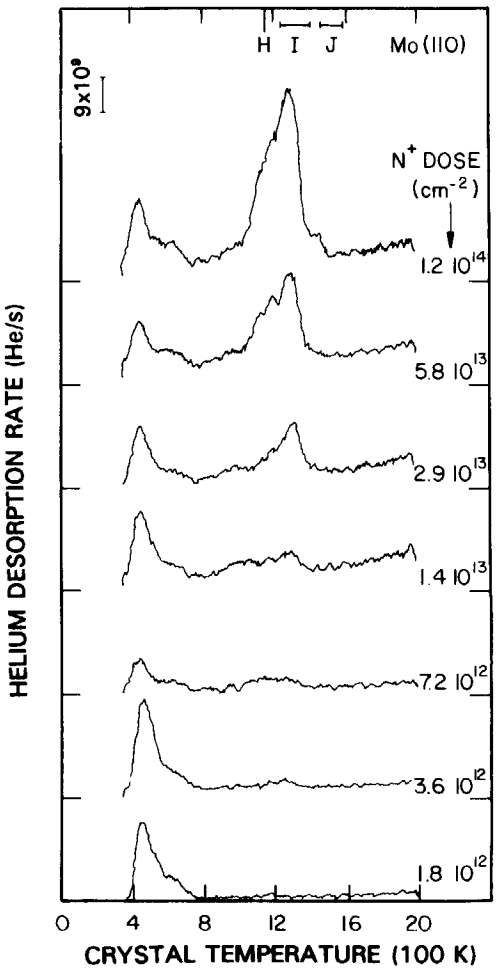

Fig. 4.8. Helium desorption spectra obtained after irradiating a Mo(110) single crystal with 3 keV N, annealing up to 1005 K, and irradiating with 5.0×10^{13} cm^{-2} 150 eV He.

defects that break up at ~950 K form new complexes of one or more nitrogen atoms and vacancies. When decorated with small amounts of helium, helium release is expected to occur either around the temperature where the reaction $HeV \rightarrow He + V$ occurs (1170 K), or at higher temperatures. The first is the case when vacancies and nitrogen dissociate from the defect cluster before helium is released from the last remaining vacancy, *e.g.* in the following sequence for a $HeNV_2$:

$$
\begin{aligned}
HeNV_2 &\rightarrow HeNV + V \quad (T<1170\ K),\\
HeNV &\rightarrow HeV + N,\\
HeV &\rightarrow He + V \quad (T\approx 1170\ K: H\ peak).
\end{aligned}
\tag{4.16}
$$

The latter is the case when both helium and vacancies are relatively strongly bound to the defect complex, *e.g.*:

$$
\begin{aligned}
HeN_nV_m &\rightarrow HeN_nV_{m-1} + V \quad (T>1170\ K)\\
HeN_nV_{m-1} &\rightarrow HeN_{n-1}V_{m-1} + N\\
\ldots &\rightarrow \ldots\\
HeNV &\rightarrow HeV + N\\
HeV &\rightarrow He + V \quad (T>1170\ K).
\end{aligned}
\tag{4.17}
$$

It can be seen in fig. 4.8 that despite the anneal up to 1005 K there are still defects present which, as expected, release helium at 1170 K (the peaks marked I and J). It is noteworthy that the peaks marked I and J also have been observed in experiments where helium filled vacancy clusters had been created by 1 keV helium irradiation, and where no nitrogen was involved[33]. This indicates that in the present experiments nitrogen is released before the helium.

To investigate until what anneal temperature the defects that survive the 1005 K anneal are present in the molybdenum crystal, we have varied the annealing temperature. Fig. 4.9 shows the helium desorption behaviour after irradiating the crystal with 4.5×10^{13} cm^{-2} 3 keV N^+ and annealing up to temperature T_A. It can be seen that, as found earlier, the NV defects that cause the E, F, G and H peaks disappear beyond $T_A\approx 950$ K, and that the defects that survive the 1005 K anneal disappear at $T_A\approx 1100$ K.

For three annealing temperatures the nitrogen irradiation dose has been varied to monitor the growth of the defect population. The result is shown in fig. 4.10 where the total number of desorbed helium atoms, which equals the number of trapped helium atoms, is shown as a function of nitrogen irradiation dose (helium desorbing below 600 K is not taken into account, since this is related to surface traps). The number of defects N_D can be calculated from the number of trapped helium atoms N_{He} by applying the trapping model described by Van Veen *et al.*[34]. This yields:

$$
zN_D = 1.4\times10^{13}\,(\Theta P_{He}/N_{He}-1)^{-1}\ cm^{-2}; \tag{4.18}
$$

where z is a constant proportional to the sink strength of a trap for helium (*e.g.* for V z equals 1, for V_8 z equals 2), Θ denotes the fraction of the helium irradiation dose entering the crystal (for 150 eV He^+ $\Theta=0.5$), and P_{He} is the helium irradiation dose (cm^{-2}).

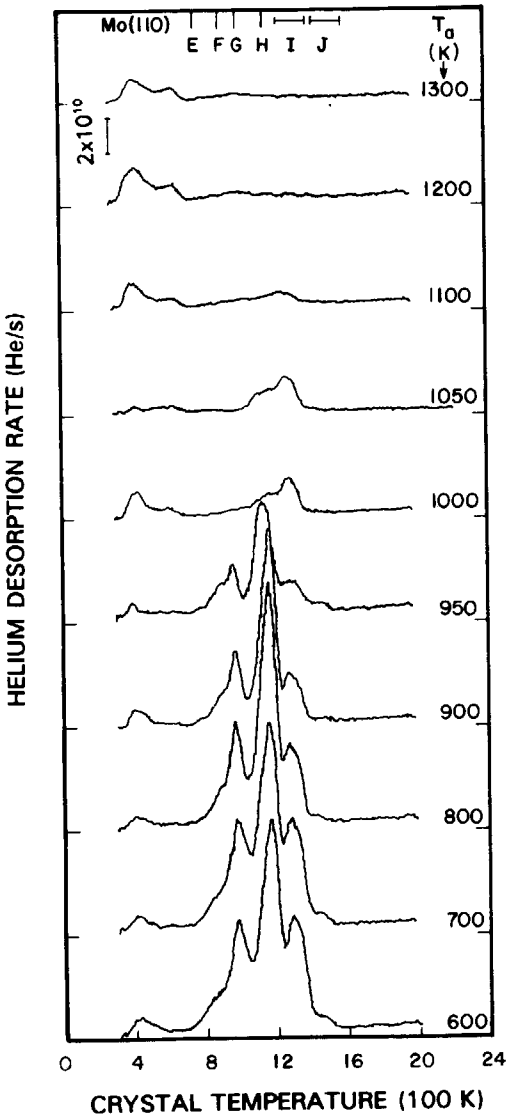

Fig. 4.9. Helium desorption spectra from a Mo(110) single crystal which has been irradiated with 4.5×10^{13} cm^{-2} 3 keV N, annealed up to temperature T_a, and irradiated with 5.0×10^{13} cm^{-2} 150 eV He.

The values of zN_D corresponding to the values of N_{He} are shown on the right axis in fig. 4.10. It can be observed in the data from the $T_A = 300$ K experiment (*i.e.* without annealing) that when the N^+ dose P_N increases from 1.8×10^{12} cm^{-2} to 1.2×10^{14} cm^{-2} the defect production decreases from 2.6 to 0.3 defects per N^+ ion, if it is assumed that $z = 1$ (no anneal, mainly

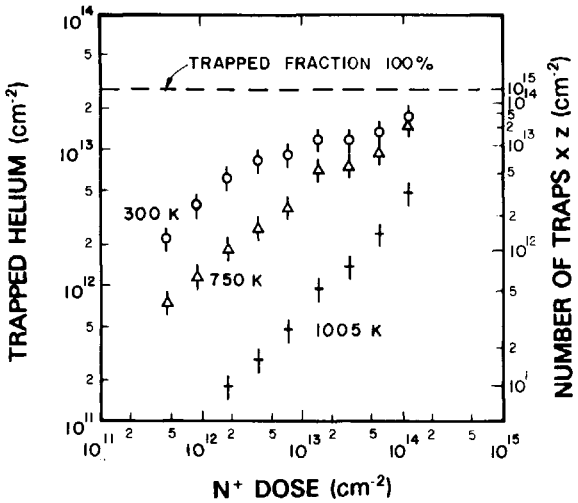

Fig. 4.10. Total number of helium atoms trapped by defects as a function of nitrogen irradiation dose after: (+) a 3 keV N irradiation followed by an anneal up to 1005 K and probing with $5x10^{13}$ cm^{-2} 150 eV He; ( ) a similar experiment with an annealing step up to 750 K after the nitrogen irradiation; (o) a similar experiment without an annealing step. The corresponding number of defects multiplied by the sink strength z per defect is given on the right axis. The dashed line indicates where the amount of trapped helium equals the amount of helium that has entered the crystal.

monovacancies). This is attributed to a combination of (a) the fact that at higher damage level more recombination takes place between vacancies and self-interstitials and hence relatively less damage is created, and (b) the fact that at higher damage level clustering is more likely to occur, thus decreasing the total number of trapping sites.

When it is assumed that $z = 1.6$ in the 1005 K anneal case (all Vs and NVs have disappeared, only small clusters are left), it can be deduced that 1% of the defects survives the 1005 K anneal when $P_N = 1.2x10^{12}$ cm^{-2} and 6% when $P_N = 1.2x10^{14}$ cm^{-2}. Thus, with increasing N^+ dose more defects are produced that survive an anneal at 1005 K.

4.5.4 Nature of defect clusters that survive a 1005 K anneal

The fact that the helium binding to defects that survive the 1005 K anneal is stronger than to monovacancies or NVs, suggests that the defects contain more than one vacancy. The similarity of the desorption peaks I and J to the peaks produced by simple trap mutation, fig. 4.6, is also clear. (Note that the probe helium dose was too small to have made such He_nV_2 defects by the trap

mutation process mentioned in section 4.4.3). Since V, V_2, V_3, V_4 and V_6 defects are already mobile or dissociate below 1005 K[7], it is reasonable to assume that the defects that survive the 1005 K anneal either contain nitrogen or are larger than V_6.
The purpose of this section is to obtain more information about the composition of the defects.

(a) NV

The defects are not NV defects since it has been demonstrated that NVs dissociate between 900 K and 1000 K.

(b) NV_2 and NV_3

These defects can be excluded by using the theoretical approach of section 4.4.5. For NV_2s it can be derived that

$$E^{D,N}_{NV_2} - E^{D,V}_{NV_2} = E^{D,N}_{NV} - E^{D,V}_{V_2} = 2.55^{17} - 1.6^{9} = 0.95 \text{ eV}, \qquad (4.19)$$

and thus during a thermal ramp annealing a vacancy leaves an NV_2 complex before the nitrogen atom does so. Since no vacancy type trap can be as deep as the surface, $E^{D,N}_{NV_2}$ must be smaller than the energy that is required to bring a nitrogen atom from the surface into the bulk, *i.e.* 3.65 eV[18]. Substitution of this value in eq. 4.19 yields $E^{D,V}_{NV_2} \leq 2.7$ eV. It can also be derived from equation 4.13 that $E^{D,V}_{NV_2} \geq E^{D,V}_{V_2} = 1.6$ eV if one assumes that $E^{D,N}_{NV_2} \geq E^{D,N}_{NV}$ (a V_2 is a deeper trap for nitrogen than a V).

Thus we have found that 1.6 eV $\leq E^{D,V}_{NV_2} \leq$ 2.7 eV. Since in the THDS experiments 2.7 eV corresponds to 960 K for a first order desorption process[35] it can be concluded that the defects that survive the anneal at 1005 K are not NV_2s, because these would have been dissociated below 960 K. In a similar way it can be derived that the defects are not NV_3s.

These arguments are supported by an experiment similar to that used on the NV defects in section 4.4.4, where argon bombardment induced self-interstitials were shown to reduce the NV defects by vacancy-interstitial recombination. By starting with the defects under investigation (bombardment with 4.5×10^{13} cm^{-2} 3 keV N^+ and a subsequent anneal to 1040 K) followed by different amounts of 150 eV Ar^+ bombardment, any NV_2s or NV_3s present ought to have been reduced: $NV_m + I \rightarrow NV_{m-1}$. However, only very little reduction of the I peak was found on subsequent probing with 5.0×10^{13} cm^{-2} 150 eV helium, suggesting that the defects are not just NV_2s or NV_3s.

(c) N_2V_2 and N_2V_3

The experimental result just mentioned is relevant to the question whether the defects might be N_2V_2 or N_2V_3 defects. It is plausible that the presence of two nitrogen atoms in the di- or trivacancy will prevent the V-I recombination. If so, then N_2V_2 and N_2V_3 defects become the strongest candidates for the unknown defects. The near coincidence of the desorption peak of fig. 4.8 with the peak produced after trap mutation (fig. 4.6) certainly suggests a divacancy character.

(d) Larger clusters

It cannot be excluded that the defects that survive annealing beyond 1005 K are clusters consisting of more than three vacancies that are reduced to smaller defects during the final ramp annealing similar to the reactions 4.16 and 4.17.

Considering these arguments leads to the conclusion that, although the exact defect or mix of defects that survive the 1005 K anneal may not be precisely defined, there is no doubt that we are dealing with (a) a vacancy defect cluster consisting of two or three vacancies and at least two nitrogen atoms, or (b) a cluster of four or five vacancies and at least one nitrogen atom, or (c) an N_mV_k defect with $m \geq 0$, $k \geq 6$.

The important point is that the results show very clearly that small vacancy clusters of the same size but without added nitrogen, are far less thermally stable and will dissociate at lower temperatures. Such information should be useful for theories of void nucleation, where trapped gas atoms can both make potential nuclei thermally stable and also ensure that subsequent cluster growth is three-dimensional (voids) rather than two-dimensional (vacancy loops)[36].

4.6 Conclusions

The employment of novel experimental methods and theoretical considerations in characterizing vacancy type defects in fusion reactor materials has been demonstrated. The THDS method has been shown to be useful in measuring vacancy migration energies. The vacancy migration energy in Mo was found to be (1.23 ± 0.04) eV. This value could be derived without assuming any sink strength for mobile vacancies. The only quantities in the analysis which could not be measured were the parameters characterizing the initial vacancy depth distribution, but the obtained result proved to be relatively insensitive to variations in this parameter.

The results of an attempt to measure the dissociation energy of a hydrogen

atom bound to a vacancy showed that this dissociation energy is less than 1.4 eV.

By using novel defect assignment methods and theoretical considerations it has more strongly been established that the detrapping of nitrogen from a single vacancy in molybdenum requires an activation energy of (2.55 ± 0.05) eV. The in this work proposed temperatures at which defect reactions take place in nitrogen irradiated molybdenum are summarized in table 4.1. The main influence of nitrogen on vacancies in molybdenum is that it enhances the vacancy survival probability after production and that it strongly promotes the thermal stability of the defects. This implies that the presence of nitrogen plays an important role in controlling void nucleation and growth. The fact that nitrogen immobilizes vacancies up to high temperatures means that above the vacancy migration temperature a high concentration of relatively small voids will be formed and that the formation of larger voids will occur less readily.

Small nitrogen-vacancy clusters have been observed that are stable up to an annealing temperature of 1100 K. The mutual binding was found to immobilize both the nitrogen and the vacancies. In the case of helium-nitrogen-vacancy complexes it has been inferred that upon annealing the nitrogen generally leaves the complexes before the helium is released.

References chapter 4

1. I.A. Schwirtlich and H. Schultz, Phil. Mag. A **42** (1980) 601.
2. K. Maier, M. Peo, B. Saile, H.E. Schaefer and A. Seeger, Phil. Mag. A **40** (1980) 701.
3. W.Th.M. Buters and A. van den Beukel, J. Nucl. Mater. **137** (1985) 51.
4. M.T. Robinson and I. Torrens, Phys. Rev. B **9** (1974) 5008.
5. NAG library routine D03PGF.
6. K. Maier, H. Mehrer and G. Rein, Z. Metallk. **70** (1979) 271.
7. A. Seeger and H. Mehrer, in: Proc. Int. Conf. on Vacancies and Interstitials in Metals, eds. A. Seeger, D. Schumacher, W. Schilling and J. Diehl (North-Holland, Amsterdam, 1969), p. 1.
8. A. van Veen, Materials Science Forum **15-18** (1987) 3.
9. R.H.J. Fastenau, A. van Veen, P. Penning, L.M. Caspers, Phys. Stat. Sol. (a) **47** (1978) 577.
10. M. Hou, A. van Veen, L.M. Caspers and M.R. Ypma, Nucl. Instr. and Meth. **209/210** (1983) 19.
11. M. Mahning and L.D. Schmidt, Z. Phys. Chem., N.F., **80** (1971) 71.
12. S.M. Myers and F. Besenbacher, J. Appl. Phys. **60** (1986) 3499.
13. H.E. Hansen, R. Talja, H. Rajainmäki, H.K. Nielsen, B. Nielsen and R.M. Nieminen, Appl. Phys. A **36** (1985) 81.
14. B.L. Doyle and D.K. Brice, J. Nucl. Mater. **122-123** (1984) 1523.
15. S. Linderoth, H. Rajainmäki, B. Nielsen, H.E. Hansen, R.M. Nieminen and K. Petersen, Mater. Sci. Forum **15-18** (1987) 751.

16. H. Eleveld and A. van Veen, to be published in J. Nucl. Mater.
17. A. van Veen and L.M. Caspers, Solid State Comm. **30** (1979) 761.
18. J.H. Evans and B.L. Eyre, Acta Met. **17** (1969) 1109.
19. See *e.g.* A. Seeger, Appl. Phys. **4** (1974) 183.
20. R.M. Walker, Radiation Damage in Solids, ed. B.S. Billington, Academic Press (1962) 594.
21. R.M. Nieminen and I. Laakkonen, Appl. Phys. **20** (1979) 181.
22. J.H. Evans, B.L. Eyre and H.K. Birnbaum, Acta Met. **18** (1970) 835.
23. P. Hautojärvi, J. Johansson, A. Vehanen, U. Yli-Kauppile and P. Moser, Phys. Rev. Lett. **44** (1980) 1326.
24. A. Anttila and J. Hirvonen, Appl. Phys. Lett. **33** (1978) 394.
25. M. Hautala, A. Anttila and J. Hirvonen, J. Nucl. Mater. **105** (1982) 172.
26. F. Reiter, in: Proc. 9th Symp. on Fusion Technology (Pergamon, Oxford, 1976) p. 57.
27. A. van Veen, J.H. Evans, W.Th.M. Buters and L.M. Caspers, Rad. Eff. **78** (1983) 53.
28. A. van Veen, W.Th.M. Buters, G.J. van der Kolk, L.M. Caspers and T.R. Armstrong, Nucl. Instr. and Meth. **194** (1982) 485.
29. J.H. Evans, Acta Met. **18** (1970) 499.
30. A. van Veen, W.Th.M. Buters, T.R. Armstrong, B. Nielsen, K.T. Westerduin and L.M. Caspers, Nucl. Instr. and Meth. **209&210** (1983) 1055.
31. N. Thrane, K. Petersen and J.H. Evans, Appl. Phys. **12** (1977) 187.
32. H.E. Hansen, B. Nielsen, G. Trumpy and K. Petersen, in: Positron Annihilation, eds. P.G. Coleman, S.C. Sharma, L.M. Diana (North Holland, Amsterdam, 1982) p. 438.
33. A. van Veen and L.M. Caspers, in: Proc. 7th Int. Vac. Congress and 3rd Int. Conf. on Solid Surfaces (Vienna, 1977) p. 2637.
34. A. van Veen and L.M. Caspers, in: Proc. Consultants Symp. on Inert Gases in Metals (AERE Report 9733, Harwell, 1980) p. 494.
35. A. van Veen, A. Warnaar and L.M. Caspers, Vacuum **30** (1980) 109.
36. N. Igata, Y. Kohno, N. Tanabe, F. Rotman and H. Tsunakawa, J. Nucl. Mater. **122** (1984) 219.

Chapter 5
The interaction between hydrogen and voids in tungsten

5.1. Introduction

Vacancy clusters and voids constitute one of the major factors that determine the hydrogen isotope permeation and the hydrogen isotope inventory in fusion reactor materials. The first desorption measurements that yielded evidence of hydrogen and deuterium trapping in vacancy type defects in molybdenum and tungsten were reported by Erents and McCracken[1,2]. Data on the dissociation energy of hydrogen from vacancy and void type defects have later been compiled by Myers *et al.*[3], Fukai and Sugimoto[4], Besenbacher *et al.*[5] and Picreaux[6]. They employed ion beam analysis to detect changes in hydrogen profiles during thermal annealing and from the obtained data the activation energies of hydrogen detrapping were derived. Nielsen *et al.*[7,8] and Hansen *et al.*[9] used the positron lifetime technique to monitor the effects of implanted or electrochemically dissolved hydrogen on vacancies and voids in molybdenum. The hydrogen was observed to decrease the positron lifetime in voids and to increase the trapping rate. Hydrogen release occurred in two separate anneal stages, one attributed to the release of hydrogen present as molecules in a void, and one attributed to the release of atomic hydrogen bound to the inner surface of a void. The positron lifetime technique has been employed similarly by Van Veen *et al.*[10] to study hydrogen in tungsten. Tanabe *et al.*[11] have performed deuterium permeation experiments on molybdenum and nickel, and reported a strong decrease in permeation caused by the presence of defect clusters. The influence of hydrogen on the nucleation and growth of voids has been discussed and modelled by Murphy[12,13] for stainless steel. Direct monitoring of the hydrogen release from metals during annealing has not been reported by many authors.

In this chapter results are presented from thermal desorption and positron annihilation experiments on the interaction between hydrogen and voids in tungsten. In these experiments, use was made of samples containing a well characterized void population uniformly distributed throughout the sample. To account for the obtained results, a theoretical model has been developed, which describes the interaction between hydrogen and voids in metals in terms of the chemical potential. This model is presented in section 5.2. In section 5.3 the thermal desorption and positron annihilation experiments are described, and it is demonstrated how the model can be applied to interpret experimental results.

5.2 Theoretical model for the hydrogen-void interaction

5.2.1 The metal-hydrogen system

In order to gain more insight into the interaction between hydrogen and voids in tungsten, it is useful to consider the various energy levels that hydrogen can occupy in tungsten. In fig. 5.1 a potential energy diagram of the hydrogen-tungsten system is shown. Definitions and literature values of the heat of solution, the surface adsorption energy, migration energy and binding and dissociation energies of hydrogen at a void follow from the figure and the caption. It is assumed that no external pressures are present, which justifies the use of the term energy instead of enthalpy in the nomenclature.

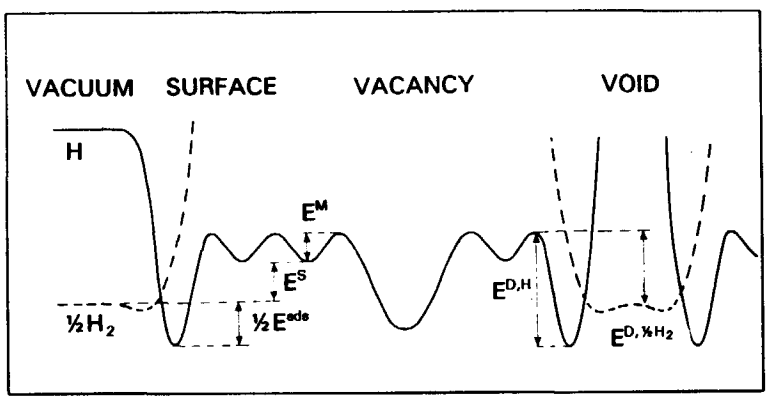

Fig. 5.1. Energy diagram of the system hydrogen-tungsten. Literature values for the indicated energies are: surface chemisorption energy $\frac{1}{2}E^{ads} = 0.4\text{-}0.7$ eV[14], migration energy $E^M = 0.40$ eV[29], heat of solution $E^S = 1.04$ eV[29]. The dissociation energy of $\frac{1}{2}H_2$ from a void $E^{D,\frac{1}{2}H_2} = E^S + E^M = 1.44$ eV. The dissociation energy of a chemisorbed hydrogen atom in a void $E^{D,H} = \frac{1}{2}E^{ads} + E^S + E^M = 1.8\text{-}2.1$ eV.

Note that inside a large void adsorbed states may exist that are similar to those at a surface and that the dissociation energy required to release a hydrogen atom bound to the inner surface of a void can be approximated by

$$E^{D,H} = \tfrac{1}{2}E^{ads} + E_H^S + E_H^M, \tag{5.1}$$

where $\frac{1}{2}E^{ads}$ is the chemisorption energy of a hydrogen atom adsorbed at the surface[14], and E_H^S and E_H^M are the energies of solution and migration.

During the implantation of hydrogen into a metal, a stationary concentration c_H of interstitial hydrogen will be established below the sample surface after

some time. The value of c_H can be calculated by using hydrogen permeation models developed by Doyle[15], Waelbroeck *et al.*[16], and Pick and Sonnenberg[17]. The important parameters are: the flux of H_2 ions J, the average penetration depth of the implanted ions L, the hydrogen diffusivity D, and the recombination rate k_r at which hydrogen atoms at the surface associate to molecules before desorption. If it is assumed that hydrogen recombination at the surface occurs instantaneously, the stationary concentration of interstitial hydrogen c_H present below the sample surface during the implantation can be estimated by (see equation 1.6)

$$c_H = \frac{2\Theta JL}{DN_0}; \tag{5.2}$$

where Θ is the probability that the ions penetrate into the sample and N_0 denotes the atomic density of tungsten. c_H is expressed in atomic fraction.

The amount of hydrogen trapped in voids can be found[18] by solving the time dependent diffusion equation for interstitial hydrogen (see equation 1.2):

$$\frac{\partial c_H(x,t)}{\partial t} = D\frac{\partial^2 c_H(x,t)}{\partial x^2} + I(x) - 4\pi r_V N_0 D c_V [c_H(x,t) - c_{H,eq}(N_H,x,t)]. \tag{5.3}$$

The equation contains the implantation depth distribution I(x), a sink term which accounts for the trapping rate at voids: $-Kc_H(x,t)c_V$, and a source term which accounts for the detrapping rate from voids: $Kc_{H,eq}(N_H,x,t)c_V$; c_V is the void concentration, $c_{H,eq}$ is the interstitial hydrogen concentration in thermal equilibrium with the hydrogen in the void, N_H is the average number of hydrogen atoms per void, and[18] $K = 4\pi r_V N_0 D$ is a factor accounting for the effective geometrical trap size with r_V the void radius and N_0 the atomic density of the host material.

Schilling[19] has shown that it is possible to account for the repeated trapping and detrapping during diffusion in a simple way by defining an effective diffusivity D_{eff}. This effective diffusivity equals the diffusivity D times the fraction of hydrogen that contributes to the diffusion:

$$D_{eff} = D\frac{c_H}{c_H + c_V N_H}, \tag{5.4}$$

where $c_V N_H$ is the concentration of hydrogen trapped in voids, expressed in atomic fraction. In the experiments discussed in the next section the amount of interstitial hydrogen is much less than the amount of hydrogen trapped in voids, *i.e.* $c_H \ll c_V N_H$.

5.2.2 Void saturation

When hydrogen atoms can not escape from a void, as is the case at low temperatures, the hydrogen pressure in a void can rise to such an extent that the volume of the void is increased by punching out loops of self-interstitials[20]. Due to the volume increase, the pressure decreases and more hydrogen can be accomodated in the void. The loop-punching process can occur repeatedly, and when this happens the voids are considered to be unsaturable traps for hydrogen.

If a loop-punching process does not take place, a local diffusive equilibrium will be established between hydrogen inside and outside a void, *i.e.* the net flux of particles into the void will be zero after some time. The detrapping rate will then be equal to the trapping rate (which implies that $c_{H,eq} = c_H$) and the void will be saturated with hydrogen. If it is assumed that voids must be saturated with hydrogen before hydrogen can reach larger depths, then the amount of hydrogen trapped in voids per unit surface area is given by

$$n_{trapped} = c_v N_H N_0 x_s(t) , \tag{5.5}$$

where $x_s(t)$ is the effective depth to which the voids are saturated with hydrogen. On the other hand the total amount of hydrogen in the sample per unit surface area can be approximated by using Fick's law (see fig. 5.2):

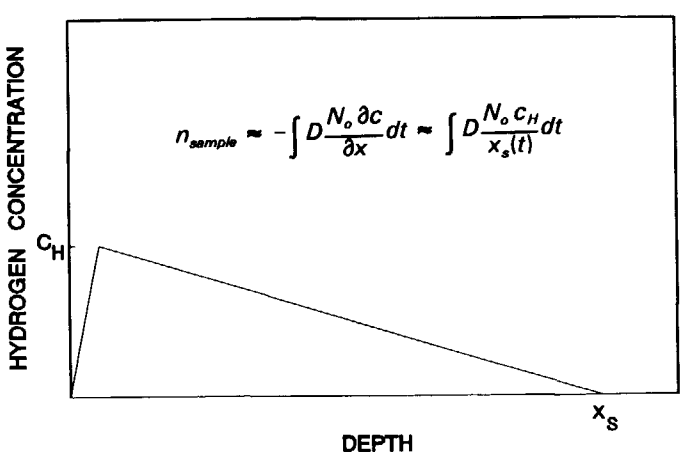

Fig. 5.2. Hydrogen concentration profile in tungsten containing voids. The amount of hydrogen in the sample n_{sample} can be derived from Fick's law. For nomenclature see text.

$$n_{sample} = \int_0^t D \frac{N_0 c_H}{x_s(t')} dt' . \qquad (5.6)$$

When it is assumed that $n_{trapped} \approx n_{sample}$, as is the case in the experiments discussed hereafter, combination of equations 5.5 and 5.6 yields:

$$\frac{D c_H}{c_v N_H} = \tfrac{1}{2} \frac{dx_s^2(t)}{dt} . \qquad (5.7)$$

Solving this equation under the boundary condition that $x_s(0) = 0$ and substituting c_H by expression 5.2 yields the depth x_s as a function of the implanted dose $2\Theta Jt$:

$$x_s = \sqrt{(4\Theta JtL)/(c_v N_H N_o)} \qquad (5.8)$$

Substitution of equation 5.8 into equation 5.5 gives the depth integrated amount of trapped hydrogen:

$$n_{trapped} = \sqrt{4\Theta JtL c_v N_H N_o} . \qquad (5.9)$$

If it is assumed that only molecular hydrogen is present in the voids (*i.e.* $N_H = 2N_{H_2}$, thus neglecting hydrogen atoms that are chemisorbed at the inner surface of the voids), N_H can be calculated as a function of $c_{H,eq}$. This can be done in two steps via the chemical potential μ_{H_2}. The chemical potential governs the flow of particles between systems in thermal and diffusive contact. In thermal and diffusive equilibrium (when the net particle flux between the systems equals zero) the chemical potentials of the chemisorbed hydrogen, the molecular hydrogen, and the interstitially dissolved hydrogen must be equal, *i.e.* $\mu_H = \tfrac{1}{2}\mu_{H_2}$. The relation between $c_{H,eq}$ and the chemical potential μ_{H_2} is given by

$$c_{H,eq} = \exp \frac{\tfrac{1}{2}\mu_{H_2} - G_H^S}{kT} \qquad (5.10)$$

where G_H^S is the free energy of solution of the hydrogen, measured relative to the ground state level of the hydrogen molecule. The relation between the

chemical potential μ_{H_2} and N_H is given by

$$\mu_{H_2} = G/N_{H_2}, \qquad (5.11)$$

where G is the Gibbs free energy. G can be calculated as a function of N_{H_2} by using the Benedict type equations of state for molecular hydrogen and deuterium at high pressures proposed by Mills *et al.*[21,22]. For deuterium *e.g.* Mills *et al.* found:

$$V = (35.283 + 0.00094704T + 3.2843T^{-1/2})p^{-1/3} + (-25.090 + 0.0063917T)p^{-2/3} + (13.650 + 0.069563T - 158.29T^{-1/2} + 720.00T^{-1})p^{-1} \ \text{cm}^3/\text{mole}. \qquad (5.12)$$

The equation of state has been derived for $0.2\times10^9 < p < 2\times10^9$ Pa and $75 < T < 307$ K.

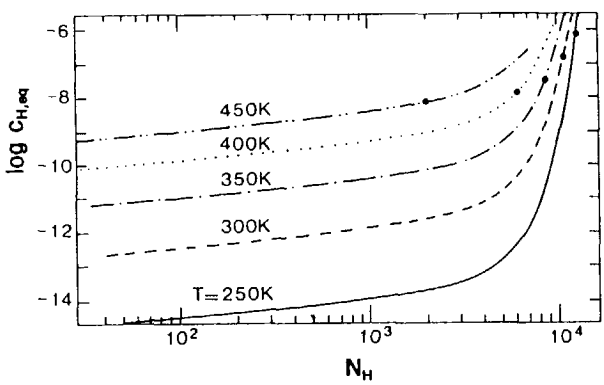

Fig. 5.3. Calculated equilibrium concentration $c_{H,eq}$ versus the average number of deuterium atoms per void N_H for various temperatures. The curves have been calculated for molybdenum with void radius $r_V = 2.7$ nm and $E^S = 0.54$ eV.

As an example, fig. 5.3 shows $c_{H,eq}$ plotted versus N_H for deuterium in molybdenum which contained voids with a radius of 2.7 nm. It can be observed that $c_{H,eq}$ initially increases with the square root of N_H and that due to high pressure effects $c_{H,eq}$ increases much more rapidly with N_H for $N_H > 1000$. The square root behaviour at low N_H follows from the fact that at low pressures the trapped hydrogen behaves like an ideal gas. For an ideal gas, μ_{H_2} is directly proportional to log N_H, and equation 5.10 shows that $c_{H,eq}$ is then proportional to the square root of N_H.

5.3 Application of the model

In this section experiments are described on the interaction between hydrogen and voids in tungsten. In subsections 5.3.1 and 5.3.2 the experimental details and the experimental results are described, and in subsection 5.3.3 the above model is applied on the obtained results. In subsection 5.3.4 it is discussed how Britton *et al.*[23] have applied the model on results obtained for molybdenum.

5.3.1 Experimental details

A pair of tungsten (100) samples, with a purity of 99.995%, a diameter of 9 mm, and a thickness of 1.5 mm, has been irradiated with 1.2×10^{16} cm^{-2} 6 MeV protons. An energy degrader was employed to obtain a uniform damage concentration up to a depth of 32 μm below the surface. The calculated damage level amounted to 6×10^{-4} dpa (displacement per atom), and the vacancy concentration measured with the positron lifetime technique was 40 appm[24]. After annealing to 900 K for 15 minutes, the sample contained 1 appm voids with an estimated size of 30 to 50 vacancies (diameter $\sim$ 1 nm)[24].

Hydrogen decoration of the voids was performed in the gas desorption spectrometer named HDD (see section 2.3) which is usually employed for high dose gas desorption experiments. In this apparatus, a ribbonlike magnetically constricted plasma is created by impact ionization of H_2 gas by electrons from a hot cathode. The sample is negatively biased with respect to the plasma. In the present experiments, typical H_2 ion fluxes were 20 $\mu A/cm^2$ for 2 keV ions at a hydrogen pressure of $\sim 10^{-3}$ Pa. The applied fluences mounted up to 0.5×10^{19} cm^{-2} 2 keV H_2 ions, which effectively corresponds to 1.0×10^{19} cm^{-2} 1 keV H ions. During the hydrogen irradiation the crystals were kept at a temperature of 330 K.

Before, during and after the hydrogen irradiation the samples were subjected to positron lifetime measurements. These measurements have been described earlier by Van Veen *et al.*[10]. They were performed with a conventional lifetime spectrometer[25], having a resolution of 200 ps (FWHM).

Besides positron lifetime measurements, hydrogen desorption experiments have been carried out on the samples. The desorption experiments were performed in the same apparatus as was used to inject the hydrogen in the positron experiments. A quadrupole mass spectrometer tuned to H_2 ions monitored the evolution of the gas release during thermal ramp annealing. The annealing rate was 10 K/s.

5.3.2 Experimental results

Positron lifetime measurements carried out before hydrogen had been injected in the two tungsten samples revealed three positron lifetimes of 80, 150 and 500 ps. These are respectively ascribed to positrons annihilating in bulk material (lifetime τ_1), at dislocation loops (lifetime τ_2), and in voids (lifetime τ_3). Dislocation loops are likely to have been present after the irradiation (see also section 3.3.3), and are expected to produce a lifetime slightly lower than the vacancy lifetime of 180 ps.

After the samples had been irradiated with hydrogen, the values of the three lifetimes were too close to each other to be separated unambiguously. Therefore, a semi-three-term analysis was made with τ_2 kept fixed at 150 ps, thus neglecting possible effects of hydrogen on loops. Fig. 5.4 shows the results, obtained both during the hydrogen implantation and the subsequent annealing treatment from 300 K to 1000 K. It can be observed that after

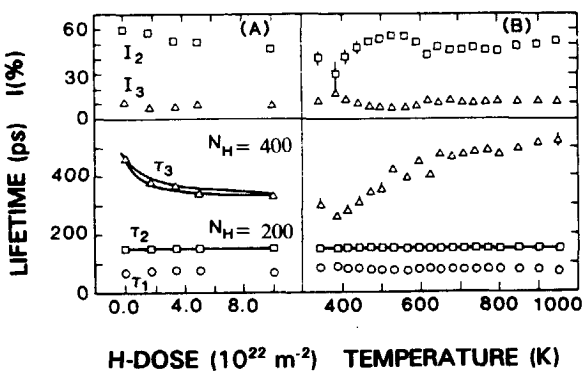

Fig. 5.4. Positron lifetimes and corresponding intensities during (A) hydrogen injection in tungsten and (B) subsequent annealing. In the three term analysis, the lifetime τ_2 was kept fixed at 150 ps. See text for experimental details. The solid curves have been calculated with the model discussed in section 5.3.3.

irradiation with 2×10^{18} cm^{-2} hydrogen atoms the lifetime of positrons annihilating in voids (τ_3) has been reduced from 500 to 350 ps. The main effect of the thermal annealing is that I_3 and τ_3 return to their original values in a broad recovery stage between 450 and 650 K.

Fig. 5.5 shows two hydrogen desorption spectra taken from one of the samples after implanting respectively 0.2 and 0.5×10^{19} cm^{-2} 1 keV hydrogen atoms. The spectra have been corrected for hydrogen desorbing from surrounding parts of the vacuum system. The integral amounts of gas released from voids were respectively 1.2 and 2×10^{18} cm^{-2}. Exposure of a sample at 330 K to a hydrogen gas pressure of 10^{-2} Pa, *i.e.* the ususal ambient pressure

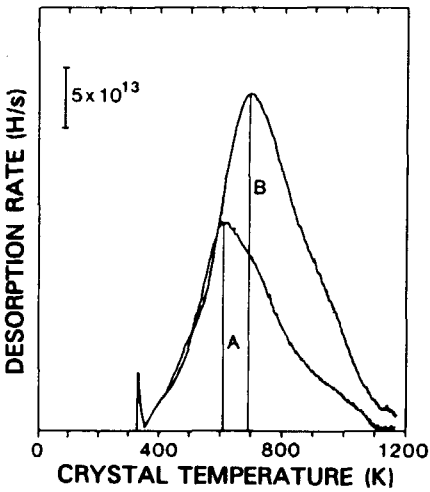

Fig. 5.5. Hydrogen desorption spectra obtained after irradiating a W(100) single crystal containing 1 appm voids with (A) 0.2×10^{19} cm^{-2} and (B) 0.5×10^{19} cm^{-2} 1 keV H ions. The heating rate (10 K/s) was much higher than in fig. 5.4, which causes hydrogen release at higher temperatures (~150 K higher at 700 K).

during implantation, showed hydrogen release peaks at 400 K and 550 K which is typical for desorption of hydrogen from tungsten surfaces[26]. The total amounts released however were an order of magnitude less than found in the experiment where the hydrogen was implanted.

5.3.3 Discussion

a) Hydrogen trapping

The positron annihilation results indicate that the voids are saturable traps for hydrogen (at least for the hydrogen injection temperatures $\geq$330 K) for the simple fact that otherwise the positrons would not have been able to sense the presence of hydrogen. In the presence of unsaturable voids the effective diffusion length for hydrogen would only have been ~50 nm, whereas more than 98% of the positrons annihilates at depths beyond 200 nm[24,27]. Apparently loop-punching conditions were not completely satisfied in the present experiment.

The interstitial hydrogen concentration in the zone where the voids are saturated with hydrogen can be calculated by using equation 5.2. With $\Theta = 0.87$, $J = 1.2 \times 10^{14}$ $cm^{-2}s^{-1}$, $L = 48$ nm for 1 keV H, $N_0 = 6.29 \times 10^{22}$ cm^{-3}, and[28] $D = 4.1 \times 10^{-3} \exp(-E_H^M/kT)$ cm^2/s the calculated concentration equals ~5 appm. Substitution of this concentration in equation 5.10 and using

$G_H^S \approx E_H^S = 1.04$ eV[29] yields a chemical potential of the molecular gas of 1.38 eV. An estimate based on the Mills equation of state yields a corresponding pressure of the order of 10 GPa. These pressures are lower than, but close to, the pressures required for loop-punching. (For bubbles in tungsten with diameters in the order of 1 nm Evans *et al.*[20] expect volume increase by loop-punching beyond 10 GPa).

The effect of high gas pressures on the positron lifetime is expected to be similar to that reported by Hansen *et al.* for high pressure helium bubbles[30]: the lifetime is inversely proportional to the density of the gas. The 330 K injection temperature seems to be critical because it is seen in fig. 5.4 that annealing at a slightly higher temperature leads to a significant reduction in the measured positron lifetime. An extension of the saturated zone caused by redistribution of hydrogen that during injection remained at near surface regions can explain this reduction in the positron lifetime. A similar reduction in lifetime has been observed in section 4.4.2 after nitrogen which had become mobile was trapped at vacancies in molybdenum.

In the thermal hydrogen desorption experiments it was observed that the total amount of trapped hydrogen was proportional to the square root of the dose Jt (not shown here, in the next section it is shown for deuterium in molybdenum). This is in good agreement with the prediction of equation 5.9. Also the positron measurements during the hydrogen injection can be understood with the model of section 5.2. Fig 5.4 shows two curves that have been calculated by assuming that up to an effective depth x_s the voids are saturated with hydrogen and that beyond this depth the voids are empty. The measured positron lifetime τ_3 will be the average of the lifetime in the saturated zone $\tau_{x \leq x_s}$ and that in the empty zone $\tau_{x>x_s}$, weighed by the positron visiting probability:

$$\tau_3 = \tau_{x \leq x_s}[1 - \exp(-\mu_p x_s)] + \tau_{x>x_s} \exp(-\mu_p x_s), \qquad (5.13)$$

where μ_p is the positron absorption coefficient in tungsten. With x_s given by equation 5.8, the best fits are obtained with $200 \leq N_H \leq 400$.

b) Hydrogen desorption

The dissociation rate from voids for hydrogen under pressure will be governed by an activation energy

$$E^{D,H} = E_H^S + E_H^M - \tfrac{1}{2}\mu_{H_2}. \qquad (5.14)$$

Retrapping of the dissociated gas will occur, causing an effective diffusion

with a diffusivity given by equation 5.4. The first amount of gas that will be released from the overpressurized cavity will only require a low activation energy, but gradually the pressure and consequently the chemical potential will decrease, which leads to an increase in the dissociation energy. When the pressure has been reduced to ~1 GPa the chemical potential does not longer contribute significantly to E^D, and the remaining molecular hydrogen will dissociate with a single activation energy. This is in accordance with the positron results shown in fig. 5.4: the release from 400 to 550 K can only be described with a range of activation energies varying from 1.0 to 1.4 eV, and the release from 500 to 650 K with a single activation energy of 1.4 eV[10]. The 1.4 eV agrees well with the expected value of 1.44 eV (see fig. 5.1).

The gas desorption results in fig. 5.5 indicate that also release with higher activation energies than 1.4 eV occurs (note that 700 K on the temperature axis corresponds to 1.4 eV). This is attributed to the release of atomic hydrogen chemisorbed on the inner surface of the voids (to which the positron annihilation technique is insensitive) and for which activation energies of 1.8-2.1 eV are expected (see fig. 5.1). Similar high temperature hydrogen release from irradiated tungsten has also been reported by Erents[2].

5.3.4 A comparison with deuterium in molybdenum

Britton *et al.*[23] have used the model of section 5.2 to interpret experimental results obtained for molybdenum. They performed thermal deuterium desorption experiments on 3 mm diameter Mo disks of 1 mm thickness. Most of their desorption experiments were performed with deuterium instead of hydrogen, because of a better signal to noise ratio (hydrogen is always present as a background gas, whereas deuterium is not). The behaviour of hydrogen and deuterium is expected to be similar, although processes involving the jump frequency can be slightly different[31].

Examples of the obtained desorption spectra are shown in fig. 5.6. It can be observed that the trapped amount reduces with increasing injection temperature. This can be accounted for by looking at fig. 5.3: for the same value of c_H an increase in T causes a reduction in N_H, and thus a reduction in the trapped amount (see equation 5.9). Moreover, an increase in T implies a decrease in c_H (via the diffusivity D, see equation 5.2) and therefore also a reduction in N_H. By utilizing the model of section 5.2, N_H was calculated to vary from 2000 for an implantation temperature T = 450 K to 10000 for T = 250 K.

The peak shapes in fig. 5.6 are characteristic for release by diffusion rather than by dissociation: relatively steep at the low temperature side and less steep at the high temperature side. Diffusional release is in accordance with equation 5.4.

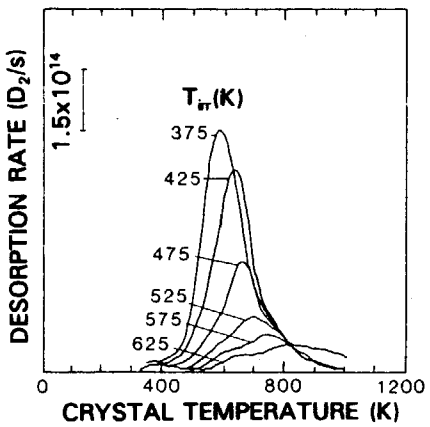

Fig. 5.6. Deuterium desorption spectra obtained after irradiating a Mo single crystal containing 1.2 appm voids with 4×10^{17} cm^{-2} 1 keV D_2 ions. The irradiation temperatures varied as indicated.

In fig. 5.7 it can be noticed that the trapped amount of deuterium increases with the square root of the dose, which is predicted by equation 5.9. The figure also shows that the trapped amounts are reduced when less impurities are present on the sample surface. This is explained by a reduction of c_H due to an increased surface recombination rate[32]. The experimentally found value of $n_{trapped}$ for the clean samples was only 50% lower than the value calculated with equation 5.9.

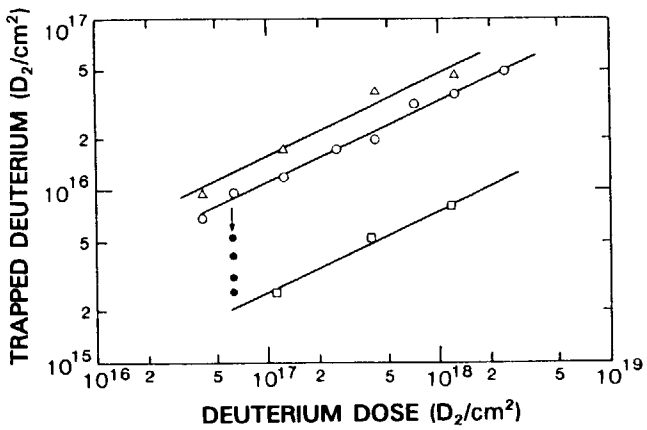

Fig. 5.7. Amount of trapped deuterium in Mo versus 1 keV D_2 ion irradiation dose for: (Δ) an irradiation temperature of 325 K, (o) an irradiation temperature of 450 K, ($\bullet$) the same experiment but stepwise sputter cleaned by 250 eV argon ions (up to 2×10^{18} cm^{-2}), and ($\square$) an electro-polished sample.

By performing irradiations with different hydrogen isotope sequences, Britton *et al.* discovered that the last arriving isotope replaces the first trapped isotope. This ties in with the assumption of a dynamic equilibrium at the saturated voids.

In the experiments on molybdenum carried out by Nielsen *et al.*[7,8] and Hansen *et al.*[9] similar effects were observed as in fig. 5.4. Recovery of the long lifetime component took place at ~500 K. Effects caused by highly pressurized hydrogen gas in the voids were not mentioned however. It is likely that at the hydrogen injection temperature of 300 K the voids in molybdenum are saturated at a lower pressure because the heat of solution of hydrogen is much lower in molybdenum than in tungsten (0.54 eV vs 1.04 eV)[28].

5.4 Conclusions

It can be concluded that with the model presented in section 5.2 the trends found in the experimental work can be reproduced. The model can be improved by including trapping and detrapping rates that depend on the amount of hydrogen per void, by taking into account surface recombination rates, and by incorporating hydrogen chemisorbed at the inner surface of a void. It is expected that in the presented desorption spectra the contribution from chemisorbed hydrogen merges with the high temperature tail of the molecular gas release peak.

It has been shown that positron annihilation combined with hydrogen desorption techniques can succesfully be employed to monitor the exchange of hydrogen with small voids in tungsten and molybdenum. The method gives access to the study of cavities filled with extremely high hydrogen pressures. The activation energies of hydrogen release agree with data known from literature for hydrogen permeation in the case of moderate pressures.

References chapter 5

1. K. Erents and G. McCracken, Brit. J. Appl. Phys. Ser. 2, **2** (1969) 1397.
2. K. Erents, in: Proc. 8th Symp. on Physics of Ionized Gases (J. Stefan Institute, Ljubljana, 1976) p. 299.
3. S.M. Myers, P.M. Richards, W.R. Wampler and F. Besenbacher, J. Nucl. Mater. **165** (1989) 9.
4. Y. Fukai and H. Sugimoto, Adv. Phys. **34** (1985) 263.
5. F. Besenbacher, S.M. Meyers and J.K. Norskov, Nucl. Instr. and Meth. B **7/8** (1985) 55.
6. S.T. Picreaux, Nucl. Instr. and Meth. **182/183** (1981) 413.
7. B. Nielsen, H.E. Hansen, H.K. Nielsen, M.D. Bentzon and K. Petersen, in: Positron Annihilation, eds. P.C. Jain, R.M. Singru and K.P. Gopinathan (World Scientific Publ. Co., Singapore, 1985) p. 497.

8. B. Nielsen, A. van Veen, L.M. Caspers, W. Lourens, G. Trumpy and K. Petersen, in: Positron Annihilation, eds. P.G. Coleman, S.C. Sharma, L.M. Diana (North Holland, Amsterdam, 1982) p. 441.
9. H.E. Hansen, R. Talja, H. Rajainmäki, H.K. Nielsen, B. Nielsen and R.M. Nieminen, Appl. Phys. A **36** (1985) 81.
10. A. van Veen, J. de Vries, D. Segers and G.J. Rozing, in: Positron Annihilation, eds. P.C. Jain, R.M. Singru and K.P. Gopinathan (World Scientific Publ. Co., Singapore, 1985) p. 543.
11. T. Tanabe, N. Saito, Y. Etoh and S. Imoto, J. Nucl. Mater. **103/104** (1981) 483.
12. S.M. Murphy, J. Nucl. Mater. **155-157** (1988) 866.
13. M. Fell and S. M. Murphy, J. Nucl. Mater. **172** (1990) 1.
14. I. Toyoshima and G.A. Somorjai, Catal. Rev. Sci. Eng. **19** (1979) 105.
15. B.L. Doyle, J. Nucl. Mater. **111/112** (1982) 628.
16. F. Waelbroeck, P. Wienhold, and J. Winter, J. Nucl. Mater. **111/112** (1982) 185.
17. M.A. Pick and K. Sonnenberg, J. Nucl. Mater. **131** (1985) 208.
18. A.A. van Gorkum and E.V. Kornelsen, Rad. Eff. **42** (1979) 93.
19. W. Schilling, in: Point Defects and Defect Interactions in Metals, eds. J.I. Takamura, M. Doyama and M. Kiritani (University of Tokyo Press, Tokyo, 1982) p. 303.
20. J.H. Evans and D.J. Mazey, J. Nucl. Mater. **138** (1986) 176.
21. R.L. Mills, D.H. Liebenberg, J.C. Bronson and L.C. Schmidt, J. Chem. Phys. **66** (1977) 3076.
22. R.L. Mills, D.H. Liebenberg and J.C. Bronson, J. Chem. Phys. **68** (1978) 2663
23. D.T. Britton, K.R. Bijkerk, A. van Veen, J.R. Heringa, H.A. Filius, J. de Vries, J.H. Evans and W.H. Segeth, in: Fusion Technology, eds. A.M. van Ingen, A. Nijsen-Vis and H.T. Klippel (North-Holland, Amsterdam, 1989) p. 924.
24. J. de Vries, Ph. D. Dissertation, Delft University of Technology, 1987, p. 20, p. 122, p. 15.
25. J. de Vries, J.M. Schippers and W. Lourens, Nucl. Instr. and Meth. A **238** (1985) 182.
26. P.W. Tamm and L.D. Schmidt, J. Chem. Phys. **51** (1969) 5352.
27. Brandt and R. Paulin, Phys. Rev. B **15** (1977) 2511.
28. R. Frauenfelder, J. Vac. Sci. Technol. **6** (1969) 388.
29. H. Jehn, in: Gase und Kohlenstoff in Metallen, eds. E. Fromm and E. Gebhardt (Springer Verlag, Berlin, 1976) p. 552.
30. H.E. Hansen, H. Rajainmäki, R. Talja, M.D. Bentzon, R.M. Nieminen and K. Petersen, J. Phys. F **15** (1985) 1.
31. Y. Ebisuzaki, W.J. Kass and M. O'Keeffe, J. Chem. Physics **46** (1967) 1373.
32. M.A. Pick, J. Nucl. Mater. **145/147** (1987) 297.

Chapter 6
Miscellaneous experiments

6.1 Introduction

In this chapter, the versatility of gas desorption spectrometry is illustrated by showing its application in three different areas. Firstly, the technique is employed in section 6.2 to gain more insight into the growth process of helium precipitates in molybdenum. Then, in section 6.3, the technique is applied to investigate helium in austenitic stainless steel. In section 6.4, finally, it is demonstrated how gas desorption spectrometry can be utilized to investigate the desorption of volatile species adsorbed at surfaces under the impact of ion irradiation.

6.2 Helium precipitates in molybdenum

6.2.1 Introduction

Studies on the nucleation and growth of helium precipitates in fusion reactor materials have previously been published for Mo[1,2], W[3,4], Ni[5], V[6], Au[7,8] and stainless steel[9]. From the studies on molybdenum it emerged that at room temperature helium precipitates grow as two-dimensional platelets[10,11]. The platelets were found to convert into groups of closely spaced three-dimensional bubbles at temperatures between 900 and 1100 K. In certain cases, this conversion was already observed at room temperature, a phenomenon which was ascribed to overlapping strain fields.

From the fact that the precipitates were unsaturable for helium it was inferred that the growth mechanism is gas-driven. For large precipitates (>500 helium atoms), it was found that the internal pressure (of the order of GPa) is relieved by punching out a platelet of self-interstitial atoms along a glide plane, thereby producing an interstitial dislocation loop[12]. For smaller precipitates the detailed growth mechanism is less clear. It is assumed that also small precipitates can punch out self-interstitials, but since emission of single self-interstitials is energetically not favourable[13], they are expected to remain bound to the defect. It has been conjectured that these bound self-interstitials are the key to the two-dimensional growth[14].

To shed more light on the process of helium precipitation, this section describes three TDS experiments which have been designed to answer the following questions:

1) Does the platelet-bubble conversion influence the growth of helium precipitates?

2) Are small helium precipitates influenced by the presence of self-interstitials?
3) Is there any interaction between helium precipitates and heavy noble gas atoms?

6.2.2 The conversion of helium platelets into bubbles

To answer the first question, the following series of experiments was carried out.

1) Creation of a controlled amount of helium platelets consisting of ~500 helium atoms. (This was realized by creating 1.5×10^{11} cm^{-2} HeV defects by 1.25×10^{12} cm^{-2} 3 keV He ion irradiation followed by annealing up to 1040 K, and addition of 7×10^{15} cm^{-2} 100 eV He).
2) Conversion of the platelets to bubbles of ~2 nm diameter by annealing up to 1600 K. (At this temperature also thermal vacancies are produced which annihilate interstitial loops and bring the bubble pressure in equilibrium).
3) Addition of helium to the bubbles (the experiment was repeated for various doses, up to 1.9×10^{16} cm^{-2} 100 eV).

To check whether the trapping of helium at bubbles differs from the trapping of helium at platelets, the same series of experiments was carried out without step 2. The results are shown in fig. 6.1.

In this figure, three desorption intervals can be distinguished: (1) desorption below 1200 K, which is tentatively assigned to helium trapped at interstitial loops that have been created during the growth of helium platelets, (2) helium desorption between 1600 K and 2100 K, which is associated with release from helium bubbles or platelets, and (3) helium desorption above 2100 K, which is not ascribed to helium release from the sample but to helium release from construction materials in the vicinity of the sample.

In conceiving the experiment, it was presupposed that the sink strength of a defect for a newly arriving helium atom is determined by the effective radius of the defect[15]. The effective trapping cross-section of a helium bubble is then smaller than that of a platelet consisting of the same number of helium atoms. Hence, it was envisaged that bubbles would trap less helium than platelets. Fig. 6.1 however shows that in the two series of experiments no significant difference in trapping has occurred in the second desorption interval. A possible, but unlikely explanation is that helium trapping is not mainly determined by the radius of the defects but by the strain field around the defects. A more likely explanation is that helium bubbles, just like helium platelets, are inclined to grow two-dimensionally. TEM work has already shown that adding helium to small bubbles does not yield larger bubbles, but results in conversion back to platelets[14]. Also platelet nucleation and growth near existing bubbles has been observed. It can be concluded that, although

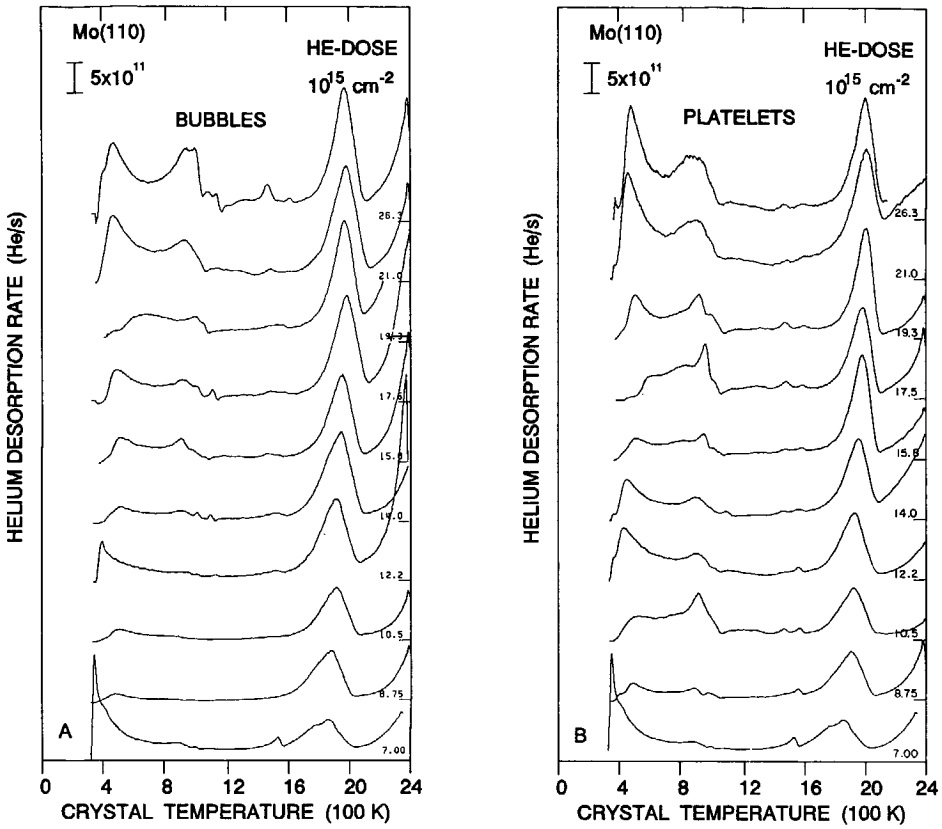

Fig. 6.1. (A) Helium desorption from helium precipitates in Mo(110). Helium platelets have been created in a Mo(110) single crystal by successive irradiation with 1.25×10^{12} cm^{-2} 3 keV He, annealing at 1040 K, and irradiation with 7×10^{15} cm^{-2} 100 eV He. Following this, the crystal was annealed at 1600 K to provoke platelet-to-bubble-conversion. To probe the resulting defect morphology, the crystal was again irradiated with 100 eV He up to the indicated total doses. (B) An identical experiment, but without the annealing step at 1600 K. It can be noticed that there is no significant difference between the two series of spectra.

the exact growth mechanism is still unclear, platelet-to-bubble conversion does not significantly influence the accumulation of helium at helium precipitates.

6.2.3 The interaction between helium precipitates and self-interstitials

To answer the second question, precipitates consisting of 20 helium atoms and 10 vacancies on average were created by adding helium to HeV defects at room temperature[1], and self-interstitials were introduced by 150 eV argon bombardment (80 to 300 self-interstitials per cluster). It was expected that

the helium precipitates would act as nucleation centres for the self-interstitials. Due to the newly arriving self-interstitials the strain energy around the precipitate could be minimized[13], and due to strain relaxation the pressure on the helium atoms in the precipitates would be released. This pressure relaxation should be reflected in a higher helium desorption temperature.

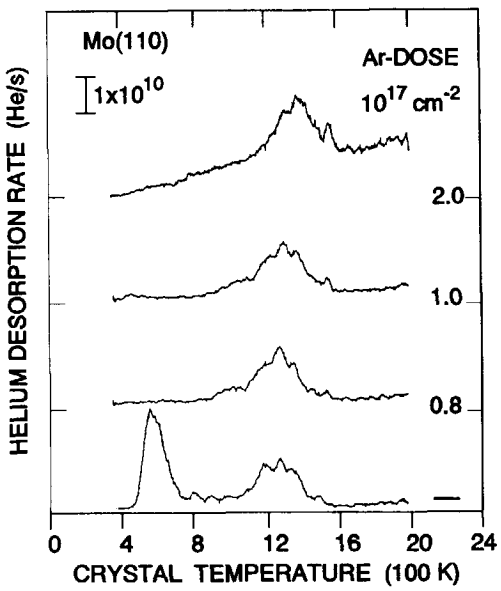

Fig. 6.2. The interaction between helium precipitates and self-interstitials in Mo(110). Clusters of 20 helium atoms on average have been created in a Mo(110) single crystal by successive irradiation with 1.25×10^{12} cm^{-2} 3 keV He, annealing up to 1040 K, and irradiation with 2×10^{14} cm^{-2} 100 eV He. Following this, self-interstitials were introduced in the crystal by bombardment with 150 eV Ar at the indicated doses. It can be observed that the average helium desorption temperature increases with increasing argon dose.

The result of the experiment is shown in fig. 6.2. In this figure, it can be observed that the average helium desorption temperature increases with increasing argon dose, in accordance with the conjecture. For a 150 eV argon dose of 2×10^{17} cm^{-2} *e.g.*, the shift in the average helium desorption temperature mounts to 75 K. Apparently, the small helium platelets are indeed influenced by the presence of self-interstitials. The shift in desorption temperature indicates that pressure release has ensued from a reaction in which extra vacancies are created, such as the reaction

$$He_{20}V_k + I_m \rightarrow He_{20}V_{k+1} + I_{m+1}. \qquad (6.1)$$

This reaction can be explained by the following. During the gas-driven

growth of helium platelets, self-interstitials are pushed out of the defect by the so-called trap mutation process[16]. For these self-interstitials it is energetically favourable to remain bound at the defect[13]. When more self-interstitials arrive however, it may become feasible for the self-interstitials to form interstitial loops. These loops can readily dissociate from the defect, thus providing space for the occurence of a new trap mutation process as is expressed by reaction 6.1. There is no evidence for modification of the defect through leakage of helium along interstitial loops[17].

It must be concluded that the present experiments have rendered evidence that there is a mutual interaction between small helium precipitates and self-interstitials.

6.2.4 The interaction between helium precipitates and heavy noble gas atoms

To answer the third question, substitutional argon atoms were introduced in a Mo(110) sample at an average depth of 20 nm below the sample surface. These were used as nucleation centres for helium precipitates consisting of either 750 or 1400 helium atoms on average. The resulting argon and helium desorption spectra are shown in fig. 6.3. The indicated average number of helium atoms per precipitate <n> has been derived from the amount of desorbed helium per desorbed argon atom.

The most striking result of the experiment is that all the argon atoms are released in the same temperature interval as the helium atoms (figs. 6.3B and 6.3D). This temperature interval is higher than found when no helium had been added (fig. 6.3A). Apparently, all the substitutional argon atoms have acted as nucleation sites for helium precipitates and, moreover, the release of argon is delayed by the helium precipitates.

At closer look, fig. 6.3 displays that helium and argon are not released in exactly the same temperature interval: most of the helium is released about 50 K earlier on the temperature scale than the argon. This indicates that the helium is released by desorption and not by bubble diffusion, since in the case of bubble diffusion both argon and helium should have been released simultaneously. The peak shape confirms this: in the case of bubble diffusion the helium release peak should have had a relatively sharp rise and a long tail. Instead, figs. 6.3C and 6.3E (and also fig. 6.1) show a sharp drop on the trailing edge, which is in accordance with helium desorption from bubbles, followed by bubble shrinkage and increase in helium pressure.

From the experiment the conclusion can be drawn that their is a strong mutual interaction between helium precipitates and substitutional argon atoms.

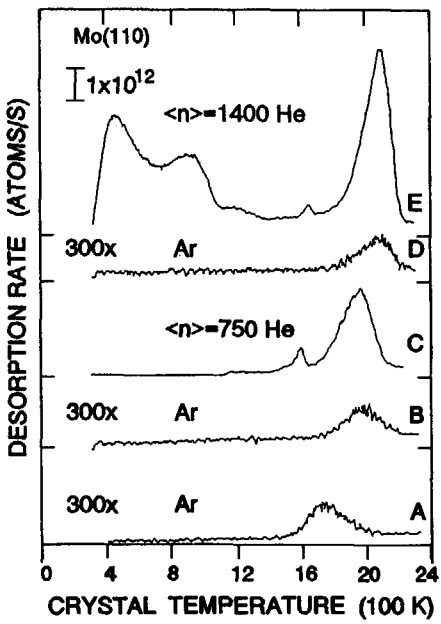

Fig. 6.3. Helium precipitation at substitutional argon atoms in Mo(110). (A) Thermal desorption of substitutional argon, implanted at 3 keV at a dose of 10^{11} cm^{-2}. (B) and (C) Desorption of argon and helium after decorating each ArV with 750 helium atoms on average by 150 eV He irradiation. (D) and (E) Similar to B and C but with 1400 helium atoms on average per ArV. The delay of the argon release by the helium precipitation can clearly be observed.

6.3 Helium in austenitic stainless steel

6.3.1 Introduction

Results on helium trapping, bubble formation and blistering in austenitic stainless steels have been published by Bohdansky *et al.*[18], Jäger and Roth[19], Jung and Schröder[20], and Viswanathan *et al.*[21]. In stainless steels there are far more trapping sites for gas atoms than in pure materials, and consequently the formation of gas bubbles proceeds less readily[22]. For the self-interstitial and vacancy migration energy in austenitic steels values up to ~0.9 eV[23] and ~1.36 eV[24] respectively have been reported.

Due to the high mobility of hydrogen isotopes in stainless steel[25], Yoshida *et al.*[26] have been able to carry out TDS experiments on deuterium in stainless steel. They could distinguish desorption peaks which they ascribed to deuterium release from dislocations and from deuterium clusters.

In this section TDS results are presented on the trapping of helium in the 316 stainless steel which serves as a worldwide reference material for fusion

applications (see section 2.2). The obtained spectra are compared with spectra from a pure $Fe_{70}Cr_{17}Ni_{13}$ single crystal. The results are also compared with results on nickel, firstly because this is the element which mostly resembles austenitic stainless steels, and secondly because it is the base material for the fusion material candidate inconel.

6.3.2 Experimental results

Before carrying out gas desorption experiments, positron lifetimes have been determined for the 316 reference steel. Two lifetimes were measured of (98 ± 5) ps (intensity 49%) and (174 ± 14) ps (30%). The first lifetime is ascribed to annihilation in the bulk of the stainless steel, the second lifetime to annihilation at dislocations, structural defects, and vacancies. (A third lifetime ascribed to voids and grain boundaries was fixed on 360 ps). Neither annealing for 1800 s at 500 K nor an attempt to fill the samples electrolytically with hydrogen (in 5% aqueous solution with 200 mg/l As_2O_3 to reduce H_2 surface recombination, 5400 s, 300 mA/cm^2) yielded significant changes.

For the pure $Fe_{70}Cr_{17}Ni_{13}$ only one bulk lifetime of (115 ± 5) ps was measured, indicating the complete absence of defects in the bulk of the sample. For pure nickel the positron bulk lifetime has been determined by *e.g.* Naidu *et al.*[27], who reported a value of (110 ± 4) ps. Thus, the bulk lifetimes in both $Fe_{70}Cr_{17}Ni_{13}$ and nickel are higher than the bulk lifetime of (98 ± 5) ps measured for the 316 reference steel. This demonstrates that in the 316 reference steel defects are present in high concentrations. A high defect concentration causes a high positron trapping rate and, according to the two state trapping model[28], a high positron trapping rate causes a decrease in the measured bulk lifetime.

In fig. 6.4 helium desorption spectra are shown, measured for a Ni(110) single crystal, a $Fe_{70}Cr_{17}Ni_{13}$(11,3,1) single crystal, and a sample made out of the polycrystalline 316 reference steel. All samples were irradiated with 1 keV helium ions at varying doses. In the Ni spectra two salient peaks labelled G and H are visible, which are attributed to helium desorption from HeV (H peak, in accordance with the literature value[29] for $E_{HeV}^{D,He}$ of 2.2 eV) and $He_{2,3,4\ or\ 5}V$ defects (G peak). Similar peaks can be seen in the FeCrNi spectra, indicating that also here monovacancies have been created which have trapped helium. Contrarily to the Ni spectra, the FeCrNi spectra also contain desorption peaks at lower temperatures. In the spectra from the 316 reference steel, desorption at lower temperatures is observed as well, but distinct G and H peaks cannot be recognized. Here, most of the helium is released between 1000 and 1400 K.

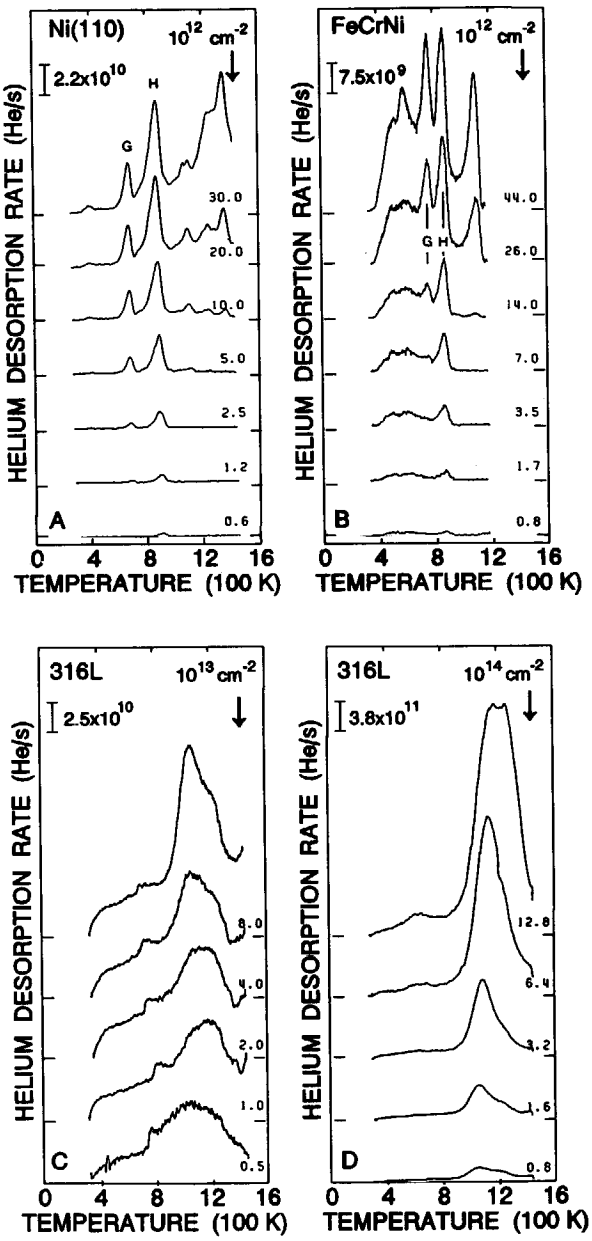

Fig. 6.4. Desorption of helium from (A) Ni(110), (B) FeCrNi, (C) and (D) stainless steel 316L, after irradiation with 1 keV He ions at the indicated doses. The peaks labelled G and H are ascribed to release from monovacancies.

6.3.3 Discussion

The helium population of the G and H peaks in the Ni and FeCrNi spectra is plotted in fig. 6.5. It can be noticed that at low doses the curves have a slope

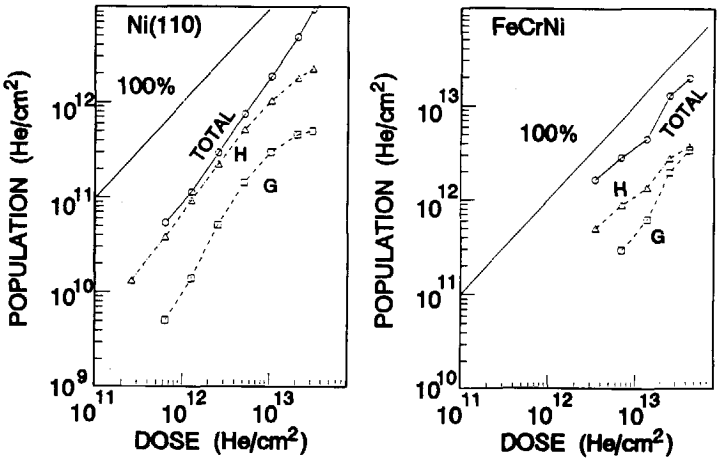

Fig. 6.5. Helium population of the G and H peaks in figs. 6.4A and 6.4B versus helium irradiation dose. The total amount of trapped helium and the line for 100% trapping are also indicated.

which is larger than unity, and that only a small fraction of the implanted helium is trapped. The explanation is that at low doses the production rate of HeV defects is proportional to both the helium and the vacancy concentration. Since both increase linearly with the irradiation dose P, the number of HeV defects would theoretically be proportional to P^2. Analogously, the number of He_2V defects would theoretically be proportional to P^3. At low irradiation doses however, helium trapping at impurities also plays a competitive role, and therefore the P^2 and P^3 behaviour is not quite observed in the curves of fig. 6.5. Nevertheless, it is clear that at low doses the slopes of the curves are larger than unity. At intermediate doses the formation of new defects will be counterbalanced by defect reduction through self-interstitials ($He_nV + I \rightarrow nHe$ or $HeV_m + I \rightarrow HeV_{m-1}$). Only defects that are resistant to reduction will then continue to grow.

The peaks in the Ni spectra above 1200 K have also been observed by Yamauchi *et al.*[30], who employed much higher irradiation doses (up to $5x10^{17}$ cm^{-2}) and energies (20 keV). They attributed these peaks to thermal vacancy assisted bubble diffusion. Thermal vacancies in nickel are already expected to be mobile at 950 K (which corresponds to 2.5 eV)[6]. Hence, any helium release from bubbles which would occur above 950 K by a jump-out mechanism is

pre-empted by thermal vacancy assisted bubble diffusion. The binding energy of helium atoms to small helium bubbles in nickel have been calculated by Adams and Wolfer[31]. The high binding energies of up to 4 eV which they reported are in line with the conclusion that thermal vacancy assisted bubble diffusion takes place at lower temperatures than a jump-out mechanism.

The peaks at low temperatures in the FeNiCr spectra are likely due to structural defects in the alloy and to impurities (the sample contained more than 50 ppm C in the surface regions).

In the spectra from the 316 reference steel, which contained substantially larger amounts of structural defects and open volume than the Ni and FeCrNi crystals, distinct desorption peaks indicating the presence of monovacancies can not be recognized. Instead, the helium is bound to defects with a range of binding energies which are too close to each other to be experimentally resolved. The implanted helium and the formed self-interstitials are most likely trapped by the vast amounts of structural defects and impurities so that a larger fraction of the vacancies than in nickel remain empty or survive recombination. During heating the vacancies are expected to become mobile and to be trapped at other defects, resulting in a high concentration of relatively small helium-vacancy clusters from which helium desorbs in the temperature interval between 1000 and 1400 K.

For stainless steel type 304[32,33,34] and the reference steel for the Japanese[35] and Chinese[36] fusion program, helium release was found in the same temperature interval as found here (1000-1400 K). This was ascribed to helium release from bubbles. Rothaut *et al.*[9] have performed TEM experiments on helium bubbles in the 316 reference steel. They observed bubble coarsening during isothermal annealing at 1073 K which they ascribed to the Ostwald ripening mechanism, *i.e.* helium jump-out from highly pressurized small bubbles and successive migration to less pressurized large bubbles. For the helium dissociation energy they deduced a value of (3.5 ± 0.5) eV, which is in accordance with the 1000-1400 K temperature interval observed in the THDS experiments reported here. The observed stabilization of vacancy clusters in stainless steel by helium up to temperatures far above 1000 K is also in accordance with positron results by Viswanathan *et al.*[37]. Note that for deuterium this vacancy cluster stabilization has not been observed: deuterium release always took place below ~ 900 K[25,38,39].

As has been mentioned above, in our THDS experiments nucleation and growth of helium bubbles has occurred during implantation, and further growth has occurred during annealing. Due to the low energies employed however (1 keV), the bubbles are situated very close to the surface in higher concentrations than in the experiments reported by the other authors who used energies varying between 450 keV and 40 MeV. Therefore, bubble

coarsening due to Ostwald ripening is in our experiments hindered by loss of helium at the surface. Besides, vacancies supplied by the nearby surface may enhance the relaxation of overpressurized bubbles[40], thus putting a halt to the Ostwald ripening process.

Schröder *et al.*[41] have pointed out that in areas with high helium concentration, as is the case in our experiments, bubble migration is the leading helium transport mechanism and not a jump-out process. In our case it is therefore envisaged that, although initially helium release predominantly takes place by a jump-out mechanism from highly overpressurized bubbles (with high chemical potential, see chapter 5), at higher temperatures the jump-out mechanism and the bubble migration mechanisms occur simultaneously. The dominating release mechanism and the release energy are expected to depend on the local bubble size (the larger the bubble the higher the helium dissociation energy), bubble pressure, local bubble concentration, distance to the surface and the strain fields around the bubbles (which in turn depend on the local composition of the stainless steel). All these parameters change continuously during annealing.

It can be concluded that both the positron measurements and the helium desorption experiments have yielded clear evidence that in the investigated stainless steel structural defects and impurities are present in vast amounts. In the positron measurements this was shown by the relatively small positron bulk lifetime, in the THDS experiments by the absence of a distinct desorption peak associated with monovacancies. A detailed defect assignment in stainless steel is impeded by the vast amounts of defects. Despite this handicap, it has been shown that thermal gas desorption spectrometry can render useful supplementary information. The information obtained is expected to degrade with the complexity of the system under investigation. In the present experiments helium release from bubbles has been observed and the release mechanism has been discussed. It should finally be remarked that due to reordering caused by ion bombardment and heating, thermal gas desorption spectra of alloys are not always well reproducible.

6.4 Ion irradiation induced desorption

6.4.1 Introduction

In fusion reactors the plasma can be contaminated by gaseous species that desorb from surfaces under the impact of ion irradiation. To investigate this process of ion irradiation induced desorption (also called ion impact desorption) and to determine cross-sections for the process, a start was made with the development of a new desorption spectrometer. This spectrometer has been described in section 2.6. In the present section a survey is given of

the existing literature on ion irradiation induced desorption, preliminary test measurements on the performance of the new spectrometer are reviewed, and suggestions are given for future developments of the new spectrometer. All the experiments presented here have been carried out on a 10 mm stainless steel sample made out of the 316 reference steel.

6.4.2 Survey of previous research

The first experiments on ion irradiation induced desorption were carried out by Winters and Sigmund[42,43]. By using flash filament techniques and mass spectrometry, they showed that on tungsten nitrogen is adsorbed and sputtered as atoms. The sputtering yield was found to be proportional to the coverage. Winters and Sigmund distinguish three dominating collisional processes: adsorbed atoms are removed (1) directly by a projectile ion, (2) by a reflected projectile, or (3) by recoiled substrate atoms produced in a collision cascade. At low energies processes 1 and 2 will be dominant, at high energies process 3. In the latter case, the sputtering yield for adsorbates will be lower than for substrate elements (for comparable binding energies). Assuming binary collisions, Winters and Sigmund have been able to calculate sputtering yields that are in agreement with their experimental data.

Farell and Eghawary[44] have measured desorption cross sections of CO adsorbed on stainless steel 304 irradiated by H, D, He, Ne and Ar ions. They monitored CO pressure changes when switching on and off their ion beam. The CO release rate obeyed the equation

$$r(t) = n\,A\,J\,\sigma\,exp\,(-J\sigma t)\ \text{'molecules/s} \qquad (6.2)$$

with n the initial CO coverage (molecules/cm^2), A the bombarded area, J the incident particle flux (cm^{-2}s^{-1}), and σ the desorption cross section (cm^2). Farell and Eghawary found that CO is sputtered as a molecule, and noted that cross-sections for non-polished surfaces are difficult to determine because the absorbing area may be significantly greater than the geometrical area (for stainless steel a factor 7 after prolonged ion bombarment). They also observed that adsorption of *e.g.* O and H occurs more readily on a stepped than on a smooth surface.

Taglauer *et al.*[45,46,47] have demonstrated that backscattering of low energy rare gas ions (briefly called ion scattering spectrometry or ISS) is a powerfool tool for adsorbed layer analysis. They have compared their measurements with MARLOWE calculations[48,49] (see section 1.2), and found that σ is approximately inversely proportional to the binding energy of the adsorbate[50]. They confirmed that CO is desorbed as a molecule, whereas oxygen atoms are removed as atoms[51]. On a metal substrate (such as

stainless steel) oxygen was found to come off as a metal oxide[52]. Sagara *et al.*[53] have performed ISS experiments on Mo and Ni and made a compilation of the data on ion impact desorption available before 1982[54].

Bastasz and Haggmark[55] have used secondary ion mass spectrometry (SIMS) to investigate hydrogen impact desorption of adsorbed deuterium from stainless steel 316. Desorption cross sections decreased from 1.2×10^{-18} cm^2 for hydrogen energies of 0.3 keV/atom to 5×10^{-17} cm^2 for 1.5 keV/atom.

Morita *et al.*[56,57,58] found with Rutherford backscattering that at least for gold atoms on nickel the adsorbate concentration does not decrease exponentially with ion dose, but bi-exponentially. The slow component was ascribed to recoil implanted adsorbate atoms that reappear at the surface via ion induced mixing.

Ion impact desorption has also been simulated by using sputtering theory for multicomponent targets[59] or analytically by adopting the three collisional mechanisms in the model of Winters and Sigmund mentioned above. Brodkorb[60] has thus analytically calculated that if the masses of the primary, adsorbed and substrate particles are all of the same order, mechanism 3 is the most important. If primary and adsorbate masses are much smaller than the mass of te substrate atoms, mechanisms 1 and 2 are dominant.

6.4.3 Preliminary test experiments on the new impact desorption spectrometer.

The development of the new desorption spectrometer in Delft, described in section 2.6, has been aimed towards monitoring species coming off the surface rather than species that remain on the surface. When monitoring the remaining species, as is done in ISS measurements, it is impossible to distinguish whether the particles removed from the surface are desorbed or recoil implanted. Auger electron spectrometry (AES) has the additional disadvantage that hydrogen and deuterium cannot be detected, and also that the signal does not only come from the surface layer but also from deeper layers.

As a preliminary test on the desorption spectrometer described in section 2.6, an experiment has been performed in which a stainless steel surface was covered with CO before irradiation with He. The mass spectrometer was used in the mode to measure neutral particles coming off the sample surface. Switching on and off the ion beam gave the result shown in fig. 6.6 for the simultaneously measured masses 4, 12, 16 and 28. From the figure it can be concluded that ion irradiation induced desorption can indeed be observed with the new spectrometer, and that the simultaneous measurement of different masses works satisfactorily. Other experiments showed that, as envisaged, variations in irradiation energy resulted in variations in desorption yield. It

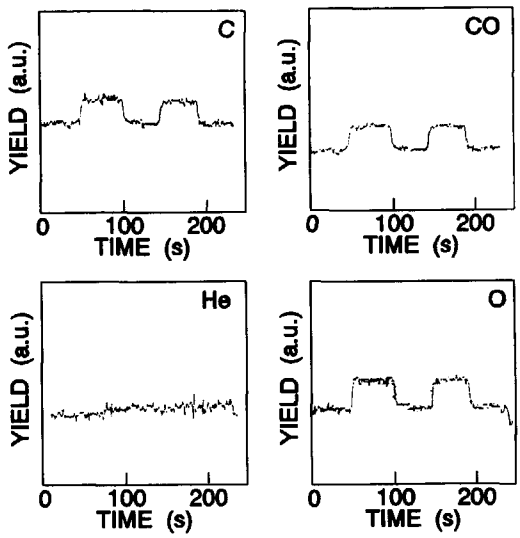

Fig. 6.6. Partial pressures of masses 4 (He), 12 (C), 16 (O) and 28 (CO) versus time during 2 keV He bombardment of stainless steel 316L covered with CO. The masses were measured simultaneously. The ion beam was switched on and off every 50 seconds. The pressure scales have not been calibrated.

cannot be concluded from fig. 6.6 that C and O are desorbed dissociatively, since the signals at masses 12 and 16 also show up in the fingerprint spectrum of CO. It was further observed that under prolonged argon bombardment the CO signal decays with time.

Apart from CO, also Fe, Cr and Ni were observed to come off the surface, both when the sample was irradiated with argon (fig. 6.7A) and when it was heated to 960 K after prolonged argon bombardment (fig. 6.7B). Apparently, the bombardment decreased binding energies for Fe, Cr and Ni atoms.

Before drawing the conclusion that the spectrometer suits its purpose, it ought to be noted that the measured signal not just represents the signal from the stainless steel sample, but also from the diaphragm and components in the ion source. Experiments to discriminate the sample contribution from the background contribution by changing the position of the mass analyser were to no avail. Therefore, experiments have been carried out in which the spectrometer was used in the SIMS (secondary ion mass spectrometry) mode. In this mode, only ions are detected by the mass analyser, no neutral particles. Due to its limited acceptance angle the mass analyser mainly detects ions coming off the sample surface. Despite the fact that the fraction of secondary particles that come off as ions is at most a few percent, and although only the energetic ones are accepted by the mass analyser, there is no signal loss due to an additional ionisation step (when neutrals are monitored, the ionisation

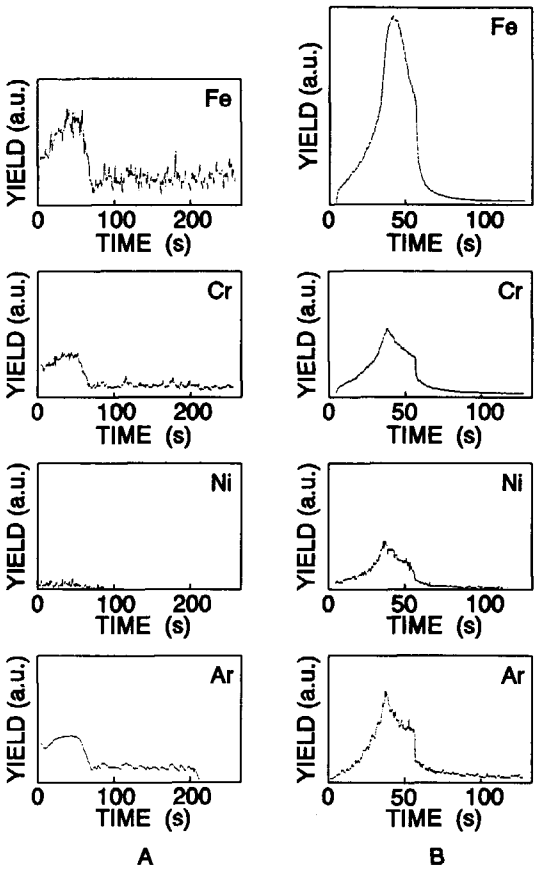

Fig. 6.7. Partial pressures of Ar, Ni, Cr and Fe versus time, (A) during 1 keV Ar bombardment of stainless steel 316L (ca. 1 μA/cm^2, at t = 70 s the ion beam was switched off), and (B) during heating to 960 K after prolonged argon bombardment.

efficiency in the mass analyser varies between 10^{-6} to 10^{-4} depending on the monitored species).

To demonstrate that SIMS experiments can be performed with the new desorption spectrometer, fig. 6.8 shows the result of an experiment in which a stainless sample was covered with CO and bombarded with He. The figure shows that a CO signal can be measured and that the signal disappears when the sample is rotated out of the beam. A clear exponentional decay with time has not been observed however.

What has been observed is that ion bombardment of the sample and surroundings causes a high intensity of species with a low ionisation potential such as Na (ionisation potential 5.14 eV) and K (4.34 eV) in the SIMS spectra.

These ions are expected to come not only from the sample but also from windows which are within the acceptance angle of the mass analyser or from vacuum cleaning chemicals. This effect, which has also been noticed by *e.g.* Matthewson[61] is something to bear in mind for the ion inventory in fusion machines.

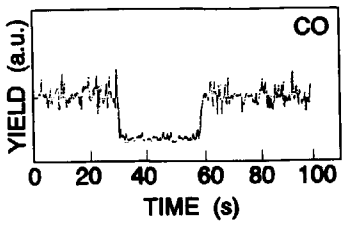

Fig. 6.8. Intensity of CO ions versus time during 1 keV He irradiation of stainless steel 316L covered with CO. At t = 30 s the sample was rotated out of the ion beam.

Another observation was that in the mass spectra the relative peak intensities depend considerably on the sample potential. This is explained by the fact that the detection probability of the ions depends largely on the trajectories of the ions in the mass analyser. The trajectories of the ions are determined by their energies, and these in turn depend on the sample potential.

As was the case in monitoring neutral particles, various species were observed to come off the target when it was heated to 1100 K. Among them were Fe, Cr and Ni. These species were ionised by the heating filament.

6.4.4 Future developments

The SIMS measurements have only been performed to explore the capabilities of the spectrometer. As has been observed by other authors, quantitative SIMS measurements are very unreliable since the ionisation efficiency of the secondary particles at the surface is highly influenced by the continuous changes in surface structure and composition[62,63] (in the case of stainless steel ion beam mixing occurs), by the collection of primaries, and by the changes in gas coverage (oxygen is known to enhance the secondary ion yield significantly).

For quantitative measurements on neutral particles, it is clear that modifications of the present apparatus are indispensible. To improve the signal to noise ratio it is foreseen that the ion source including the diaphragm will have to be pumped differentially and that a separate chamber will have to be added in which solely the samples are covered with gas atoms. Besides, it is noteworthy that, although SNMS (sputtered neutral mass spectrometry) is still a developing technique[64,65], energy measurements on sputtered neutrals can be very helpful to reject background signals.

Instead of monitoring the species that come off the surface during bombardment it is possible to monitor the species that remain on the surface by doing flash desorption or ISS measurements (which include ion energy

determination). With minor modifications, both types of measurements are possible with the present equipment.

References chapter 6

1. See *e.g.* A. van Veen, J.H. Evans, W.Th.M. Buters and L.M. Caspers, Rad. Eff. **78** (1983) 53.
2. For positron experiments see *e.g.* P.M.G. Nambissan, P. Sen and B. Viswanathan, Radiation Effects and Defects in Solids **116** (1991) 125.
3. E.V. Kornelsen and A.A. van Gorkum, Rad. Effects **42** (1979) 113.
4. G.J. van der Kolk, A. van Veen, L.M. Caspers and J.Th.M. de Hosson, J. Nucl. Mater. **127** (1985) 56.
5. A. van Veen, J.H. Evans, L.M. Caspers and J.Th.M. de Hosson, J. Nucl. Mater. **122&123** (1984) 560.
6. W. Jäger, R. Lasser, T. Schober and G.J. Thomas, Rad. Eff. **78** (1983) 165.
7. J.H. Evans and A. van Veen, J. Nucl. Mater. **168** (1989) 12.
8. J.H. Evans, A. van Veen and M.W. Finnis, J. Nucl. Mater. **168** (1989) 19.
9. J. Rothaut, H. Schröder and H. Ullmaier, Philos. Mag. A **47** (1983) 781.
10. J.H. Evans, A. van Veen and L.M. Caspers, Nature **291** (1981) 310.
11. A. van Veen, L.M. Caspers and J.H. Evans, J. Nucl. Mater. **103&104** (1981) 1181.
12. J.H. Evans, A. van Veen and L.M. Caspers, Scripta Met. **15** (1981) 323.
13. L.M. Caspers, M. Ypma, A. van Veen and G.J. van der Kolk, Phys. Stat. Sol. (a) **63** (1981) 183.
14. J.H. Evans, A. van Veen and L.M. Caspers, Rad. Eff. **78** (1983) 105.
15. R.H.J. Fastenau and P. Penning, Phys. Stat. Sol. (a) **66** (1981) 613.
16. A. van Veen, L.M. Caspers, E.V. Kornelsen, R.H.J. Fastenau, A.A. van Gorkum and A. Warnaar, Phys. Stat. Sol. (a) **40** (1977) 235.
17. W.Th.M. Buters, J.H. Evans, A. van Veen and A. van den Beukel, Defect and Diffusion Forum **57-58** (1988) 75.
18. J. Bohdansky, K.L. Wilson, A.E. Pontau, L.G. Haggmark and M.I. Baskes, J. Nucl. Mater. **93&94** (1980) 594.
19. W. Jäger and J. Roth, Nucl. Instr. Meth. **182&183** (1981) 975.
20. P. Jung and K. Schröder, J. Nucl. Mater. **155-157** (1988) 1137.
21. B. Viswanathan, G. Kögel, P. Sperr and W. Triftshäuser, in: Positron Annihilation, eds. P.G. Coleman, S.C. Sharma, L.M. Diana (North Holland, Amsterdam, 1982) p. 520.
22. D.S. Whitmell and R.S. Nelson, Rad. Effects **14** (1972) 249.
23. C. Dimitrov and O. Dimitrov, J. Phys. F **14** (1984) 793.
24. E. Kuramoto, N. Tsukuda, Y. Aono, T. Takenaka, Y. Takano, H. Yoshida and K. Shiraishi, J. Nucl. Mater. **133&134** (1985) 561.
25. C.J. Altstetter, R. Behrisch and B.M.U. Scherzer, J. Vac. Technol. **15** (1978) 70.

26. N. Yoshida, N. Ashizuka, T. Fujiwara, T. Kurita and T. Muroga, J. Nucl. Mater. **155-157** (1988) 775.
27. S.V. Naidu, A. Sen Gupta, G. Mukhopadhyay, R.K. Bhandari and P. Sen, Rad. Eff. **83** (1984) 129.
28. A. Seeger, Appl. Phys. **4** (1974) 183.
29. D. Edwards and E.V. Kornelsen, Surf. Sci. **44** (1974) 1.
30. T. Yamauchi, S. Yamanaka and M. Miyake, J. Nucl. Mater. **179-181** (1991) 308.
31. J.B. Adams and W.G. Wolfer, J. Nucl. Mater. **166** (1989) 235.
32. D.S. Whitmell and R.S. Nelson, Rad. Effects **14** (1972) 249.
33. W. Bauer and W.D. Wilson, in: Proc. Int. Conf. on Radiation-Induced Voids in Metals (Albany, 1971) p. 230.
34. G. Carter, D.G. Armour, S.F. Donelly, D.C. Ingram and R.P. Webb, in: Proc. Consultants Symp. on Inert Gases in Metals (AERE Report 9733, Harwell, 1980) p. 83.
35. A. Uedono, S. Tanigawa and H. Sakairi, J. Nucl. Mater. **173** (1990) 307.
36. P. Wang, Y. Li, J. Liu, G. Zhang, R. Ma, P. Zhu, C. Qiu, T. Xu, J. Nucl. Mater. 169 (1989) 167.
37. B. Viswanathan, W. Triftshäuser, G. Kögel, Rad. Eff. **78** (1983) 231.
38. C. Lopes Gil, A.P. de Lima, N. Ayres de Campos, P. Sperr, G. Kögel and W. Triftshäuser, Radiation Effects and Defects in Solids **112** (1990) 111.
39. N. Yoshida, T. Kurita, T. Fujiwara and T. Muroga, J. Nucl. Mater. **162-164** (1989) 1082.
40. V.N. Chernikov, H. Trinkaus, P. Jung and H. Ullmaier, J. Nucl. Mater. **170** (1990) 31.
41. H. Schröder and P.F.P. Fichtner, J. Nucl. Mater. **179-181** (1991) 1007.
42. H.F. Winters, J. Vac. Sci. Technol. **8** (1971) 17.
43. H.F. Winters and P. Sigmund, J. Appl. Phys. **45** (1974) 4760.
44. G. Farell and B.D. Eghawary, J. Nucl. Mater. **93&94** (1980) 834.
45. E. Taglauer, G. Marin, W. Heiland, Appl. Phys. **13** (1977) 47.
46. E. Taglauer and W. Heiland, J. Nucl. Mater. **76&77** (1978) 328.
47. E. Taglauer, W. Heiland, J. Onsgaard, Nucl. Instr. and Meth. **168** (1980) 571.
48. E. Taglauer, G. Marin, W. Heiland and U. Beitat, Surface Sci. **63** (1977) 507.
49. E. Taglauer and U. Beitat, J. Nucl. Mater. **111&112** (1982) 800.
50. E. Taglauer, W. Heiland and U. Beitat, Surface Sci. **89** (1979) 710.
51. E. Taglauer and W. Heiland, J. Nucl. Nater. **93&94** (1980) 823.
52. E. Taglauer, W. Heiland, R.J. Mac Donald, Surface Sci. **90** (1979) 661.
53. A. Sagara, K. Akaishi, K. Kamada and A. Miyahara, J. Nucl. Mater. **103&104** (1981) 357.
54. A. Sagara and K. Kamada, J. Nucl. Mater. **111&112** (1982) 812.
55. R. Bastasz and L.G. Haggmark, J. Nucl. Mater. **111&112** (1982) 805.
56. K. Morita, M. Takami, H. Ohno, Surface Sci. **157** (1985) 361.
57. K. Morita and H. Morii, Nucl. Instr. Meth. B **13** (1986) 457.
58. K. Morita, H. Morii, Y. Horino, Nucl. Instr. Meth. B **18** (1987) 407.

59. P. Sigmund, A. Oliva and G. Falcone, Nucl. Instr. and Meth. **194** (1982) 541.
60. W. Brodkorb, Phys. Stat. Sol. (a) **94** (1986) 83.
61. A.G. Mathewson, CERN report ISR-VA/74-30.
62. D. Armour, in: Proc. NATO-ASI on Plasma-Surface Interactions (Kluwer, Dordrecht, 1989).
63. K. Wittmaack, Nucl. Instr. Meth. **168** (1980) 343.
64. D. Lipinsky, R. Jede, O. Ganschow, A. Benninghoven, J. Vac. Sci. Technol. A **3** (5) (1985) 2007.
65. H. Gnaser, J. Fleischhauer, W.O. Hofer, Appl. Phys. A **37** (1985) 211.

Summary

This thesis presents a study which has been carried out to explore and demonstrate the versatility of thermal gas desorption spectrometry as a tool to investigate the interaction between gaseous impurities and point defects in nuclear fusion reactor materials.

In chapter 1 a brief introduction is given into nuclear fusion reactor materials, the behaviour of defects in these materials, and the technique which has been used in the present study to investigate the defects, *i.e.* thermal gas desorption spectrometry.

Chapter 2 describes the apparatus which has been employed to conduct the gas desorption experiments. It is explained how specimens have been prepared, how a desired defect structure has been created in the specimens, how the release of trapped gas has been monitored, and how information about defects has been extracted from gas desorption spectra. A brief description is given of the positron annihilation technique, which has been applied throughout this work to supplement the information obtained by gas desorption spectrometry. Chapter 2 also presents two gas desorption spectrometers which have been designed to study ion irradiation induced desorption and hydrogen isotope permeation.

In chapter 3 it is shown how the gas desorption technique has been employed to investigate the interaction between self-interstitials and argon in molybdenum. Firstly, a novel method to create self-interstitials without interfering vacancies is examined more closely. Corroborative evidence is presented which proves that low energy heavy ion bombardment provides a useful technique for the controlled production of stable self-interstitial atoms. The vital role of so-called replacement collision sequences in the self-interstitial production process is established, and threshold energies for the generation of self-interstitials are accounted for.

The self-interstitial production technique which is discussed in the first part of chapter 3 has been utilized to study the influence of self-interstitial atoms on the retention of gas atoms in fusion reactor materials. It is shown that the retention of argon in low energy high fluence argon irradiated molybdenum cannot be described by a linear superposition of low fluence trapping processes. This fact is partly due to the sputtering of accumulated argon atoms, and partly to the intimate interaction between deposited argon and irradiation induced self-interstitials. The experimental results reveal that saturation in argon retention which has been reported by other authors is quasi-saturation. It is pointed out that at fluences higher than those explored by previous authors, argon retention is governed by relatively stable defect complexes consisting of self-interstitial atoms and argon atoms.

In chapter 4 it is demonstrated that thermal gas desorption spectrometry provides a sensitive technique for measuring the concentration of vacancy type defects at low defect concentrations. It is shown how the technique can be used to measure vacancy annealing curves and how the vacancy migration energy can be extracted from the annealing curves by using a simple diffusion model. In molybdenum, the vacancy migration was found to be (1.23 ± 0.04) eV. The presence of hydrogen did not produce any measurable effect on the annealing of vacancies in molybdenum. An attempt to estimate the dissociation energy of a hydrogen atom bound to a vacancy in molybdenum yielded that this energy is less than 1.4 eV.
A substantial part of chapter 4 is devoted to the interaction between nitrogen and vacancies in molybdenum. By applying novel defect assignment methods and theoretical considerations, it is more strongly established that the detrapping of a nitrogen atom from a single vacancy in molybdenum requires an activation energy of (2.55 ± 0.05) eV. The main influence of nitrogen on vacancies is that it enhances the vacancy production rate and that it strongly promotes the thermal stability of vacancies. This implies that the presence of nitrogen plays an important role in controlling void nucleation and growth.
A study into the interaction between nitrogen and small vacancy clusters in molybdenum displays the limitations of thermal gas desorption spectrometry in identifying compound defects. It is shown how, in spite of these limitations, the nature of compound defects can be deduced *per exclusionem* by combining theoretical considerations with available information on smaller defects. Thus, small nitrogen-vacancy clusters have been identified which are stable up to an annealing temperature of 1100 K. The mutual binding was found to immobilize both the nitrogen and the vacancies. In the case of helium-nitrogen-vacancy complexes it is inferred that upon annealing the nitrogen generally leaves the complexes before the helium is released. The main conclusion is that, just like monovacancies, vacancy clusters without nitrogen are far less thermally stable than clusters with nitrogen.

Chapter 5 is devoted to the interaction between hydrogen isotopes and voids. It is demonstrated that hydrogen desorption techniques combined with the positron annihilation technique can successfully be employed to monitor the exchange of hydrogen with small voids in tungsten and molybdenum. A theoretical model is presented, based on the fact that voids can be saturated with hydrogen. The model enables the study of cavities that are subject to extremely high hydrogen pressures. It is shown how the trends and activation energies found in the experimental work can be reproduced with the model.

Chapter 6 demonstrates the versatility of thermal gas desorption spectrometry by showing its use in three different areas. Firstly, the technique is applied to gain more insight in the growth process of helium precipitates. It is shown that the conversion of helium precipitates from two-dimensional

platelets to three-dimensional bubbles does not significantly influence the accumulation of helium at the precipitates. It is demonstrated how helium precipitates are influenced by self-interstitials, and it also becomes apparent that there is a strong interaction between helium precipitates and substitutional argon atoms.

Secondly, the gas desorption technique has been employed to investigate helium in austenitic stainless steel. Here, a detailed defect assignment is impeded by the vast amounts of structural defects and impurities. It is shown that, in spite of this, gas desorption spectrometry can render useful supplementary information.

Finally, it is demonstrated how gas desorption spectrometry can be utilized to investigate the desorption of volatile species adsorbed at surfaces under the impact of ion irradiation. Preliminary tests on the performance of the novel spectrometer which has especially been developed for this purpose are discussed, and suggestions are given for future developments.

Samenvatting

Dit proefschrift beschrijft een onderzoek naar de interactie tussen gasatomen en puntdefecten in potentiële materialen voor kernfusiereactoren. Het onderzoek is verricht met behulp van thermische-gasdesorptie-spectrometrie en is er op gericht de bruikbaarheid en veelzijdigheid van deze techniek in het onderzoek naar kernfusiematerialen aan te tonen.

In hoofdstuk 1 wordt een korte beschouwing gegeven over kernfusiematerialen, het gedrag van defecten in deze materialen, en de gasdesorptietechniek met behulp waarvan de defecten in het onderhavige onderzoek zijn bestudeerd.

Hoofdstuk 2 beschrijft de apparatuur die gebruikt is voor de gasdesorptieëxperimenten. In dit hoofdstuk wordt beschreven hoe proefmonsters van kernfusiematerialen zijn geprepareerd voor onderzoek, hoe een gewenste defectstructuur is aangebracht in de proefmonsters, op welke manier de desorptie van gassen uit de monsters wordt gemeten, en hoe informatie over defecten kan worden gedistilleerd uit desorptiespectra. Er wordt kort ingegaan op een techniek waarmee aanvullende informatie wordt verkregen: de positron-annihilatietechniek. Tevens worden twee nieuwe desorptiespectrometers gepresenteerd: een spectrometer die is ontwikkeld voor onderzoek naar gasdesorptie geïnduceerd door ionenbestraling, en een spectrometer voor onderzoek naar waterstofisotoop-permeatie door materialen waarin zich puntdefecten bevinden.

In hoofdstuk 3 wordt gedemonstreerd hoe de gasdesorptietechniek is gebruikt om de interactie tussen zelf-interstitiëlen en argon in molybdeen te bestuderen. Allereerst wordt een bestaande methode om zelf-interstitiëlen te creëren zonder interfererende vacatures nader onder de loep genomen. Bevestigd wordt dat laag-energetisch zware-ionen bombardement een zeer geschikte techniek is om stabiele zelf-interstitiëlen te produceren. De rol van atomaire botsingsketens in dit proces wordt toegelicht, en drempelenergieën worden verklaard.

De bovengenoemde produktietechniek voor zelfinterstitiëlen wordt in het resterende gedeelte van hoofdstuk 3 aangewend om de interactie tussen zelf-interstitiëlen en gasatomen in fusiereactormaterialen te onderzoeken. Het blijkt dat in molybdeen dat bestraald wordt met hoge doses laag-energetisch argon het argongedrag niet beschreven kan worden als een superpositie van processen die plaatsvinden by lage doses. Dit is gedeeltelijk te wijten aan het wegsputteren van geaccumuleerd argon tijdens een bestraling, en gedeeltelijk aan de interactie tussen ingeschoten argonatomen en tijdens de bestraling gegenereerde zelf-interstitiëlen. Het blijkt dat de door andere onderzoekers gerapporteerde verzadiging in de hoeveelheid achtergebleven argonatomen na

een bestraling slechts quasi-verzadiging is. Bij hogere dan de tot op heden geëxploreerde doses wordt de hoeveelheid achtergebleven argonatomen voornamelijk bepaald door relatief stabiele defectcomplexen die bestaan uit zelf-interstitiëlen en argonatomen.

In hoofdstuk 4 wordt gedemonstreerd dat thermische-gasdesorptie-spectrometrie een zeer geschikte techniek is voor het meten van lage concentraties vacature-achtige defecten. Geïllustreerd wordt hoe de techniek kan worden gebruikt voor het meten van vacature-herstelcurven en hoe de vacature-migratieënergie hieruit kan worden afgeleid met behulp van een eenvoudig diffusiemodel. De vacature-migratieënergie in molybdeen is op deze manier vastgesteld op $(1{,}23 \pm 0{,}04)$ eV. De aanwezigheid van waterstof in molybdeen bleek geen meetbaar effect te hebben op het herstelgedrag van de vacatures. Voor de dissociatieënergie van waterstof gebonden aan een vacature in molybdeen werd gevonden dat deze minder dan 1,4 eV bedraagt. Een belangrijk deel van hoofdstuk 4 is gewijd aan de interactie tussen stikstof en vacatures in molybdeen. Nieuwe defect-identificatiemethoden en nieuwe theoretische overwegingen worden gepresenteerd en aangewend om onomstotelijk te bewijzen dat de eerder gemeten dissociatieënergie van stikstof gebonden aan een vacature in molybdeen $(2{,}55 \pm 0{,}05)$ eV bedraagt. De belangrijkste invloed van stikstof in molybdeen is dat het de produktie van vacatures tijdens een bestraling significant verhoogt en dat het de thermische stabiliteit van de vacatures sterk bevordert. Dit impliceert dat stikstof, evenals helium, een belangrijke rol speelt in de nucleatie en groei van voids.
De beperkingen van de gasdesorptietechniek komen tot uiting in een onderzoek naar de invloed van stikstof op het herstelgedrag van vacatureagglomeraten. Getoond wordt hoe, ondanks deze beperkingen, grotere samengestelde defecten geïdentificeerd kunnen worden. Dit kan *per exclusionem* door theoretische overwegingen te combineren met beschikbare informatie omtrent kleinere defecten. Aldus zijn stikstof-vacatureagglomeraten waargenomen die stabiel bleken tot een temperatuur van 1100 K. De migratie van zowel vacatures als stikstofatomen werd verhinderd door de onderlinge binding. Voor helium-stikstof-vacature-agglomeraten kon worden afgeleid dat tijdens verhitting de stikstof over het algemeen eerder het defect verlaat dan het helium. De belangrijkste conclusie is dat, evenals bij monovacatures, vacatureagglomeraten zonder stikstof veel minder stabiel zijn dan met stikstof.

In hoofstuk 5 wordt nader ingegaan op de interactie tussen waterstof en voids in wolfraam en molybdeen. Gedemonstreerd wordt hoe de gasdesorptietechniek succesvol kan worden gecombineerd met de positron-annihilatietechniek teneinde deze interactie te bestuderen. Een theoretisch model wordt gepresenteerd dat gebaseerd is op het feit dat voids verzadigd kunnen worden met waterstof. Het model is geschikt voor voids waarin extreem hoge waterstofdrukken heersen. De trends en de activeringsenergieën

die gevonden worden in de experimenten kunnen worden gereproduceerd met het model.

Hoofdstuk 6 illustreert de veelzijdigheid van de gasdesorptietechniek aan de hand van drie verschillende onderwerpen. De techniek wordt eerst toegepast om meer inzicht te verwerven in het groeiproces van heliumprecipitaten in molybdeen. Aangetoond wordt dat de conversie van kleine heliumprecipitaten van twee-dimensionale schijfjes naar drie-dimensionale bellen geen significante invloed heeft op de accumulatie van helium bij de precipitaten. Tevens blijkt dat eenmaal gevormde precipitaten kunnen worden beïnvloed door de aanwezigheid van zelf-interstitiëlen, en dat er een zeer sterke interactie bestaat tussen de precipitaten en vooraf geïntroduceerde substitutionele argonatomen. Vervolgens wordt de techniek gebruikt voor onderzoek aan austenitisch roestvast staal. Een gedetailleerde defectidentificatie is hier onmogelijk vanwege de grote hoeveelheden structurele defecten en verontreinigingen. Desalniettemin wordt getoond dat de gasdesorptietechniek belangrijke aanvullende informatie kan leveren.
Tenslotte wordt gedemonstreerd hoe gasdesorptiespectrometrie kan worden aangewend om de desorptie van aan oppervlakken geadsorbeerde deeltjes onder invloed van ionenbestraling te bestuderen. Een nieuwe spectrometer die voor dit doel is ontwikkeld wordt besproken, en er worden suggesties gegeven voor toekomstige ontwikkelingen.

Acknowledgements

I would like to express my gratitude to all those that have contributed to the work presented in this thesis. In the first place thanks are due to prof. dr. A. van Veen, without whose inspiration, guidance, and ideas this thesis would not have seen the light of day. I am equally obliged to prof. dr. ir. H. van Dam for providing the opportunity to perform the research in his group, and for his accurate and adequate supervision.

Further, I wish to thank Remko Bijkerk and Tim Armstrong for the gas desorption measurements they have carried out. I am greatly indebted to Jouke Heringa and Maurits Ypma for their assistance in computer calculations, and to Bent Nielsen, Henk Schut, and Johan de Vries for showing me the right avenues through the realm of positrons. Dr. J.H. Evans is gratefully acknowledged for TEM measurements and valuable comments.

I continue to be indebted to Jan de Roode, Bob Heyenga, Karl Roos, Dick de Haas, and Ronald Otte for skilful technical assistance. The tutorial suggestions proffered by Kees Westerduin have always been carefully considered and acted on where I felt in agreement with them.

I would like to extend my gratitude to the members of the workshops of the physics department and the IRI. Particular mention should be made of Jan van Oort, who meticulously constructed the components of the miniature ion source.

For their financial support I gratefully acknowledge both the Directorate-General for Science, Research and Development of the Commission of the European Communities (EC stimulation programme CODEST STI-075-J-C (CD) and the European Fusion Technology Programme (Task Mat. 20.2).

Last, but by no means least, I would like to thank all the anonymous contributors and friends that will fall into oblivion.

Hans Filius

Curriculum Vitae

The author of this thesis was born on the 27th of February 1960 in Flushing (Vlissingen) in The Netherlands. In 1978 he obtained his secondary education certificate at the "Christelijk Lyceum" in Apeldoorn. In the same year he started studying Applied Physics at the Delft University of Technology. After obtaining his "Kandidaats" diploma in 1981, he performed his fourth and fifth year research at the Reactor Physics group of the Delft University of Technology. During his studies, the author has worked at the Technical University of Denmark, at the Ben Gurion University in Israel, and at the European Centre for Nuclear Research CERN in Geneva. In May 1985 he finished his studies and received the Master of Science degree ("ingenieur"). After working on a four months contract at the Reactor Physics group of the Interfaculty Reactor Institute of the Delft University of Technology , the author has worked in this group from November 1985 onwards on the research described in this thesis.

De auteur van dit proefschrift werd op 27 februari 1960 geboren te Vlissingen. In 1978 behaalde hij het VWO-diploma aan het Christelijk Lyceum te Apeldoorn. Vervolgens ging hij Technische Natuurkunde studeren aan de Technische Universiteit Delft. Na het kandidaatsexamen in 1981 heeft hij daar zijn vierde- en vijfdejaarswerk verricht in de vakgroep Reactorfysica. Tijdens zijn studie heeft de auteur stages gelopen aan de Technische Universiteit van Denemarken, De Ben Gurion Universiteit in Israel, en bij het CERN te Genève. In mei 1985 studeerde hij af. Na een tijdelijk dienstverband van vier maanden bij de afdeling Reactorfysica van het Interfacultair Reactor Instituut heeft de auteur vanaf november 1985 aldaar gewerkt aan het onderzoek dat is beschreven in dit proefschrift.